Université Catholique de Louvain

Faculté des Sciences
Institut de Recherche en Mathematique et Physique
Center for Cosmology, Particle Physics and Phenomenology

Accurate predictions for Higgs production at the LHC: the VBF channel

Doctoral dissertation presented by

Marco Zaro

in fulfillment of the requirements for the degree of Doctor in Sciences

Jury de thèse:

Prof. Dr. Fabio Maltoni, *Promoteur*	UCL
Prof. Dr. Jean-Marc Gérard	UCL
Prof. Dr. Vincent Lemaitre	UCL
Prof. Dr. Sven-Olaf Moch	DESY/Hamburg
Prof. Dr. Gavin Salam	CERN

July 3rd, 2013

A Elisa,

Grazie!

Poets say science takes away from the beauty of the stars - mere globs of gas atoms. I too can see the stars on a desert night, and feel them. But do I see less or more? The vastness of the heavens stretches my imagination - stuck on this carousel my little eye can catch one - million - year - old light. A vast pattern - of which I am a part... What is the pattern, or the meaning, or the why? It does not do harm to the mystery to know a little about it. For far more marvelous is the truth than any artists of the past imagined it. Why do the poets of the present not speak of it? What men are poets who can speak of Jupiter if he were a man, but if he is an immense spinning sphere of methane and ammonia must be silent?

Thanks!

Penso a tutti gli amici che ho incontrato,
a quelli che non ho saputo amare,
a tutte le canzoni che ho cantato,
e a Te, che non ti stanchi di aspettare.

C. Chieffo

During the writing of this thesis it has become more and more clear to me that nothing could have been done without the help and the support of many precious people. These pages are meant to thank you all. Please forgive me if anybody is forgotten.

First, I would like to thank my advisor, **Prof. Fabio Maltoni**: thanks a lot, Fabio for these four years spent as a Ph.D student of yours! Thanks a for your contagious enthusiasm in studying physics, for the many many hints and ideas you gave me, for all the questions I have asked you (even for the most stupid ones). Thanks also for your friendship to me and Elisa, which has helped us a lot in feeling at home here. And thanks to your wife **Alessia**, and your beautiful daughters **Emma** and **Paola**, even though they laugh at me when I try to speak French.

Then I would like to thanks all the people I have had the pleasure to work with during the Ph.D., for their patience with me, for their help and for all the things I have learnt from them. Thanks to **Prof. Sven Moch** for your kindness with me and for two fruitful years working together and for having taken part to my Ph.D. jury. Thanks also to **Paolo Bolzoni**, that besides being a “collaborator” is also a good friend of mine. Thanks for having not made me feel alone in Zeuthen, for your visits here in Louvain and for your company during the first year of my Ph.D. Thanks to the whole MadGraph/aMC@NLO crew! Thanks to **Olivier** and **Johan** for your introduction to the Python world and for all your precious answer to my questions. Thanks to **Prof. Tim Stelzer** for your enthusiasm and for the friendship born with a bottle of wine in Cargese and grown up with capirinas in Natal. Thanks to **Prof. Stefano Frixione**, **Rikkert** and **Valentin** for all the exciting work done together and for the work still to be done. A special thanks is to **Paolo Torrielli**, for the many many days spent on

Skype trying to understand VBF (otherwise this thesis would have stop after Chapter 4), thanks for your (also psychological) support. Thanks a lot to the VUB group, **Tina**, **Karen** and **Kentarou**. Thanks for your hospitality when I was too lazy to go to Louvain-la-Neuve. Thanks Kentarou for working together.

It is now the turn of the CP3 people. Thanks hanks to **Prof. Jean-Marc Jerard** and **Prof. Vincent Lemaitre** for all the very interesting questions and discussions we have had, and for the useful comments about this thesis. Thanks to my very discreet office mate **Philippe**. Thank you for the fact that, despite the fact that we did not speak too much together, you have always been ready to help me with every problem I have had, from my wisdom teeth to my broken Mac. A special thanks is for our secretary/fiscal expert/personal adviser **Ginette**. Merci pour ton amitié, pour ton aide et pour ta simpathie contageuse. Thanks a lot to **Michael**, you have been one of the first persons I got on with here at CP3. Thanks for your help and for your friendship, as well as for having introduced me to the world of Belgian beers. The "Brasserie Vapeur" will always remain in my heart. I wish you all the best for your life with **Lucie**. Thanks to **Priscila** for your simpathy, and good luck with your kid. Thanks to **Elvira**, **Pierre**, **Antoine**, **Mathieu**, **Ludivine**, **Diogo**, **Gustavo**, the two **Cristophe**'s, **Marcello**, **Lucia**, **Tristan**, **Suzan**, **Cen**, **Roshan**, **Michele** (hoping that you still can eat "pasta e ceci"), **Davide**, **Giacomo**, **Carine**, **Gauthier**, **Claude** and **Arnaud** (good luck for your private defense!) for all the time spent together. Thanks a lot to the IT guys, **Vincent**, **Jerome** and **Pavel**, for all the times I have bothered you with my computer troubles.
A special thanks goes to the "Milano team", and to **Prof. Stefano Forte** for continuously adding new people. Thanks to **Maria** (and also to **Giacomo** and **baby Anna**). Maria, I have to thank you for the year we spent together living in the Belgian countryside. Thanks for having helped me to feel at home when I was just arrived here. Thanks for your freshness, your simplicity and your certitude. Then thanks to **Elisa** for the year and a half you have spent here in CP3. Thanks for your simplicity and your capacity of becoming attached to people. Last (only in order of arrival in Belgium) thanks to **Federico**, for the many questions you have asked me, and good luck for your Ph.D. here.

Turning to the "future", thanks to **Prof. Matteo Cacciari** for having accepted me as a post-doc in Paris and for his many useful comments and suggestions on my works. Thanks to **Prof. Gavin Salam** for having read this thesis, for the many and very stimulating questions and comments. I really hope that this could be the beginning for a future collaboration.

Thanks to all the friends I have met here in Belgium, who have accepted me as I am and are grown with me in these years. A special thanks goes to my flat mates **Luciano**, **Giuseppe**, **Michele** (known as “la bestia”), **Lorenzo**, **Planck**, **Giorgio** and **Didier**. Thanks, specially for the your company and friendship during the one-year-and-a-half spent together. Thanks to **Mauro**, **Stefano**, **Francoise**, **Lucia**, **Rosanna**, **Oxana**, **Angela** and **Marta**. Thanks for what you have been and are for me. Thanks to **Sofia** and **Alba**, the two girls from upstairs. Merci à Christiane, Michel, et Louis pour votre simplicité et pour avoir marché ensemble pendant ces années. Un grand merci à toute la famille **Bleus** pour le chaloreux accueil que ils ont toujours envers nous et pour une très belle amitié. A special thanks is for a very special girl, **Giulia** and her family. Giulia, grazie semplicemente perché ci sei e sei felice. Grazie **Mariangela, Riccardo, Ale e Eli** per avermi praticamente accolto nella vostra famiglia, e per il bene che volete a Elisa.

Thanks to my friends in Italy or around Europe, because despite being apart since four years, our friendship is still there, and all the times we meet it is like if I had never left. This makes me sure that you will also be there when we will move to Paris. Grazie **Due e Luci**, **Manni e Anna**, **Banzo, Giulia e Tommaso**, **Jackie, Maddy, Cate e Stefano**, **Enzo Vale e Albert**, **Coto e Frabbo**, **Marmo, Rita e Ricky**, **Tanzi**, **la Lobe** e **Giò**.

Before turning to the very special person who has accepted to share her life with me, I have to thanks my family. Grazie ai miei genitori **Luisa e Giovanni**, ai miei fratelli **Filippo e Michele**, alle mie nonne **Emma e Anna** e ai miei nonni **Mario e Natale** che mi curano da lassù. Grazie per avermi cresciuto, per avermi trasmesso la passione per quello che faccio e la curiosità per le cose. Grazie sooprattutto perché avete accettato lo strappo di lasciarmi partire, e per il fatto che comunque ci siete sempre nel momento del bisogno.

And last, but first, thanks to my wife **Elisa**. Thanks for how much we have grown up when we still were boyfriend and girlfriend and I was in Belgium and you in Italy. Thanks for having become my spouse, leaving an easy life in Busto Arsizio and starting a risked bet before here in Belgium and then in Paris. Thanks for your certitude that the bet is already won. Thanks for having been my roots during these four years, a root which may not be seen, because it is hidden below, but that makes the tree bloom.

Ci vediamo a Parigi!

Marco

Contents

Appendices

Chapter 1

Introduction

The Standard Model of fundamental introduction is the theory that describes reality at the smallest scales which can be currently probed by experiments. It has been formulated by S. Glashow, A. Salam and S. Weinberg in the 1960's as a gauge theory based on the $SU(2)_L \times U(1)_Y$ groups which unifies electromagnetism and weak interactions [1–3]. The electromagnetic and weak force, before considered as of completely different nature, are now shown to be two sides of the same coin, with weak interactions being "weak" because they are mediated by massive particles, the W and the Z bosons, unlike electromagnetism, which is mediated by the massless photon. Gauge theories, however, forbid their mediators to have a mass, since any mass term in the Lagrangian would explicitly break gauge invariance. The mechanism which allows gauge bosons to acquire a mass was formulated in the same decade by P. W. Higgs, R. Brout, F. Englert, G. Guralnik, C. Hagen and T. Kibble [4–9]. This mechanism consists in adding to the Standard Model Lagrangian a new scalar doublet field, charged under the $SU(2)_L \times U(1)_Y$ group, and interacting with the gauge bosons in a gauge invariant manner. This new field has the remarkable property of having a non-vanishing vacuum expectation value, which is not $SU(2)_L \times U(1)_Y$-symmetric. Once the theory is expanded around this vacuum expectation value, mass-terms for the weak gauge boson appears. This mechanism does not explicitly break gauge invariance, since the interactions of the scalar doublet with the gauge fields do not violate it, and is known as the spontaneous symmetry breaking mechanism. Besides giving mass to Standard Model particles, this mechanism predicts the existence of an new scalar state, called the Higgs boson.

In the same period, the last ingredient was added to the Standard Model, which consisted in formulating also the strong interactions, those relevant for binding the nucleons (protons and neutrons), as a gauge theory, Quantum Chromo-Dynamics

(QCD), based on the $SU(3)$ group. This formulation, which was driven by some astonishing results in experiments which were probing nucleons with highly-energetic electrons, was proposed by M. Gell-Mann, H. Fritzsch, D. Gross, F. Wilczek and H. D. Politzer [10–13], and considers hadrons as bunches of partons, quarks and gluons.

After the inclusion of strong interactions, the Standard Model has remained the same for almost forty years, obtaining more and more confirmations of its validity by various experiment, where the parameters of the theory have been measured with astonishing precision. However, people had to wait until 2012 when the last missing confirmation of the validity of the Standard Model was found. Until then, no evidence of the existence of the Higgs boson was found: on July 4th 2012 the two experiments at the Large Hadron Collider at the CERN (Geneva), ATLAS and CMS, claimed the observation of a new particle, with mass of about 125 GeV and with properties compatible with these predicted for the Higgs boson [14,15]. This claim was based on data acquired on both the 7 TeV and 8 TeV runs, with about 5fb^{-1} of integrated luminosity per run per experiment. At present, one year later, after the end of the 8 TeV run with the integrated luminosity exceeding 20fb^{-1}, data seems to point towards the fact that these new particle has indeed the right characteristics to be considered as *the* Higgs boson [16–18].

These great achievements would not have been possible without the enthusiastic work of thousands of people, either involved in building and running the accelerator and the experiments, or in providing the best possible theoretical predictions for the various production channels of the Higgs boson, and for the corresponding backgrounds.

As the LHC is a hadron collider, strong interactions dominate the scene. First of all, processes mediated by strong interactions represent an overwhelming background for all kind of searches, their typical rates being orders of magnitude larger than those of any electro-weak process (see also Fig. 1.1). Second, even for processes driven by electro-weak reactions, thousands of hadrons originating from the remnants of the colliding protons typically accompany the event. And finally, as observables can only be computed in perturbation theory, typically identifying the expansion parameter with the strong coupling $\alpha_s \simeq 0.1$, QCD can induce sizable corrections to observables. While this last point has not been an issue for the discovery of the Higgs boson, as it happened exploiting channels with a clear mass-peak signature, it does affect the determination of the properties of the new particle.

In the last years lots of efforts have been spent in order to have computations that include QCD corrections, at least at the first non-trivial order (called next to leading

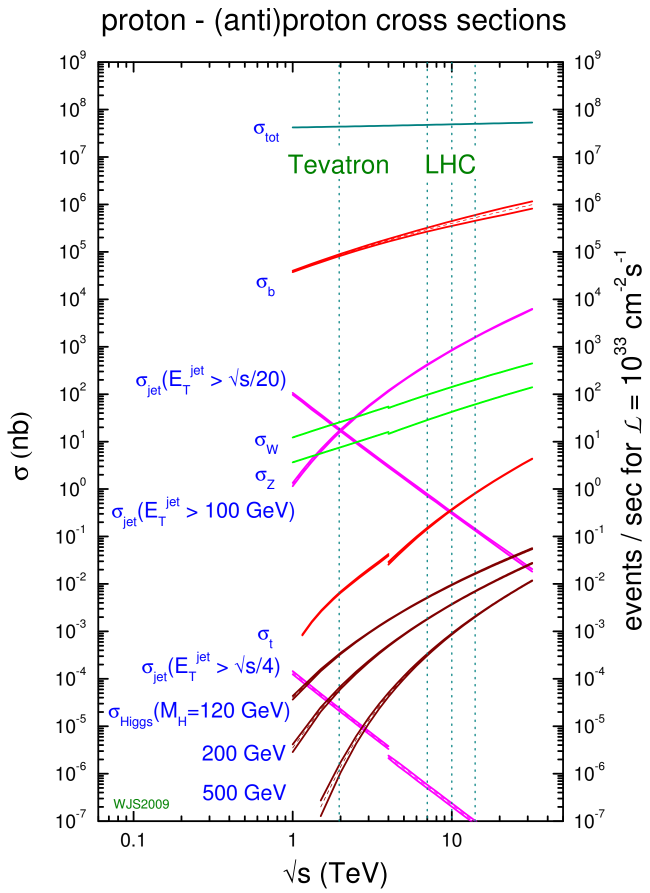

Figure 1.1: Cross-sections for the most important processes at hadron colliders. Image from [19]

order, NLO). One result of these efforts is the amazing precision to which the cross-section of all Higgs production processes can be computed, see Fig. 2.3 in the text. In parallel to these efforts, lot of work have also been done towards providing event simulations which are as much realistic as possible, giving a picture of the final state in terms of hadrons, rather than in terms of partons as typical for perturbative computations.
These efforts have lead to the possibility of computing NLO observables for virtually any process, in an automatic way, with a realistic simulation of the final state, the only limitation being the computing time.

In this thesis I will present the state-of-the-art predictions for the second most important Higgs boson production channel, called vector-boson fusion (VBF). The total cross-section of this process is now known including NNLO QCD corrections (*i.e.*corrections up to the second non-trivial order in α_s) as well as electroweak NLO corrections. For more differential observables, I will present the computation of NLO corrections with a fully hadronic simulation of the final state.

In Chapter 2 I will introduce the Standard Model of fundamental interactions, with particular focus on the role of the Higgs boson in originating particle masses. Chapter 3 will be devoted to the presentation of VBF, the topic of this thesis. In Chapter 4 I will detail the computation of NNLO QCD corrections to the total cross-section of VBF, with the main result of reducing the residual theoretical uncertainties down to few percents in the whole scanned mass range. Once these corrections are combined with NLO electroweak corrections, VBF can be considered to be the best known total cross-section at the LHC. After the computation of the total cross-section, I will turn to the computation of more exclusive observables: in Chapter 5 I will present the computation of NLO corrections to many different observables, with a fully differential hadronic description of the final state.

This thesis is based on the following publications

- [20] P. Bolzoni, F. Maltoni, S. Moch, and M. Zaro, Higgs production via vector-boson fusion at NNLO in QCD, Phys.Rev.Lett. **105**, 011801 (2010), arXiv:1003.4451,
- [21] P. Bolzoni, F. Maltoni, S.-O. Moch, and M. Zaro, Vector boson fusion at NNLO in QCD: SM Higgs and beyond, Phys.Rev. **D85**, 035002 (2012), arXiv:1109.3717,
- [22] S. Frixione, P. Torrielli, and M. Zaro, Higgs production through vector-boson fusion at the NLO matched with parton showers, Submitted to Phys. Lett. **B** (2013), arXiv:1304.7927,

on the results in the VBF sections of the CERN Yellow Reports

- [23] LHC Higgs Cross Section Working Group, S. Dittmaier *et al.*, Handbook of LHC Higgs Cross Sections: 1. Inclusive Observables, (2011), arXiv:1101.0593,
- [24] LHC Higgs Cross Section Working Group, S. Dittmaier *et al.*, Handbook of LHC Higgs Cross Sections: 3. Higgs Properties, (in preparation) (2013),

and on the conference proceedings [25–27].

Chapter 2

The Higgs boson in the Standard Model

In this first chapter I will present a brief introduction to she Standard Model (SM) of strong and electroweak interactions. I will first introduce in Sec. 2.1 the gauge structure of the interactions, and the particle content of the SM, building, in Sec. 2.2, the SM Lagrangian. As I will show, gauge symmetries require all particles to be massless, and this is in neat contrast with the experimental observation of massive fermions (e.g. the top quark) and massive gauge bosons. This is the so-called "problem of masses". In order to solve the problem of masses, *i.e.*to allow mass terms in the Lagrangian without breaking gauge invariance, in the 1960's, P. W. Higgs, R. Brout, F. Englert, G. Guralnik, C. Hagen and T. Kibble have proposed a mechanism [4–9] in which gauge symmetries are spontaneously broken by the introduction of an extra field. This field, called the Higgs field, has a vacuum-expectation-value which breaks gauge symmetries, therefore allowing gauge bosons to acquire a mass. I will explain this mechanism in Sec. 2.3. After giving mass to gauge bosons, the remnant of the Higgs field is a scalar particle, the Higgs boson.
Almost fifty years after the hypothesis of its existence, and several particle-physics experiments looking for it, the Higgs boson has finally been discovered [14, 15] by both the ATLAS and CMS experiments at the Large Hadron Collider (LHC) at the CERN. I will terminate this chapter by presenting in Sec. 2.4 the main production mechanisms at the LHC.

2.1 The SM before electroweak symmetry breaking

The Glashow-Weinberg-Salam electroweak theory [1–3] which describes the electromagnetic and weak interactions between quarks and leptons, is a gauge theory based on the symmetry group $SU(2)_L \times U(1)_Y$. Combined with Quantum Chromo-Dynamics (QCD) the theory of strong interactions based on the $SU(3)_C$ group [10–13], it provides a unified framework to describe these three forces of nature. This framework is the Standard Model. The model, before introducing the electroweak symmetry breaking mechanism discussed in Sec. 2.3, has two kind of fields: matter and gauge fields.

2.1.1 The matter content of the SM

The SM matter fields consist in three generations of left-handed and right-handed chiral Dirac fermions, classified into the two families of quarks and leptons. Left handed fields are in doublets with respect to the weak isospin group $SU(2)_L$, while right-handed are singlets.
Leptons of the first, second and third family are respectively called of “electronic”, “muonic” and “tauonic” flavor. Each leptonic family consist in one electrically charged lepton, with relative charge $Q_l = -1$, (called electron, muon and tau), and one neutral, massless particle: the neutrino. Right handed neutrinos completely decouple in the SM, and therefore will not be considered in what follows.
Each of the three families of quarks consist in an up- and down-type quark. Up and down quarks have relative electric charge respectively $Q_{up} = 2/3$, $Q_{down} = -1/3$. Unlike leptons, quarks are charged under the strong interactions, and they are triplets in the $SU(3)$ gauge group. The three up type quarks are called up (u), charm (c) and top (t), and the three down type down (d), strange (s) and bottom (b).
I will dub L^i and Q^i the left-handed lepton and quark isospin doublets of the i-th family,

$$\begin{aligned}
L_1 &= \begin{pmatrix} \nu_e \\ e^- \end{pmatrix}_L, & Q_1 &= \begin{pmatrix} u \\ d \end{pmatrix}_L, \\
L_2 &= \begin{pmatrix} \nu_\mu \\ \mu^- \end{pmatrix}_L, & Q_2 &= \begin{pmatrix} c \\ s \end{pmatrix}_L, \\
L_3 &= \begin{pmatrix} \nu_\tau \\ \tau^- \end{pmatrix}_L, & Q_3 &= \begin{pmatrix} t \\ b \end{pmatrix}_L,
\end{aligned} \tag{2.1}$$

and u_R^i, d_R^i, e_R^i, ν_R^i the right-handed up-type quark, down-type quark, charged leptons and neutrinos

$$\begin{aligned} u_R^1 &= u^R\,, & d_R^1 &= d_R\,, & e_R^1 &= e_R^-\,, & \nu_R^1 &= \nu_{eR}\,, \\ u_R^2 &= c^R\,, & d_R^2 &= s_R\,, & e_R^2 &= \mu_R^-\,, & \nu_R^2 &= \nu_{\mu R}\,, \\ u_R^3 &= t^R\,, & d_R^3 &= b_R\,, & e_R^3 &= \tau_R^-\,, & \nu_R^3 &= \nu_{\tau R}\,. \end{aligned} \tag{2.2}$$

The upper and lower component of each doublet have respectively isospin $I_{f_L} = \pm 1/2$, while right-handed singlets have $I_{f_R} = 0$. The hypercharge (*i.e.*the charge with respect to the $U(1)_Y$ group) depends on the electric and isospin charge as

$$Y_f = 2Q_f - 2I_f\,. \tag{2.3}$$

Right handed neutrinos, which have zero isospin, electric charge and hypercharge, are completely decoupled in the SM, and will not enter in what follows.

2.1.2 The gauge content of the SM

The SM gauge fields are spin-one bosons that mediate the gauge interactions. In the electroweak sector, there is the field B_μ corresponding to the generator Y of $U(1)_Y$ and the three fields W_μ^a corresponding to the generators I^a of $SU(2)_L$. These generators can be written in terms of the Pauli matrices as

$$I^a = \frac{1}{2}\tau^a\,. \tag{2.4}$$

These generator obey the commutation relations

$$\left[T^a, T^b\right] = \mathrm{i}\epsilon^{abc}T_c\,, \quad [T^a, Y] = [Y, Y] = 0\,. \tag{2.5}$$

For what concerns strong interactions, gauge fields are an octet of gluon fields G_μ^a corresponding to the eight generators of the $SU(3)_C$ group (the Gell-Mann matrices t^a) which obey the relations

$$\left[t^a, t^b\right] = \mathrm{i}f^{abc}t_c\,, \tag{2.6}$$

in terms of the $SU(3)_C$ structure constants f^{abc}, and which are normalized such that

$$\mathrm{Tr}(t^a) = 0\,, \qquad \mathrm{Tr}\left(t^a t^b\right) = \frac{1}{2}\delta_{ab}\,. \tag{2.7}$$

The field strengths are

$$\begin{aligned} G^a_{\mu\nu} &= \partial_\mu G^a_\nu - \partial_\nu G^a_\mu + g_s f^{abc} G^b_\mu G^c_\nu , && (2.8) \\ W^a_{\mu\nu} &= \partial_\mu W^a_\nu - \partial_\nu W^a_\mu + g_2 \epsilon^{abc} W^b_\mu W^c_\nu , && (2.9) \\ B^a_{\mu\nu} &= \partial_\mu B^a_\nu - \partial_\nu B^a_\mu , && (2.10) \end{aligned}$$

with g_s, g_2 and g_1 the coupling constants respectively of $SU(3)_C$, $SU(2)_L$, $U(1)_Y$.

2.2 The SM Lagrangian and the problem of masses

After having presented the SM fields, I now turn to discuss their interactions. The matter fields ψ are minimally coupled to gauge fields by means of the covariant derivative D_μ which is defined as

$$D_\mu \psi = \left(\partial_\mu - \mathrm{i} g_2 T_a W^a_\mu - \mathrm{i} g_1 \frac{Y_f}{2} B_\mu \right) \psi . \tag{2.11}$$

In the case of quarks, the extra term $-ig_s t_a G^a_\mu$ corresponding to the strong interactions has to be added, while for right-handed fermions the isospin term has to be dropped.

The SM Lagrangian, without mass terms for fermions and gauge bosons is then given by

$$\begin{aligned} \mathcal{L}_{SM} &= -\frac{1}{4} G^a_{\mu\nu} G^{\mu\nu}_a - \frac{1}{4} W^a_{\mu\nu} W^{\mu\nu}_a - \frac{1}{4} B_{\mu\nu} B^{\mu\nu} + && (2.12) \\ &\quad + \bar{L}_i \mathrm{i} D_\mu \gamma^\mu L_i + \bar{e}^R_i \mathrm{i} D_\mu \gamma^\mu e^R_i + \bar{Q}_i \mathrm{i} D_\mu \gamma^\mu Q_i + \bar{u}^R_i \mathrm{i} D_\mu \gamma^\mu u^R_i + \bar{d}^R_i \mathrm{i} D_\mu \gamma^\mu d^R_i , \end{aligned}$$

and is invariant under local $SU(3)_C \times SU(2)_L \times U(1)_Y$ gauge transformations for fermions and gauge fields. In the case of the electroweak sector, for instance, one has

$$\begin{aligned} L(x) &\rightarrow L'(x) = \exp(\mathrm{i}\alpha_a(x) T^a + \mathrm{i}\beta(x) Y) L(x) , \\ R(x) &\rightarrow R'(x) = \exp(\mathrm{i}\beta(x) Y) R(x) , \\ W^a_\mu(x) &\rightarrow W'^a_\mu(x) - \frac{1}{g_2} \partial_\mu \alpha^a(x) - \epsilon^{abc} \alpha^b(x) W^c_\mu(x) , \\ B_\mu(x) &\rightarrow B'_\mu(x) - \frac{1}{g_1} \partial_\mu \beta(x) . && (2.13) \end{aligned}$$

Up to now, gauge fields and fermions have been kept massless. Since experimentally weak gauge bosons have been proved to be massive, a mass term of the form $\frac{1}{2}M_V^2 W_\mu W^\mu$ should appear in the Lagrangian. However such a term will violate the $\times SU(2)_L \times U(1)_Y$ gauge invariance. In the simpler case of quantum electro-dynamics (QED), the $U(1)_{EM}$ gauge invariance indeed forces the photon to be massless. The presence of masses is troublesome also in the fermionic sector, since a mass term of the form $-m\bar{\psi}_R\psi_L$ couples the right and left handed fermions, which carry different $U(1)_Y$ and $SU(2)_L$ charges.

As said, experimental evidences show that weak bosons and fermions do have a mass, and this has forced people in the scientific community to look for a mechanism to generate mass terms without breaking gauge invariance. Such a mechanism has been found more than forty years ago, and is known as the Higgs-Brout-Englert-Guralnik-Hagen-Kibble mechanism of spontaneous symmetry breaking [4–9], or simply as the Brout-Englert-Higgs (BEH) mechanism. I will explain the BEH mechanism in the following section, applying it explicitly to the case of the SM.

2.3 The BEH mechanism

2.3.1 The Goldstone theorem

The starting ingredient for understanding the BEH mechanism is the Goldstone theorem [28–32].

Consider the Lagrangian for a simple real scalar field ψ,

$$\mathcal{L} = \frac{1}{2}\partial_\mu\phi\partial^\mu\phi - V(\phi), \quad \text{with} \quad V(\phi) = \frac{1}{2}\mu^2\phi^2 + \frac{1}{4}\lambda\phi^4 \,. \tag{2.14}$$

Such a Lagrangian is invariant under the reflexion symmetry $\phi \rightarrow -\phi$ since no cubic terms are present. If the mass terms μ^2 is positive, the potential $V(\phi)$ is also positive (if also $\lambda > 0$), and the minimum of the potential is obtained for

$$\langle 0|\phi|0\rangle = \phi_0 = 0 \,. \tag{2.15}$$

In this case, $\mathcal{L}$ is simply the Lagrangian for a scalar field of mass μ.

In the opposite case, if $\mu^2 < 0$, the potential $V(\phi)$ has no more a minimum at $\phi = 0$. Asking its derivative to be zero one has

$$\frac{\partial V}{\partial \phi} = \mu^2 \phi + \lambda \phi^2 = 0\,, \tag{2.16}$$

Which is solved for

$$\langle 0|\phi|0\rangle = \phi_0 = \pm\sqrt{-\frac{\mu^2}{\lambda}} \equiv v\,. \tag{2.17}$$

v is called the vacuum expectation value (vev) of the scalar field ϕ. In this case, to obtain the correct interpretation of $\mathcal{L}$ one has to expand around one of the mimima v by defining a rescaled field $\sigma = \phi - v$. In terms of σ the new Lagrangian (up to constants) is

$$\mathcal{L} = \frac{1}{2}\partial_\mu \sigma \partial^\mu \sigma - (-\mu^2)\sigma^2 - \sqrt{-\mu^2 \lambda}\sigma^3 - \frac{\lambda}{4}\sigma^4\,, \tag{2.18}$$

corresponding to a scalar field of mass $m^2 = -2\mu^2$ with cubic and quartic self-interactions. The presence of a cubic interaction breaks the reflexion symmetry present in the original Lagrangian. However, the second Lagrangian has been obtained by simply rescaling, the ϕ field appearing in the first, so the correct formulation of the above sentence is that the original reflection symmetry is no more manifest in the new Lagrangian, because the choice of vacuum state broke it. This is the simplest example of a spontaneously broken symmetry.

In the previous example, the original symmetry of the Lagrangian was a discrete symmetry. A slightly more complicated case is the that of a continuous symmetry. Consider the Lagrangian for four real scalar fields ϕ_i, $i = 0, 1, 2, 3$

$$\mathcal{L} = \frac{1}{2}\partial_\mu \phi_i \partial^\mu \phi_i - \frac{1}{2}\mu^2 (\phi_i \phi_i) - \frac{1}{4}\lambda (\phi_i \phi_i)^2\,. \tag{2.19}$$

This Lagrangian is invariant under the (continuous) transformations

$$\phi_i(x) \to R_{ij}\phi_j(x)\,, \tag{2.20}$$

for any (orthogonal) matrix R belonging to $O(4)$, the rotation group in four dimensions. As for the single scalar field, in the case $\mu^2 < 0$, the minimum of the potential occurs for

$$\phi_i \phi_i = -\frac{\mu^2}{\lambda} \equiv v^2\,. \tag{2.21}$$

Unlike the single scalar field case, where the minima were a discrete set, now they are a four-dimensional sphere.
I rewrite now the Lagrangian expanding the fields around the minimum

$$\phi_{min} = (v,0,0,0)\,, \tag{2.22}$$

and defining $\sigma = \phi_0 - v$ and $\phi_i = \pi_i$, for $i = 1,2,3$. In terms of σ and of the three π_i the Lagrangian becomes

$$\begin{aligned}\mathcal{L} \;=\; & \frac{1}{2}\partial_\mu\sigma\partial^\mu\sigma - \frac{1}{2}\left(-2\mu^2\right)\sigma^2 - \lambda v\sigma^3 - \frac{\lambda}{4}\sigma^4 + \\ & + \frac{1}{2}\partial_\mu\pi_i\partial^\mu\pi_i - \frac{\lambda}{4}\left(\pi_i\pi_i\right)^2 - \lambda v\pi_i\pi_i\sigma - \frac{\lambda}{2}\pi_i\pi_i\sigma^2\,. \end{aligned} \tag{2.23}$$

This Lagrangian corresponds to a massive field σ, as for the previous case, but with in addition three massless scalar fields π_i. These π_i fields enjoy an $O(3)$ symmetry, which is the leftover of the original $O(4)$.
Since the number of generators of $O(N)$ is $N(N-1)/2$, three out of the six generators of the original $O(4)$ correspond to broken symmetries. Indeed the choice of the minimum in Eq. (2.22) breaks the three generators corresponding to rotations that mix the first component with the others, but not those that act only on the last three components. For each broken generator the corresponding massless π_i field has appeared. The Goldstone theorem [28–32], states exactly what has been proved: for any spontaneously broken continuous symmetry, the theory must contain a massless particle, called the Goldstone boson.

2.3.2 The BEH mechanism in an abelian theory

The Goldstone theorem is valid for global symmetries. I will now consider what happens in the case of a local U(1) symmetry. Consider the Lagrangian for a complex scalar field coupled to an electromagnetic field A^μ:

$$\mathcal{L} = -\frac{1}{4}F_{\mu\nu}F^{\mu\nu} + D_\mu\phi D^\mu\phi^* - V(\phi)\,, \tag{2.24}$$

where the electromagnetic covariant derivative is defined as

$$D_\mu = \partial_\mu - \mathrm{i}eA_\mu \tag{2.25}$$

and the scalar potential is

$$V(\phi) = \mu^2\phi^*\phi + \lambda\left(\phi\phi^*\right)^2\,. \tag{2.26}$$

This Lagrangian is invariant under the local $U(1)$ transformation

$$\begin{aligned} \phi(x) &\rightarrow \exp(\mathrm{i}\alpha(x))\,\phi(x)\,, && (2.27)\\ A_\mu &\rightarrow A_\mu - \frac{1}{e}\partial_\mu \alpha(x)\,. && (2.28) \end{aligned}$$

The case $\mu^2 > 0$ corresponds to the QED Lagrangian for a charged scalar particle with mass μ and quartic self-interaction. The opposite case, $\mu^2 < 0$ the field ϕ acquires a vev, with the potential minimum at

$$\langle \phi \rangle = \sqrt{-\frac{\mu^2}{2\lambda}} \equiv \frac{v}{\sqrt{2}}\,. \tag{2.29}$$

As before the physical Lagrangian is obtained by rescaling the field ϕ. In this case it is more convenient to introduce two real fields ϕ_1, ϕ_2 defined as

$$\phi = \frac{1}{\sqrt{2}}\left(v + \phi_1(x) + \mathrm{i}\phi_2(x)\right)\,, \tag{2.30}$$

in terms of which the new (rescaled) Lagrangian is

$$\mathcal{L} = -\frac{1}{4}F_{\mu\nu}F^{\mu\nu} + \frac{1}{2}\left(\partial_\mu\phi_1\right)^2 + \frac{1}{2}\left(\partial_\mu\phi_2\right)^2 - v^2\lambda\phi_1^2 + \frac{1}{2}e^2v^2A_\mu A^\mu - evA_\mu\partial^\mu\phi_2\,. \tag{2.31}$$

Some interaction terms, which are not relevant for the discussion, have been omitted. In the new Lagrangian a photon mass term has appeared, corresponding to a photon mass $M_A = ev = -e\mu/\lambda$, as well as a mass term for ϕ_1 ($M_{\phi_1} = -\sqrt{2}\mu$), while no mass term appears for ϕ_2.

However, in this form, the Lagrangian in Eq. (2.31) has one extra degree of freedom with respect to the original one in Eq. (2.24), because the photon is now massive, thus with three possible polarization states instead of two. Therefore, one degree of freedom in Eq. (2.31) has not to be physical. The same conclusion can be drawn by noticing the presence of the bilinear term $evA^\mu\partial_\mu\phi_2$ which has to be eliminated. $U(1)$ gauge symmetry comes to help: in Eq. (2.30), the field ϕ_2 appears as imaginary part of ϕ. It can be eliminated by a $U(1)$ gauge transformation with parameter $\alpha = \arg(\phi)$. This choice of gauge makes ϕ_2 disappear from the Lagrangian Eq. (2.31), only leaving the physical degrees of freedom. It is called unitary gauge, and can be interpreted as the photon absorbing the Goldstone boson as its longitudinal polarization state, thus becoming massive. The original $U(1)$ symmetry is not apparent any longer, and it is said to be spontaneously broken. This is the BEH mechanism [4–9], through which gauge bosons masses are generated.

2.3.3 The BEH mechanism in the SM

After having discussed the case for an abelian theory, I extend the discussion to the case of the SM Lagrangian Eq. (2.13). After spontaneous symmetry breaking, one should obtain the correct mass pattern in the electroweak sector, *i.e.*massive $W^\pm$ and Z bosons and a massless photon. Since the three massive bosons would incorporate at least three degrees of freedom in their longitudinal polarization state, the simplest choice for the scalar field is to have a complex $SU(2)_L$ doublet

$$\Phi = \begin{pmatrix} \phi^+ \\ \phi^0 \end{pmatrix}, \tag{2.32}$$

with hypercharge $Y_\Phi = 1$. The Lagrangian for the dynamic of the scalar doublet is

$$\mathcal{L}_S = (D_\mu \Phi)^\dagger D^\mu \Phi - \mu^2 \Phi^\dagger \Phi - \lambda(\Phi^\dagger \Phi). \tag{2.33}$$

As in the previous sections, the $\mu^2 < 0$ case has to be considered. Since electromagnetism must not be broken, the vev acquired by Φ should correspond to the neutral component:

$$\langle 0|\Phi|0\rangle = \begin{pmatrix} 0 \\ \frac{v}{\sqrt{2}} \end{pmatrix}, \tag{2.34}$$

with, as usual

$$v = \sqrt{-\frac{\mu^2}{\lambda}}. \tag{2.35}$$

Introducing the rescaled fields θ_i, $i = 1,2,3$ and H, the Φ doublet can be written as (the dependence on x of all fields is understood)

$$\Phi = \begin{pmatrix} \theta_2 + \mathrm{i}\theta_1 \\ \frac{1}{\sqrt{2}}(v+H) - \mathrm{i}\theta_3 \end{pmatrix}. \tag{2.36}$$

As learned from the abelian case discussed in Sec. 2.3.2, not all the fields in Eq. (2.36) are physical. Indeed, since three degrees of freedom will be acquired by the massive weak bosons, the three θ_i fields can be eliminated by a suitable gauge transformation, so that, in the unitary gauge, one has

$$\Phi = \frac{1}{\sqrt{2}} \begin{pmatrix} 0 \\ v+H \end{pmatrix}. \tag{2.37}$$

The masses for the weak bosons are generated by the kinetic term in Eq. (2.33):

$$\begin{aligned} \left|D^\mu\Phi\right|^2 &= \left|\left(\partial_\mu - \mathrm{i}g_2\frac{\tau_a}{2}W^a_\mu - \mathrm{i}g_1\frac{1}{2}B_\mu\right)\Phi\right|^2 = \\ &= \frac{1}{2}\left|\begin{pmatrix} \partial_\mu - \frac{\mathrm{i}}{2}\left(g_2W^3_\mu + g_1B_\mu\right) & -\mathrm{i}\frac{g_2}{2}\left(W^1_\mu - \mathrm{i}W^2_\mu\right) \\ -\mathrm{i}\frac{g_2}{2}\left(W^1_\mu + \mathrm{i}W^2_\mu\right) & \partial_\mu + \frac{\mathrm{i}}{2}\left(g_2W^3_\mu - g_1B_\mu\right) \end{pmatrix}\begin{pmatrix} 0 \\ v+H \end{pmatrix}\right|^2 = \\ &= \frac{1}{2}(\partial_\mu H)^2 + \frac{1}{8}g_2^2(v+H)^2\left|W^1_\mu + \mathrm{i}W^2_\mu\right|^2 + \frac{1}{8}(v+H)^2\left|g_2W^3_\mu - g_1B_\mu\right|^2 . \end{aligned} \tag{2.38}$$

In particular, from Eq. (2.38) two mass terms arise: one, which corresponds to the first two components of the W_μ field, and the second which corresponds to a linear combination of W^3_μ and B_μ.
The first two components of the W_μ field, can be combined to obtain the charged $W^\pm_\mu$ fields as

$$W^\pm_\mu = \frac{1}{\sqrt{2}}\left(W^1_\mu \mp \mathrm{i}W^2_\mu\right), \tag{2.39}$$

which therefore acquire a mass

$$M_W = \frac{1}{2}vg_2 . \tag{2.40}$$

For what concerns the Z boson, it appears as the linear combination

$$Z_\mu = \frac{g_2W^3_\mu - g_1B_\mu}{\sqrt{g_2^2 + g_1^2}}, \tag{2.41}$$

with a corresponding mass

$$M_Z = \frac{1}{2}v\sqrt{g_1^2 + g_2^2}. \tag{2.42}$$

Starting from the four fields B_μ, W^i_μ I have obtained three massive vector bosons. One more field remains, which do not receive any mass term from the Higgs. It is the photon, A_μ, which can be obtained as the combination of W^3_μ and B_μ orthogonal to the Z boson. Introducing the weak mixing angle θ_w, defined from

$$\cos\theta_w = \frac{g_2}{\sqrt{g_1^2 + g_2^2}}, \tag{2.43}$$

both the Z and the photon can be obtained from the rotation

$$\begin{pmatrix} Z_\mu \\ A_\mu \end{pmatrix} = \begin{pmatrix} \cos\theta_w & -\sin\theta_w \\ \sin\theta_w & \cos\theta_w \end{pmatrix} \begin{pmatrix} W^3_\mu \\ B_\mu \end{pmatrix} . \tag{2.44}$$

In terms of θ_w The W and Z boson mass are linked by the relation

$$\frac{M_W}{M_Z} = \cos\theta_w . \tag{2.45}$$

2.3.3.1 Generation of fermion masses

I will now discuss the mechanism, originally introduced by Weinberg [2], through which fermion masses can be generated in the SM without violating gauge invariance. This can be achieved with the same scalar doublet Φ which generates the gauge boson masses, together with its "conjugate" isodoublet $\widetilde{\Phi} = i\tau_2\Phi^*$. The hypercharge of $\widetilde{\Phi}$ is opposite to that of Φ.

For any fermionic generation, it is possible to build an $SU(2)_L \times U(1)_Y$ invariant Lagrangian, corresponding to a Yukawa interaction between Φ and the fermions

$$\mathcal{L}_F = -\lambda_e \bar{L}\Phi e_R - \lambda_d \bar{Q}\Phi d_R - \lambda_u \bar{Q}\widetilde{\Phi} u_R + h.c.. \tag{2.46}$$

Replacing Φ with the rescaled expression in the unitary gauge given in Eq. (2.37) one obtains (taking the electron case as representative)

$$\mathcal{L}_F = -\frac{1}{\sqrt{2}}\lambda_e (\bar{\nu}_e, \bar{e}_L) \begin{pmatrix} 0 \\ v+H \end{pmatrix} e_R + \ldots = -\frac{1}{\sqrt{2}}\lambda_e (v+H)\bar{e}_L e_R + \ldots , \tag{2.47}$$

where the constant in front of $\bar{e}_L e_R$ can be identified with the fermion mass

$$m_f = \frac{\lambda_f v}{\sqrt{2}} . \tag{2.48}$$

2.3.4 The Higgs particle in the SM

After having explained the BEH mechanism for the generation of masses, I now introduce the Higgs particle, corresponding to the field H in the Φ isodoublet.

The Higgs boson Lagrangian can be obtained from that relevant for the Φ doublet Eq. (2.33):

$$\mathcal{L}_H = \frac{1}{2}\partial_\mu H \partial^\mu H - V(H) , \tag{2.49}$$

where the potential in terms of the H field is (recalling the relation $v = -\mu^2/\lambda$

$$V(H) = -\frac{1}{2}\lambda v^2 (v+H)^2 + \frac{1}{4}\lambda(v+H)^4 = +\lambda v^2 H^2 + \lambda v H^3 + \frac{\lambda}{4} H^4 \,. \tag{2.50}$$

In the potential Eq. (2.50) a mass term for H appears, corresponding to a Higgs mass

$$M_H^2 = 2\lambda v^2 = -2\mu^2 \,, \tag{2.51}$$

as well as tri- and quadri-linear Higgs self interactions.

The terms which are responsible for the interactions of the Higgs particle with the other SM particles can be immediately derived by Eq. (2.38) and Eq. (2.47), respectively for interactions with weak bosons and fermions.
The interactions between the Higgs and weak bosons are governed by the terms

$$\mathcal{L}_{HV} = 2\frac{M_V^2}{v} V^\mu V_\mu^\dagger H + \frac{M_V^2}{v^2} V^\mu V_\mu^\dagger H^2 \,, \tag{2.52}$$

where $V = W^+, Z$ ($V^\dagger = W^-, Z$).
For what concerns Higgs and fermions, the relevant terms are

$$\mathcal{L}_{HF} = -\frac{m_f}{v} H \bar{f}_L f_R + h.c. \,. \tag{2.53}$$

In general one can notice that the couplings between the Higgs boson and another particle is proportional to the particle mass. Therefore the Higgs boson will interact most with the heaviest particles in the SM (the top quark and the weak bosons).
The Feynman rules for Higgs self-coupling and interactions with bosons and fermions are shown in Fig. 2.1.

To conclude this paragraph I want to highlight that the SM Higgs boson is the “minimal solution” to the problem of fermion and boson masses, as all masses are generated by means of a single Higgs field, and all are proportional to the Higgs field vev. Other solutions exist, where more Higgs field come in extra doublets or in higher $SU(2)_I$ representations, but will not be discussed in this thesis.

Before the Higgs discovery on July 4th 2012 [14, 15], the only free parameter of the SM was the Higgs mass, related to the Higgs self-coupling constant λ by Eq. (2.51). For what concerns the vev, it is related to the W boson mass, which is also related to

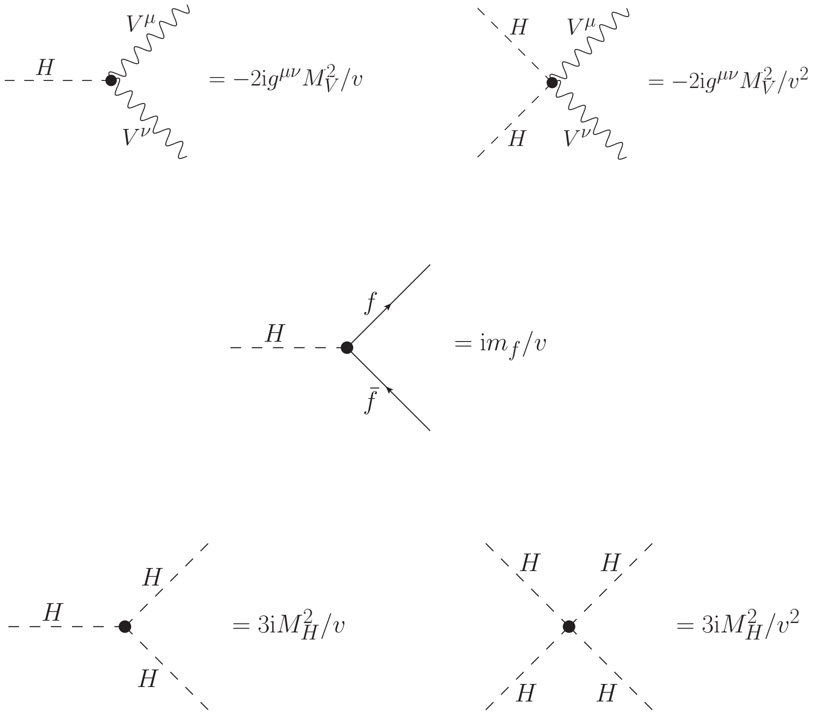

Figure 2.1: Feynman rules for the Higgs boson in the Standard Model.

the Fermi coupling constant G_F measured from the muon decay ($G_F = 1.1663787(6) \times 10^{-5}\,\mathrm{GeV}^{-2}$ [33]). The relation

$$M_W = \frac{1}{2} g_2 v = \left(\frac{\sqrt{2} g_2^2}{8 G_F} \right)^{1/2} , \tag{2.54}$$

leads to $v = 246\,\mathrm{GeV}$. After the measurements of the weak boson masses, also the constants g_1, g_2 can be determined.

2.4 Higgs boson production at the LHC

In this section, I will introduce the main production mechanisms of the Higgs boson at hadron collider, with particular focus on the LHC. As seen in the previous chapter, the Higgs boson couples to particles with a strength which is proportional to the particle mass, the most important production mechanisms will involve the coupling of the Higgs boson to the W and Z bosons and the top-quark.

At the LHC the Higgs boson is produced through four production mechanisms. These mechanisms are (in order of decreasing total-rate): gluon fusion (mediated by a top-quark loop), vector boson fusion, VH associated production (where $V = W^{\pm}, Z$) and $t\bar{t}H$ associated production (see Fig. 2.2 for representative diagrams).

An exhaustive study of the four channels will require more space than it is allowed in this thesis and can be found e.g. in the review [34].

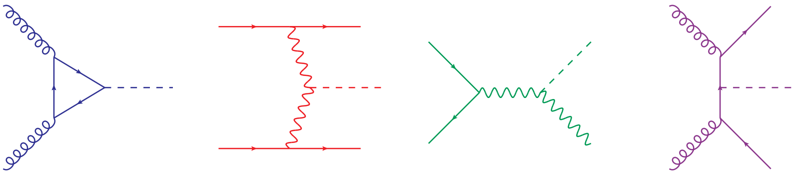

Figure 2.2: Representative Feynman diagrams for the four main Higgs boson production channel at the LHC. From left: gluon fusion (blue), vector-boson fusion (red), VH associated production (green) and $t\bar{t}H$ associated procuction (purple).

The state-of-art predictions for the total rates of the four production channels at the LHC $\sqrt{S} = 8\,\text{TeV}$ are shown in Fig. 2.3 (from [35]). The total cross-section for gluon-fusion is known up to next-to-next-to-leading order (NNLO) in QCD [36–42], including soft gluon resummation up to NNLL [43]. Efforts towards the computation of the NNNLO total cross-section are on-going [44, 45]. Electroweak corrections have also been computed [46, 47], and have been combined with QCD corrections in the multiplicative scheme [48–51] (see Sec. 4.2.2 for an overview on possible QCD-EW combinations). For what concerns VBF, the total cross-section has been computed up to NNLO in QCD [20, 21, 52–54] including EW corrections (in the multiplicative scheme), which have been computed in [55, 56]. As VBF is the main topic of this thesis, details will be given later on (specially in Chapter 4 for what concerns the computation of the total cross-section). Like VBF, VH associated production is also known up to NNLO QCD [57–60] and NLO EW [61]. Finally $t\bar{t}H$ is known up to NLO QCD [62–67].

In the last years, in parallel with the efforts in computing as accurate as possible total rates, lot of energies have been spent in developing tools for fully differential predic-

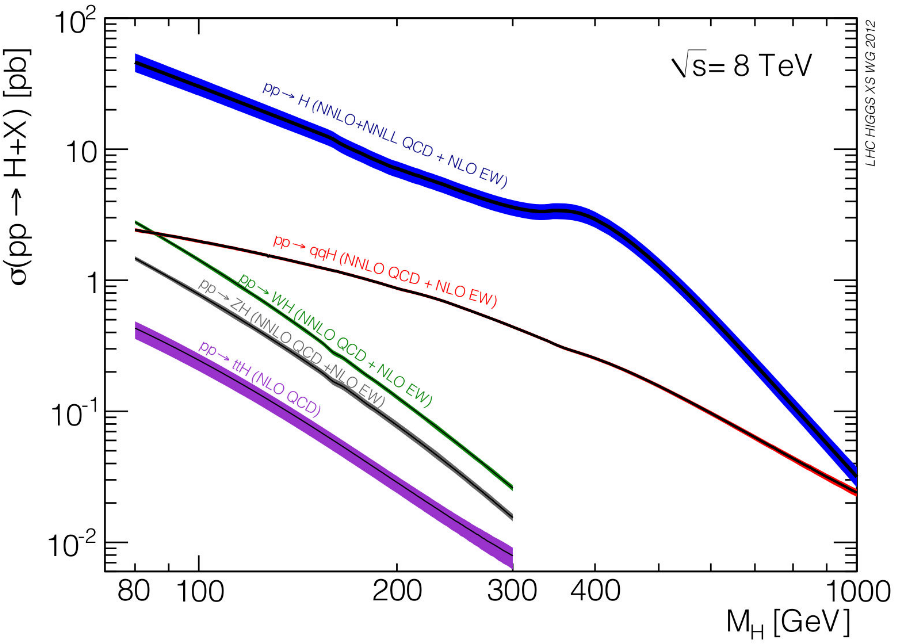

Figure 2.3: Total cross-section predictions for the Higgs boson production at the LHC $\sqrt{S}$ = 8 TeV (from [35]). The colored bands represent the theoretical uncertainties on each prediction.

tion of observables. One such tool, aMC@NLO [68], allows the user to automatically generate the code to generate events at NLO accuracy for virtually any process in the SM (more details will be given in Chapter 5 where VBF will be studied). These events can be passed to a parton shower Monte-Carlo, to have a complete, fully differential picture of the final state. To show the flexibility and the usefulness of such a tool, in Fig. 2.4 I show the Higgs boson transverse-momentum distributions for the production channels discussed above. These distributions are computed at NLO accuracy and correspond to events showered with HERWIG6 [69, 70].

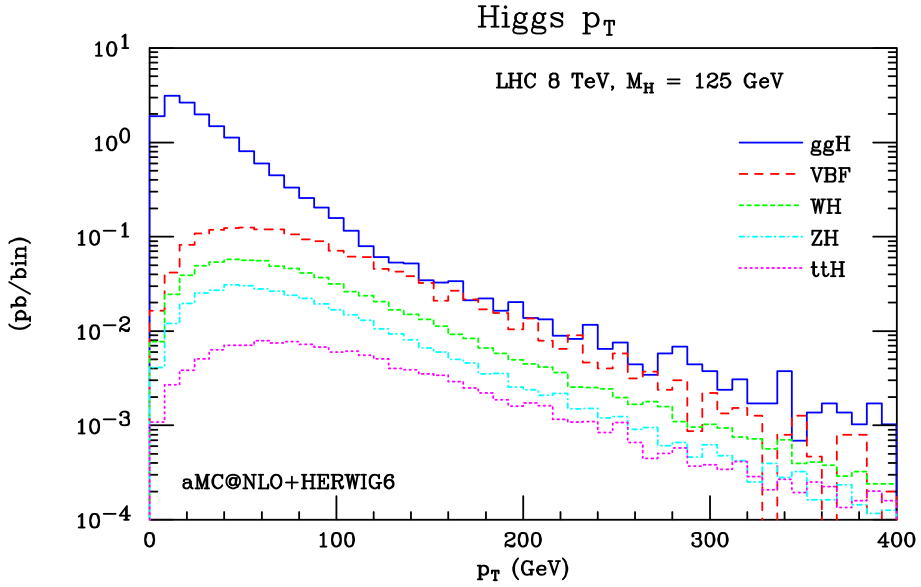

Figure 2.4: Transverse momentum of the Higgs boson in the gluon fusion (blue solid), VBF (red long-dashed), WH (green short-dashed), ZH (cyan dot-dashed) and $t\bar{t}H$ (magenta dotted) production mechanism, for a $M_H = 125\,\text{GeV}$ Higgs boson at the LHC, $\sqrt{S} = 8\,\text{TeV}$. Each curve corresponds to fifty-thousands events generated with aMC@NLO, including NLO and parton-shower corrections. The MSTW 2008 parton distributions [71] have been used. Renormalization and factorization scales are fixed to the Higgs boson mass.

Chapter 3

Vector boson fusion

3.1 Introduction

Vector boson fusion (VBF) is the second Higgs boson production channel in total rate at the LHC. Although its rate is almost one order of magnitude smaller than the dominant production channel, gluon fusion, VBF has played quite an important role in the discovery of the Higgs boson, and will also be crucial for the determination of the Higgs properties. This is because, typically, VBF events are less polluted by QCD radiation than gluon fusion ones, and, due to the particular final state-topology, backgrounds can be more easily suppressed by imposing appropriate selection cuts.
I will begin this chapter with Sec. 3.2, trying to define VBF in a way that is as unambiguous as possible, not only at lowest order, but also in view of including higher order QCD and EW corrections. After this, in Sec. 3.3, by looking at the VBF LO amplitude, I will present the distinguishing features of VBF-like events, which are the presence of two hard jets in the opposite rapidity hemispheres, and the lack of radiation in the central region. I will conclude the chapter with Sec. 3.4 showing that these features are not spoiled even if extra radiation is considered.

3.2 A working definition for VBF

In this section I will look for a definition of VBF which can be safely used in order to consistently compute higher order corrections. In general, the definition of “production-channel” is itself ambiguous, since production channels are always defined on simple conventions typically based on leading-order Feynman diagrams.

While this poses no problems at LO, it might lead to ambiguities when decays of resonant states and/or higher order effects are included. Consider, as a simple example, the class of processes which involve only the electroweak coupling α_{EW} at the leading order, such as Drell-Yan (with the decay into two jets), single-top production and Higgs boson production via coupling with a vector boson. Most of such processes can be easily defined at leading order considering the corresponding resonant intermediate or final states, while some, such as VBF are (quantum-mechanically) ambiguous already at the leading order: $pp \to Hjj$ with vector bosons in the t-channel can interfere with $pp \to HV^{(*)} \to Hjj$, *i.e.*, with Higgs associated production with a vector boson then decaying into two jets. Such interference, however, is quite small everywhere in the phase space and it can formally be reduced to zero by just taking the narrow width limit. This suggests that considering the two processes distinct is a handy approximation, at least at the leading order. For all of the processes in this class, *i.e.*, single-top and Higgs electroweak production, aiming at a better precision by including higher-order QCD effects creates further ambiguities as it opens up more possibilities for interferences (one notable example is tW at NLO overlapping with $t\bar{t}$ production) and the reliability of the approximations made has to be carefully assessed.

In general two complementary approaches can be followed. The first is to consider all interferences exactly, and introduce a gauge-invariant scheme to properly handle the width effects. This can be consistently done at NLO order in QCD and electroweak corrections, following well-known and established techniques, such as the use of the complex-mass scheme [72]. This is the path followed for instance in Ref. [56] for the calculation of QCD and electroweak effects in the order α_{EW}^3 process $pp \to Hjj$. The advantage of this approach is that all interference effects are correctly taken into account in any region of phase space, including where tight cuts might create significant enhancements. This is the only way to proceed when interference effects are similar to or larger than the corrections from higher orders. However, when such effects are small, it offers several drawbacks. The first is the unnecessary complexity of the calculation itself. The second is that the operational separation between the two processes, which can be quite useful at the practical level, for example in experimental analysis, is lost. In this context, even the definition of signal and background might not be meaningful and the distinction possibly leads to confusion. In this case another approach can be followed, to use a simple process definition and to systematically check the impact of higher-order corrections and of interferences, in order to set the ultimate practical precision that can be achieved.

Such a definition for VBF consist in defining VBF as the Higgs production for vanishing quark masses, through direct coupling of the Higgs to vector bosons in the $t-$channel, with color-singlet exchange between the two colliding protons. A diagrammatic representation of this definition is given in Fig. 3.1, where no heavy-quark loops are included in the blobs, while extra (color-singlet) vector bosons can appear

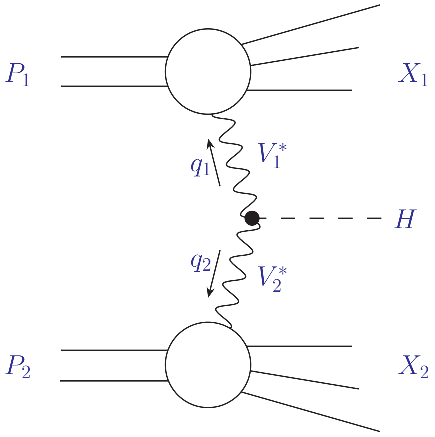

Figure 3.1: Higgs production via the VBF process.

at higher orders.

The reason of such a formulation will become more clear in what follows.

3.3 The lowest order amplitude and VBF event topology

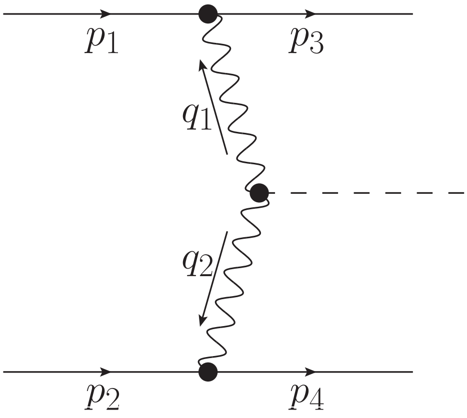

Figure 3.2: LO VBF Feynman diagram.

The most relevant properties of VBF can be deduced by looking at its LO partonic amplitude, corresponding to the diagram in Fig. 3.2. Dubbing p_1, p_2 (p_3, p_4) the momenta of the initial-state (final-state) quarks, this amplitude can be written as (understanding the quark color indexes)

$$\mathcal{M}_{LO}^{VBF} = 2\left(\sqrt{2}G_F\right)^{1/2} M_V^2 \frac{1}{q_1^2 - M_V^2} \frac{1}{q_2^2 - M_V^2} \bar{u}(p_3)\Gamma_\mu \bar{u}(p_1)\, \bar{u}(p_4)\Gamma^\mu \bar{u}(p_2)\,, \quad (3.1)$$

where I have defined

$$q_1 = p_3 - p_1\,, \qquad q_2 = p_4 - p_2\,. \quad (3.2)$$

Γ_μ is the $Vq\bar{q}$ vertex, which for SM interactions between quarks and W and Z bosons can be cast in the from

$$\Gamma_{mu} = \left(\sqrt{2}G_F\right)^{1/2} M_V \left(v_q\gamma_\mu - a_q\gamma_\mu\gamma_5\right), \quad (3.3)$$

written in terms of the usual vector and axial-vector couplings of the gauge bosons to fermions:

$$v_q = a_q = \frac{1}{\sqrt{2}}\,, \quad (3.4)$$

for the W boson, and

$$v_q = I_q - 2Q_q \sin^2\theta_w\,, \qquad a_q = I_q\,, \quad (3.5)$$

for the Z.

From the expression of the LO diagram Eq. (3.1) many of the distinguishing features of VBF can be inferred. First of all, VBF is a t-channel process, with massive bosons in the propagators. This turns into having a finite total cross-section, and in the fact that the bulk of the cross-section corresponds to small momentum transfers $Q_i^2 = -q_i^2$, typically $Q_i^2 \lesssim M_V^2$. This last fact, together with having initial states quarks usually probed at mid-large Bjorken x, is responsible for the very peculiar VBF final state topology: the two final-state quarks tend to travel almost in the same direction as the corresponding initial ones, carrying a substantial fraction of the initial quark momenta. Eventually, these two final state quarks will appear in the detector as two almost back-to-back jets in the forward-backward region, and with a very large invariant mass (typically some TeV at the LHC), whereas the Higgs is normally produced at central rapidities. A candidate VBF event from the CMS experiment, showing this feature, is shown in Fig. 3.3. This topology makes it possible to tag on the two jets in order to select VBF-like events, substantially reducing contamination from background or from other production channels (e.g. Higgs production in gluon fusion in association with jets).

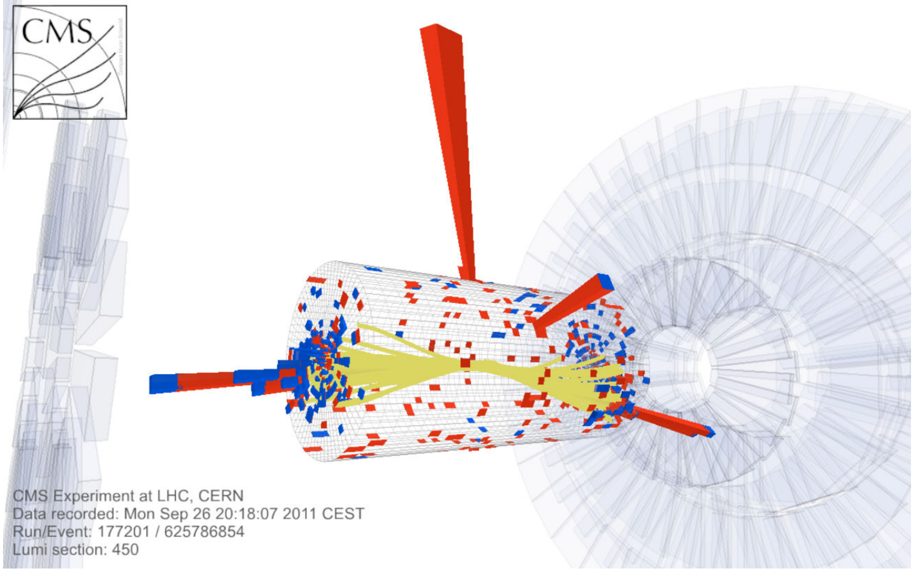

Figure 3.3: Candidate VBF event (with the Higgs boson decaying to two photons) recorded by the CMS experiment during the LHC proton-proton run at $\sqrt{S} = 7\,\text{TeV}$. The two tagging jets (in the forward regions) are visible as tracks in the tracker detector and as energetic deposit in the calorimeters. The two photons are visible in the central regions as energy deposit in the electromagnetic calorimeter.

Another consequence of the final state topology is the extreme suppression of interferences. Partonic channels such as $uu \to Huu$ or $ud \to Hud$ have two diagrams contributing, the one in Fig. 3.2 and the one which is obtained exchanging p_3 with p_4 (and replacing the W with a Z-boson for $ud \to Hud$). The reason of this suppression can be easily understood by looking at the propagators in the case of interferences and in the case of the square of a diagram. The propagator structure of the interferences is

$$\mathrm{PROP}_{intf} = \frac{1}{2p_1 \cdot p_3 + M_V^2}\,\frac{1}{2p_2 \cdot p_4 + M_V^2}\,\frac{1}{2p_1 \cdot p_4 + M_V^2}\,\frac{1}{2p_2 \cdot p_3 + M_V^2}\,, \tag{3.6}$$

while the one from squared diagrams is

$$\mathrm{PROP}_{sqr} = \frac{1}{\left(2p_1 \cdot p_3 + M_V^2\right)^2} \frac{1}{\left(2p_2 \cdot p_4 + M_V^2\right)^2} \,. \tag{3.7}$$

From what I discussed before, in the squared diagram the following relations hold in a (very) rough way

$$p_1 \simeq p_3 \,, \quad p_2 \simeq p_4 \,. \tag{3.8}$$

With this very rough approximation one can calculate the suppression factor or interferences as roughly $\left(\frac{M_V^2}{2p_3 \cdot p_4}\right)^2$, where the denominator is the invariant mass of the two final sate quarks (jets). As said above typical values of the invariant mass are of $O(\mathrm{TeV})$, so that one expects interferences to be suppressed at the per-cent level or below. Indeed, this is confirmed the explicit computation.

3.4 The effect of higher order QCD corrections

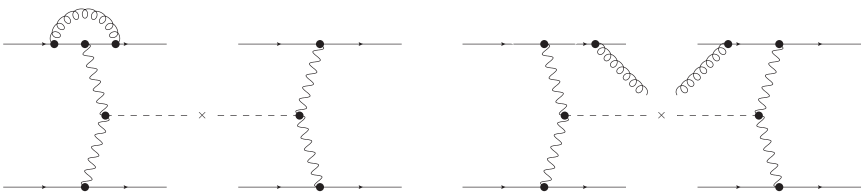

Figure 3.4: Representative virtual (left) and real-emission (right) matrix-elements for factorizable NLO QCD corrections to VBF.

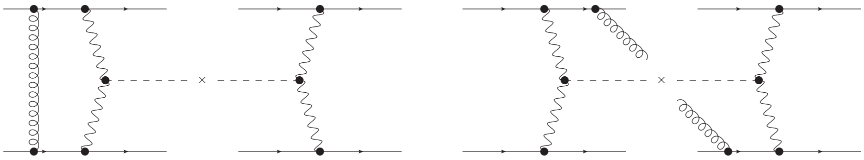

Figure 3.5: Representative virtual (left) and real-emission (right) matrix-elements for non-factorizable NLO QCD corrections to VBF. These matrix elements vanish due to color conservation.

In this paragraph, I will discuss NLO QCD corrections to VBF. In particular I will show that such corrections do not spoil the peculiar event topology presented in Sec. 3.3.

NLO QCD corrections to VBF (treating real and virtual corrections on the same footing) can be classified into two categories: corrections that only affect one quark line, called factorizable corrections, and corrections that link the two quark lines, called non-factorizable corrections. Representative matrix-elements are shown respectively in Fig. 3.4 and in Fig. 3.5.

It is interesting to note that non-factorizable corrections vanish because of color conservation: this can be understood either using a group-theory argument, since they all contain the trace of a single Gell-Mann color matrix $\mathrm{Tr}\,[t_a] = 0$, or explicitly assigning color to the partons, as done in Fig. 3.6.

The only contribution due to non-factorizable QCD corrections comes from QCD corrections to interferences, which, anyway, are extremely small already at LO (as explained in Sec. 3.3). Such contributions have been computed in [56] and are found to be totally negligible, as expected.

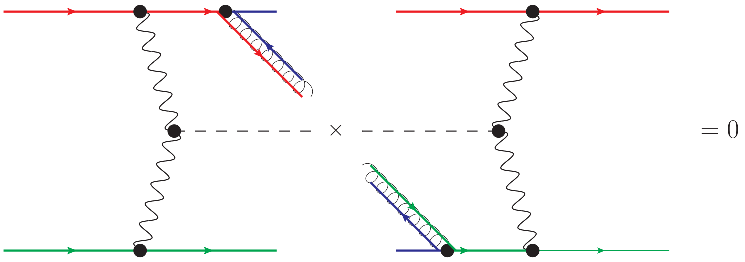

Figure 3.6: Example of color flow in non-factorizable NLO QCD corrections to VBF. The outgoing quark which radiated the gluon carries a color different than the corresponding quark which did not radiate, making the interference to vanish.

Turning now to the factorizable corrections, it is instructive to understand whether the real emission diagrams can alter the event topology described in Sec. 3.3. The most interesting characteristic that was pointed is the fact of having the Higgs boson in a region well separated from that of QCD. In principle, extra QCD emission can pollute the central rapidity region, where the Higgs is produced.

To better understand this let us explicitly consider the case of the radiation of an extra gluon. In order to keep things simpler, I will work in the soft approximation, where, if $k < p_i$ is the gluon momentum, the gluon-quark-quark Feynman rule reduces to

$$V^{\mu}_{qqg,soft} = 2g_s\, T^a_{ij}\, p^{\mu}\,, \tag{3.9}$$

where p is the quark momentum (is the same for both quarks since $k \to 0$), a,μ are the color and Lorentz index of the gluon and i, j are the color index of the outgoing and incoming quark respectively.

Using this expression, the matrix element for VBF plus the emission of a soft gluon with polarization vector ϵ_g is (only the emission from the $p_1 - p_3$ line is considered)

$$\mathcal{M}^{VBF}_{soft} = g_s T^a_{ij} \left(\frac{p_1 \cdot \epsilon_g}{p_1 \cdot k} - \frac{p_3 \cdot \epsilon_g}{p_3 \cdot k} \right) \mathcal{M}^{VBF}_{LO} \,. \tag{3.10}$$

Therefore, the corresponding partonic cross-section is

$$d\sigma^{VBF}_{soft} = d\sigma^{VBF}_{LO} \frac{\alpha_s C_F}{\pi} \frac{dk^0}{k^0} \frac{d\phi}{2\pi} d\cos\theta_g \frac{1-\cos\theta_{13}}{\left(1-\cos\theta_{1g}\right)\left(1-\cos\theta_{3g}\right)} \,, \tag{3.11}$$

where θ_{ij} is the angle between particle i and j:

$$\cos\theta_{ij} = \frac{\vec{p_i} \cdot \vec{p_j}}{\left|\vec{p_i}\right| \left|\vec{p_j}\right|} \,. \tag{3.12}$$

One can rewrite

$$\begin{aligned} & \frac{1-\cos\theta_{13}}{\left(1-\cos\theta_{1g}\right)\left(1-\cos\theta_{3g}\right)} = \\ = \; & \frac{1}{2} \left[\left(\frac{1-\cos\theta_{13}}{\left(1-\cos\theta_{1g}\right)\left(1-\cos\theta_{3g}\right)} + \frac{1}{1-\cos\theta_{1g}} - \frac{1}{1-\cos\theta_{3g}} \right) + (1 \leftrightarrow 3) \right] \\ = \; & W_1 + W_3 \,, \end{aligned} \tag{3.13}$$

such that W_i contains only the collinear divergence $\theta_{ig} \to 0$.
Interestingly, the following relation holds [73] when one averages W_i over the gluon azimuth:

$$\int_0^{2\pi} \frac{d\phi}{2\pi} W_i = \frac{1}{1-\cos\theta_{ig}} \Theta\left(\theta_{13} - \theta_{ig}\right) . \tag{3.14}$$

Eq. (3.14) has an extremely important physical meaning: in the soft approximation, a gluon is emitted at small angles with respect to the particles that radiate it, or, equivalently, that radiation at large angles is suppressed. This phenomenon is called angular ordering.

I will now show the derivation of the angular-ordering condition Eq. (3.14). In particular I will focus on W_1, the proof for W_3 being completely analogous. I parametrize the three-momenta $\vec{p}_1$, $\vec{p}_3$, $\vec{k}$ as

$$\begin{aligned}
\vec{p}_1 &= \left|\vec{p}_1\right|(0,\, 0,\, 1)\,, && (3.15)\\
\vec{p}_3 &= \left|\vec{p}_3\right|(\sin\theta_{13},\, 0,\, \cos\theta_{13})\,, && (3.16)\\
\vec{k} &= \left|\vec{k}\right|\left(\sin\theta_{1g}\cos\phi,\, \sin\theta_{1g}\sin\phi,\, \cos\theta_{1g}\right). && (3.17)
\end{aligned}$$

The angle θ_{3g} is related to the gluon azimuth by the relation

$$\cos\theta_{3g} = \sin\theta_{13}\sin\theta_{1g}\cos\phi + \cos\theta_{13}\cos\theta_{1g}\,, \tag{3.18}$$

and can be cast in the form

$$1 - \cos\theta_{3g} = a - b\cos\phi\,, \tag{3.19}$$

with

$$\begin{aligned}
a &= 1 - \cos\theta_{13}\cos\theta_{1g}\,, && (3.20)\\
b &= \sin\theta_{13}\sin\theta_{1g}\,. && (3.21)
\end{aligned}$$

If I now define

$$z = \exp(\mathrm{i}\phi)\,, \tag{3.22}$$

the following identity holds:

$$\mathcal{I}_1 \equiv \int_0^{2\pi} \frac{d\phi}{2\pi}\frac{1}{1-\cos\theta_{3g}} = \frac{1}{\mathrm{i}\pi b}\oint \frac{dz}{(z-z_+)(z-z_-)}\,, \tag{3.23}$$

where the zeros of the denominator are

$$z_\pm = \frac{a}{b} \pm \sqrt{\frac{a^2}{b^2} - 1}\,. \tag{3.24}$$

Among the two zeros, only z_- lies inside the unit circle, therefore one obtains

$$\mathcal{I}_1 = \sqrt{\frac{1}{a^2 - b^2}} = \frac{1}{\left|\cos\theta_{1g} - \cos\theta_{13}\right|}\,. \tag{3.25}$$

Finally the azimuthal average of W_1 can be expressed in terms of $\mathcal{I}_1$, obtaining

$$\begin{aligned}\int_o^{2\pi}\frac{d\phi}{2\pi}W_1 &= \frac{1}{2(1-\cos\theta_{1g})}\Big[1+(\cos\theta_{1g}-\cos\theta_{13})\Big]\mathcal{I}_1 = \\ &= \begin{cases}\frac{1}{1-\cos\theta_{1g}} & \text{if} \quad \theta_{1g}<\theta_{13} \\ 0 & \text{else}\end{cases}, \end{aligned} \tag{3.26}$$

which completes the proof.

What I have just shown is that, considering the case of a soft gluon, extra QCD radiation in VBF is bound to be close in phase-space to the outgoing quarks. When the exact real emission matrix-elements are considered, also including contributions with a gluon in the initial state, no substantial modification of the radiation pattern is found. The bottom line is that radiation in the central rapidity region, hence emitted at large angles with respect to the quarks $1,3$, is usually suppressed in VBF, and this is a direct consequence of the fact that no color is exchanged between the protons. A comparison of the rapidity distribution for the third jet in VBF and in Higgs production via gluon fusion (where the two protons are color connected), is shown in Fig. 3.7, where it is possible to appreciate the different radiation pattern.

This thesis will be devoted to present the most accurate predictions for VBF. In Chapter 4 I will study the impact of NLO and NNLO QCD corrections on the VBF total cross-section, and I will show how the theoretical uncertainties greatly reduce after their inclusion. In Chapter 5 I will compute NLO QCD corrections to VBF matched with parton shower. This will allow to study the impact of corrections on differential observables, and to study with more detail the extra jet radiation pattern.

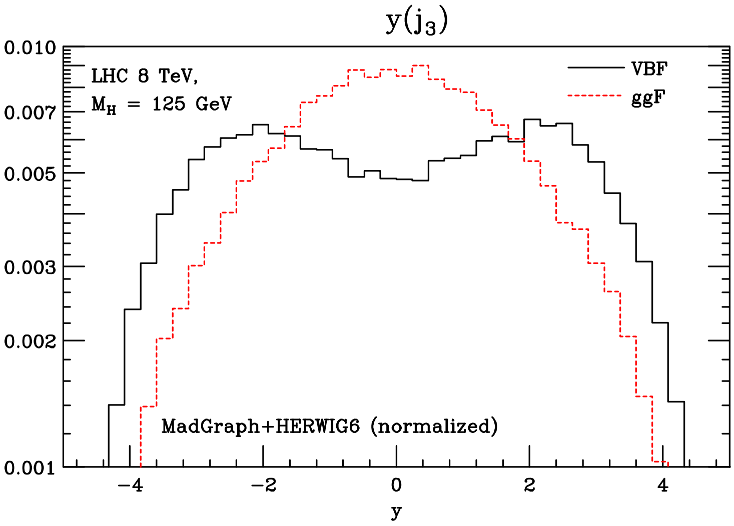

Figure 3.7: Rapidity distribution for the third jet in VBF (black solid) and in Higgs production via gluon fusion (red dashed), at the LHC $\sqrt{S} = 8\,\text{TeV}$, for a $M_H = 125\,\text{GeV}$ Higgs boson. Events have been generated with MadGraph [74] and showered with HERWIG6 [69, 70]. Hadrons are clustered into jets using the anti-k_T algorithm [75] as implemented in FastJet [76], with $\Delta R = 0.5$, $p_T > 20\,\text{GeV}$. Distributions are normalized to 1.

Chapter 4

Precise predictions for the total VBF cross-section

The results presented in this chapter are based on [20, 21, 25–27] and on the VBF chapter of [23, 24].

4.1 Introduction

This chapter is devoted to the presentation of the state-of-the-art predictions for the VBF total cross-section. Lot of efforts from various groups have been spent in order to provide predictions as accurate as possible, resulting in the VBF total cross-section being now one of the most (if not the most) precise prediction for a total-rate at the LHC.

In Sec. 4.2 I will first describe the details of the computation of the NNLO QCD corrections published in [21,25], and show how these predictions can be further improved by including the NLO electroweak (EW) corrections and effects due to the Higgs virtuality.
I will present the results for the LHC with a center-of-mass energy $\sqrt{S} = 8\,\text{TeV}$ (as for the 2012 run) in Sec. 4.3, then move to conclusions in Sec. 4.4.

4.2 Higher order corrections to VBF

According to the definition of VBF given in Sec. 3.2, higher order corrections can be classified as genuine “VBF-like” contributions and “non VBF-like” ones. I will now present the contributions belonging to each of the two classes.
“VBF-like” contributions:

- Factorizable contributions in QCD, where “factorizable” means that they can be represented as in Fig. 3.1. This class will be evaluated exactly in Sec. 4.2.1.1, and gives the bulk of the QCD corrections up to order α_s^2 to a precision better than 1%.
- Non-factorizable contributions in QCD, *i.e.*corrections in which colored particles (in a color-singlet state) are exchanged between the colliding protons. They will be studied in Sec. 4.2.1.2, where they are proven to be color suppressed (of order α_s^2/N_c^2) with respect the factorizable ones, and they are estimated to contribute less than 1% to the total VBF cross section.
- Electroweak corrections to diagrams in Fig. 3.1. These are relevant corrections which have been calculated in Ref. [56]. Their combination with the NNLO QCD ones has been presented in Ref. [23] and will be briefly reported in Sec. 4.2.2.
- Higgs boson finite width effects. These effects arise from the inclusion of the Higgs boson width in the calculation, which need to be considered specially in the case (now excluded) of a heavy Higgs boson. This can be done according to many schemes which give equivalent results for a light Higgs, but can sizably differ for a heavier one. The computation of these effects for VBF is discussed in Sec. 4.2.3.

“Non-VBF like” contributions:

- Single-quark line contributions, as calculated in Ref. [77]. These effects are smaller than 1% in differential cross sections.
- Interferences between VBF diagrams, which are known up to NLO in QCD and electroweak as calculated in Ref. [56]. These effects are found to be very small already at LO, which can be easily included.
- Interferences between VBF and associated WH and WZ production at NLO in QCD and electroweak, as calculated in Ref. [56]. Also these effects can be easily calculated at LO and are found to be completely negligible, and vanishing in the narrow-width approximation.

- Interferences with the top-loop mediated Higgs production, Refs. [78, 79] and contributions calculated in Sec. 4.2.1.3. These effects are found to contribute less than 1% to the total cross section.

- t-channel vector boson production in presence of heavy-quark loops (triangles and boxes), see Sec. 4.2.1.3. These effects are estimated to contribute less than 1% to the total cross section.

4.2.1 QCD corrections to VBF

As has been explained in Chapter 3, QCD corrections to VBF factorize in such a way that contributions arising from gluon exchange between the quark lines vanish. Up to NLO this fact, together with the large suppression of interferences, allow to consider the two quark-lines as fully independent. From this point of view, VBF is nothing more than a double Deep-Inelastic Scattering process, where the vector bosons fuse into the Higgs. Therefore, the long known NLO QCD corrections to DIS [80] can be used to compute the VBF cross-section at NLO.

This has indeed been exploited in the first computation of the NLO QCD corrections to VBF more than twenty years ago [53], and is known as the “structure function approach”.

At NNLO some extra non-vanishing contributions arise, which break the factorization which underlies the structure function approach. An estimate (or the explicit computation if possible) of such contributions is mandatory in order to assess if the structure-function approach can be extended up to NNLO, and will be done in what follows.
The factorization-violating contributions can be classified into two groups: the first group consists in the contribution from the exchange of two gluons in a color singlet between the protons, where the gluons can be both virtual, real-virtual and both real. The exact inclusion of this contributions is, unfortunately, still beyond reach.
The second group of contributions consist in diagrams involving the third generation of quarks, where the Higgs can couple to the top.

As it will be shown in Sec. 4.2.1.2 and Sec. 4.2.1.3, an estimate of these contributions suggests that they can be neglected with respect to the NNLO QCD corrections included in the structure function approach.

4.2.1.1 Structure function approach

The structure function approach is based on the observation that to a very good approximation the VBF process can be described as a double deep-inelastic scattering process (DIS), see Fig. 3.1, where two (virtual) vector-bosons V_i (independently) emitted from the hadronic initial states fuse into a Higgs boson.

Considering VBF as the product of two DIS processes, the total cross-section total cross-section can be factorized as the product of the electroweak matrix element $\mathcal{M}^{\mu\rho}$, *i.e.*, $V_1^\mu V_2^\rho \to H$, which in the SM reads

$$\mathcal{M}^{\mu\nu} = 2\left(\sqrt{2}G_F\right)^{1/2} M_V^2 g^{\mu\nu}, \tag{4.1}$$

and the DIS hadronic tensor $W_{\mu\nu}$:

$$\begin{aligned} d\sigma \; = \; & \frac{1}{2S} 2G_F^2 M_{V_1}^2 M_V^2 \frac{1}{\left(Q_1^2+M_V^2\right)^2} \frac{1}{\left(Q_2^2+M_V^2\right)^2} \\ & \times W_{\mu\nu}\left(x_1,Q_1^2\right) \mathcal{M}^{\mu\rho} \mathcal{M}^{*\nu\sigma} W_{\rho\sigma}\left(x_2,Q_2^2\right) \\ & \times \frac{d^3P_{X_1}}{(2\pi)^3\, 2E_{X_1}} \frac{d^3P_{X_2}}{(2\pi)^3\, 2E_{X_2}} ds_1 ds_2 \frac{d^3P_H}{(2\pi)^3\, 2E_H} \\ & \times (2\pi)^4 \delta^4\left(P_1+P_2-P_{X_1}-P_{X_2}-P_H\right). \end{aligned} \tag{4.2}$$

Here G_F is Fermi's constant and $\sqrt{S}$ is the center-of-mass energy of the collider. $Q_i^2 = -q_i^2$, $x_i = Q_i^2/(2P_i \cdot q_i)$ are the usual DIS variables, $s_i = (P_i + q_i)^2$ are the invariant masses of the i-th proton remnant, and M_{V_i} denote the vector-boson masses, see Fig. 3.1. The three-particle phase space dPS of the VBF process is given in the second line of Eq. (4.2). It is discussed in detail in App. A.

Higgs production in VBF requires the hadronic tensor $W_{\mu\nu}$ for DIS neutral and charged current reactions, *i.e.*, the scattering off a Z as well as off a $W^\pm$-boson. It is commonly expressed in terms of the standard DIS structure functions $F_i(x,Q^2)$ with $i = 1,2,3$. *i.e.* F_i^V with $i = 1,2,3$ and $V \in \{Z, W^\pm\}$. Thus,

$$\begin{aligned} W_{\mu\nu}\left(x_i,Q_i^2\right) \; = \; & \left(-g_{\mu\nu} + \frac{q_{i,\mu}q_{i,\nu}}{q_i^2}\right) F_1(x_i,Q_i^2) + \frac{\hat{P}_{i,\mu}\hat{P}_{i,\nu}}{P_i \cdot q_i} F_2(x_i,Q_i^2) + \\ & + \mathrm{i}\epsilon_{\mu\nu\alpha\beta} \frac{P_i^\alpha q_i^\beta}{2P_i \cdot q_i} F_3(x_i,Q_i^2), \end{aligned} \tag{4.3}$$

where $\epsilon_{\mu\nu\alpha\beta}$ is the completely antisymmetric tensor and the momentum $\hat{P}_i$ reads

$$\hat{P}_{i,\mu} = P_{i,\mu} - \frac{P_i \cdot q_i}{q_i^2} q_{i,\mu} \,. \tag{4.4}$$

The evaluation of Eq. (4.1) and Eq. (4.3) leads to the explicit result for the squared hadronic tensor in Eq. (4.2) in terms of the DIS structure functions [53] (see also the review [34]) :

$$\begin{aligned}
&W_{\mu\nu}\left(x_1,Q_1^2\right)\mathcal{M}^{\mu\rho}\mathcal{M}^{*\nu\sigma}W_{\rho\sigma}\left(x_2,Q_2^2\right) = 4\sqrt{2}G_F M_{V_i}^4 \\
&\times \Bigg\{ F_1\left(x_1,Q_1^2\right)F_1\left(x_2,Q_2^2\right)\left[2+\frac{(q_1\cdot q_2)^2}{q_1^2 q_2^2}\right] \\
&\quad + \frac{F_1\left(x_1,Q_1^2\right)F_2\left(x_2,Q_2^2\right)}{P_2\cdot q_2}\left[\frac{(P_2\cdot q_2)^2}{q_2^2}+\frac{1}{q_1^2}\left(P_2\cdot q_1-\frac{P_2\cdot q_2}{q_2^2}q_1\cdot q_2\right)^2\right] \\
&\quad + \frac{F_2\left(x_1,Q_1^2\right)F_1\left(x_2,Q_2^2\right)}{P_1\cdot q_1}\left[\frac{(P_1\cdot q_1)^2}{q_1^2}+\frac{1}{q_2^2}\left(P_1\cdot q_2-\frac{P_1\cdot q_1}{q_1^2}q_1\cdot q_2\right)^2\right] \\
&\quad + \frac{F_2\left(x_1,Q_1^2\right)F_2\left(x_2,Q_2^2\right)}{(P_1\cdot q_1)(P_2\cdot q_2)} \\
&\quad \times \left(P_1\cdot P_2 - \frac{(P_1\cdot q_1)(P_2\cdot q_1)}{q_1^2} - \frac{(P_1\cdot q_2)(P_2\cdot q_2)}{q_2^2}\right. \\
&\quad \left. + \frac{(P_1\cdot q_1)(P_2\cdot q_2)(q_1\cdot q_2)}{q_1^2 q_2^2}\right)^2 \\
&\quad + \frac{F_3\left(x_1,Q_1^2\right)F_3\left(x_2,Q_2^2\right)}{2(P_1\cdot q_1)(P_2\cdot q_2)}\Big((P_1\cdot P_2)(q_1\cdot q_2)-(P_1\cdot q_2)(P_2\cdot q_1)\Big)\Bigg\} \,.
\end{aligned} \tag{4.5}$$

At this stage it remains to insert the DIS structure functions F_i^V with $i = 1,2,3$ and $V \in \{Z, W^\pm\}$. At NLO in QCD, explicit expression have been given in Ref. [53] using the results of Ref. [80]. For the necessary generalization beyond NLO, I will now briefly review the basic formulae.

Thanks to the QCD factorization theorem, structure functions can be expressed as convolutions of the PDFs in the proton and the short-distance Wilson coefficient functions C_i. The gluon PDF at the factorization scale μ_F is denoted by $g(x,\mu_F)$ and the quark (or anti-quark) PDF by $q_i(x,\mu_F)$ (or $\bar{q}_i(x,\mu_F)$) for a specific quark flavor i. The latter PDFs appear in the following combinations,

$$q_{\rm s} = \sum_{i=1}^{n_f}\left(q_i+\bar{q}_i\right), \qquad q_{\rm ns}^{\rm v} = \sum_{i=1}^{n_f}\left(q_i-\bar{q}_i\right), \tag{4.6}$$

$$q^{+}_{\mathrm{ns},i} = \Big(q_i + \bar{q}_i\Big) - q_{\mathrm{s}}\,, \qquad\qquad q^{-}_{\mathrm{ns},i} = \Big(q_i - \bar{q}_i\Big) - q^{\mathrm{v}}_{\mathrm{ns}}\,, \tag{4.7}$$

as the singlet distribution q_{s}, the (non-singlet) valence distribution $q^{\mathrm{v}}_{\mathrm{ns}}$ as well as flavor asymmetries of $q^{\pm}_{\mathrm{ns},i}$. All of them are subject to well-defined transformation properties under the flavor isospin, see e.g. [81, 82].

For the neutral current Z-boson exchange the DIS structure functions F^Z_i can be written as follows:

$$\begin{aligned} F^Z_i(x,Q^2) \;=\; & f_i(x) \int\limits_0^1 dz \int\limits_0^1 dy\, \delta(x-yz) \sum_{j=1}^{n_f} \Big(v_j^2 + a_j^2\Big) \times \qquad (4.8) \\ & \times \Big\{ q^{+}_{\mathrm{ns},j}(y,\mu_F)\, C^{+}_{i,\mathrm{ns}}(z,Q,\mu_R,\mu_F) + q_{\mathrm{s}}(y,\mu_F)\, C_{i,\mathrm{q}}(z,Q,\mu_R,\mu_F) + \\ & + g(y,\mu_F)\, C_{i,\mathrm{g}}(z,Q,\mu_R,\mu_F) \Big\}\,, \\ F^Z_3(x,Q^2) \;=\; & \int\limits_0^1 dz \int\limits_0^1 dy\, \delta(x-yz) \sum_{i=1}^{n_f} 2\, v_i\, a_i \times \qquad (4.9) \\ & \times \Big\{ q^{-}_{\mathrm{ns},i}(y,\mu_F)\, C^{-}_{3,\mathrm{ns}}(z,Q,\mu_R,\mu_F) + q^{\mathrm{v}}_{\mathrm{ns}}(y,\mu_F)\, C^{\mathrm{v}}_{3,\mathrm{ns}}(z,Q,\mu_R,\mu_F) \Big\}\,, \end{aligned}$$

where $i = 1,2$ and the pre-factors in Eq. (4.8) are $f_1(x) = 1/2$, $f_2(x) = x$. The vector- and axial-vector coupling constants v_i and a_i in Eq. (4.8) are given by (see also Sec. 3.3)

$$v_i^2 + a_i^2 \;=\; \left\{ \begin{array}{ll} \frac{1}{4} + \left(\frac{1}{2} - \frac{4}{3}\sin^2\theta_w\right)^2 & u\text{-type quarks}\,, \\ \frac{1}{4} + \left(\frac{1}{2} - \frac{2}{3}\sin^2\theta_w\right)^2 & d\text{-type quarks}\,, \end{array} \right. \tag{4.10}$$

and, likewise, in Eq. (4.9),

$$2 v_i a_i \;=\; \left\{ \begin{array}{ll} \frac{1}{2} - \frac{4}{3}\sin^2\theta_w & u\text{-type quarks}\,, \\ \frac{1}{2} - \frac{2}{3}\sin^2\theta_w & d\text{-type quarks}\,. \end{array} \right. \tag{4.11}$$

The coefficient functions C_i in Eqs. (4.8)–(4.9) parameterize the hard partonic scattering process. They depend only on the scaling variable x, and on dimensionless ratios of Q^2, μ_F and the renormalization scale μ_R. The perturbative expansion of C_i in the strong coupling α_s up to two loops reads in the non-singlet sector,

$$\begin{aligned}
C^{+}_{i,\mathrm{ns}}(x) &= \delta(1-x) + a_s\left\{c^{(1)}_{i,\mathrm{q}} + L_M P^{(0)}_{\mathrm{qq}}\right\} && (4.12)\\
&\quad + a_s^2\left\{c^{(2),+}_{i,\mathrm{ns}} + L_M\left(P^{(1),+}_{\mathrm{ns}} + c^{(1)}_{i,\mathrm{q}}(P^{(0)}_{\mathrm{qq}} - \beta_0)\right) + L_M^2\left(\frac{1}{2}P^{(0)}_{\mathrm{qq}}(P^{(0)}_{\mathrm{qq}} - \beta_0)\right)\right.\\
&\quad \left. + L_R\beta_0 c^{(1)}_{i,\mathrm{q}} + L_R L_M \beta_0 P^{(0)}_{\mathrm{qq}}\right\},\\
C^{-}_{3,\mathrm{ns}}(x) &= \delta(1-x) + a_s\left\{c^{(1)}_{3,\mathrm{q}} + L_M P^{(0)}_{\mathrm{qq}}\right\} && (4.13)\\
&\quad + a_s^2\left\{c^{(2),-}_{3,\mathrm{ns}} + L_M\left(P^{(1),-}_{\mathrm{ns}} + c^{(1)}_{3,\mathrm{q}}(P^{(0)}_{\mathrm{qq}} - \beta_0)\right) + L_M^2\left(\frac{1}{2}P^{(0)}_{\mathrm{qq}}(P^{(0)}_{\mathrm{qq}} - \beta_0)\right)\right.\\
&\quad \left. + L_R\beta_0 c^{(1)}_{3,\mathrm{q}} + L_R L_M \beta_0 P^{(0)}_{\mathrm{qq}}\right\},
\end{aligned}$$

where $a_s = \alpha_s(\mu_R)/(4\pi)$ and $i = 1,2$ in Eq. (4.12). The complete scale dependence, *i.e.* the towers of logarithms in $L_M = \ln(Q^2/\mu_F^2)$ and $L_R = \ln(\mu_R^2/\mu_F^2)$ (keeping $\mu_R \neq \mu_F$), has been derived by renormalization group methods (see, e.g. [83]) in terms of splitting functions $P^{(l)}_{ij}$ and the coefficients of the QCD beta function, β_l. In the normalization of the expansion parameter, $a_s = \alpha_s/(4\pi)$, the conventions for the running coupling are

$$\frac{d}{d\ln\mu^2}\,\frac{\alpha_s}{4\pi} \equiv \frac{d a_s}{d\ln\mu^2} = -\beta_0 a_s^2 - \ldots\,, \qquad \beta_0 = \frac{11}{3}C_A - \frac{2}{3}n_f\,, \qquad (4.14)$$

with β_0 the usual expansion coefficient of the QCD beta function, $C_A = 3$ and n_f the number of light flavors.

Note, that the valence coefficient function $C^{\mathrm{v}}_{3,\mathrm{ns}}$ in Eq. (4.13) is defined as $C^{\mathrm{v}}_{3,\mathrm{ns}} = C^{-}_{3,\mathrm{ns}} + C^{\mathrm{s}}_{3,\mathrm{ns}}$. However $C^{\mathrm{s}}_{3,\mathrm{ns}} \neq 0$ only at three-loop order, so that Eq. (4.13) suffices with $C^{\mathrm{v}}_{3,\mathrm{ns}} = C^{-}_{3,\mathrm{ns}}$ up to NNLO. In the singlet sector

$$\begin{aligned}
C_{i,\mathrm{q}}(x) &= \delta(1-x) + a_s\left\{c^{(1)}_{i,\mathrm{q}} + L_M P^{(0)}_{\mathrm{qq}}\right\} && (4.15)\\
&\quad + a_s^2\left\{c^{(2)}_{i,\mathrm{q}} + L_M\left(P^{(1)}_{\mathrm{qq}} + c^{(1)}_{i,\mathrm{q}}(P^{(0)}_{\mathrm{qq}} - \beta_0) + c^{(1)}_{i,\mathrm{g}}P^{(0)}_{\mathrm{gq}}\right)\right.\\
&\quad + L_M^2\left(\frac{1}{2}P^{(0)}_{\mathrm{qq}}(P^{(0)}_{\mathrm{qq}} - \beta_0) + \frac{1}{2}P^{(0)}_{\mathrm{qg}}P^{(0)}_{\mathrm{gq}}\right)\\
&\quad \left. + L_R\beta_0 c^{(1)}_{i,\mathrm{q}} + L_R L_M \beta_0 P^{(0)}_{\mathrm{qq}}\right\},
\end{aligned}$$

$$
\begin{aligned}
C_{i,\mathrm{g}}(x) \;=\;& a_s \Big\{ c^{(1)}_{i,\mathrm{g}} + L_M P^{(0)}_{\mathrm{qg}} \Big\} \\
&+ a_s^2 \Big\{ c^{(2)}_{i,\mathrm{g}} + L_M \Big(P^{(1)}_{\mathrm{qg}} + c^{(1)}_{i,\mathrm{q}} P^{(0)}_{\mathrm{qg}} + c^{(1)}_{i,\mathrm{g}} (P^{(0)}_{\mathrm{gg}} - \beta_0) \Big) \\
&+ L_M^2 \Big(\frac{1}{2} P^{(0)}_{\mathrm{qq}} P^{(0)}_{\mathrm{qg}} + \frac{1}{2} P^{(0)}_{\mathrm{qg}} (P^{(0)}_{\mathrm{gg}} - \beta_0) \Big) \\
&+ L_R \beta_0 c^{(1)}_{i,\mathrm{g}} + L_R L_M \beta_0 P^{(0)}_{\mathrm{qg}} \Big\} ,
\end{aligned} \tag{4.16}
$$

where again $i = 1,2$ in Eq. (4.15). The quark-singlet contribution contains the so-called pure-singlet part, $C_{i,\mathrm{q}} = C^{+}_{i,\mathrm{ns}} + C_{i,\mathrm{ps}}$, *i.e.* $P^{(1)}_{\mathrm{qq}} = P^{(1),+}_{\mathrm{ns}} + P^{(1)}_{\mathrm{ps}}$ and $c^{(2)}_{i,\mathrm{q}} = c^{(2),+}_{i,\mathrm{ns}} + c^{(2)}_{i,\mathrm{ps}}$ in Eq. (4.15). Note that $C_{i,\mathrm{ps}} \neq 0$ from two-loop order. The DIS coefficient functions $c^{(l)}_{i,\mathrm{k}}$ are known to NNLO from Refs. [84–87], likewise, NNLO evolution of the PDFs has been determined in Refs. [81, 88] and even the hard corrections at order α_s^3 are available [89, 90]. Accurate parameterizations of all coefficient functions in Eqs. (4.12)–(4.16) can be taken e.g. from Refs. [89,90] and the splitting functions $P^{(l)}_{ij}$ are given e.g. in Refs. [81, 88] [1]. All products in Eqs. (4.12)–(4.16) are understood as Mellin convolutions. They can be easily evaluated in terms of harmonic polylogarithms $H_{\vec{m}}(x)/(1 \pm x)$ up to weight 4, see [91], which can be evaluated using the FORTRAN package [92].

For the charged current case with $W^{\pm}$-boson exchange the DIS structure functions $F_i^{W^{\pm}}$ are given by,

$$
\begin{aligned}
F_i^{W^-}(x,Q^2) =& \frac{1}{2} f_i(x) \int_0^1 dz \int_0^1 dy\, \delta(x-yz) \frac{1}{n_f} \sum_{j=1}^{n_f} \left(v_j^2 + a_j^2 \right) \times \\
& \times \Big\{ \delta q^{-}_{\mathrm{ns}}(y,\mu_F)\, C^{-}_{i,\mathrm{ns}}(z,Q,\mu_R,\mu_F) + q_{\mathrm{s}}(y,\mu_F)\, C_{i,\mathrm{q}}(z,Q,\mu_R,\mu_F) + \\
& + g(y,\mu_F)\, C_{i,\mathrm{g}}(z,Q,\mu_R,\mu_F) \Big\} ,
\end{aligned} \tag{4.17}
$$

$$
\begin{aligned}
F_3^{W^-}(x,Q^2) =& \frac{1}{2} \int_0^1 dz \int_0^1 dy\, \delta(x-yz) \frac{1}{n_f} \sum_{i=1}^{n_f} 2 v_i a_i \times \\
& \times \Big\{ \delta q^{+}_{\mathrm{ns}}(y,\mu_F)\, C^{+}_{3,\mathrm{ns}}(z,Q,\mu_R,\mu_F) + q^{\mathrm{v}}_{\mathrm{ns}}(y,\mu_F)\, C^{\mathrm{v}}_{3,\mathrm{ns}}(z,Q,\mu_R,\mu_F) \Big\} ,
\end{aligned} \tag{4.18}
$$

---

[1] Note, that with the conventions of Refs. [81, 88–90] both the pure-singlet and the gluon coefficient functions as well as the splitting functions $P^{(0)}_{\mathrm{qg}}$ and $P^{(1)}_{\mathrm{qg}}$ in Eqs. (4.12)–(4.16) need to be divided by a factor $2n_f$ to account for the contribution of **one** individual quark flavor (not the anti-quark).

where, as above, $C_{i,\mathrm{q}} = C^{+}_{i,\mathrm{ns}} + C_{i,\mathrm{ps}}$ and, also, $C^{\mathrm{v}}_{3,\mathrm{ns}} = C^{-}_{i,\mathrm{ns}}$ up to two-loop order. The asymmetry $\delta q^{\pm}_{\mathrm{ns}}$ parametrizes the iso-triplet component of the proton, *i.e.* $u \neq d$ and so on. It is defined as

$$\delta q^{\pm}_{\mathrm{ns}} \;=\; \sum_{i \in u-\mathrm{type}} \sum_{j \in d-\mathrm{type}} \left\{ \left(q_i \pm \bar{q}_i \right) - \left(q_j \pm \bar{q}_j \right) \right\} . \tag{4.19}$$

Its numerical impact is expected to be small though. The respective results for $F_i^{W^+}$ are obtained from Eqs. (4.17)–(4.18) with the simple replacement $\delta q^{\pm}_{\mathrm{ns}} \to -\delta q^{\pm}_{\mathrm{ns}}$.

The vector- and axial-vector coupling constants v_i and a_i are given by

$$v_i = a_i = \frac{1}{\sqrt{2}} . \tag{4.20}$$

The coefficient functions in Eqs. (4.17)–(4.18) including their dependence on the factorization and the renormalization scales can be obtained from Eqs. (4.12)–(4.16) with the help of the following simple substitutions $c^{(2),+}_{i,\mathrm{ns}} \leftrightarrow c^{(2),-}_{i,\mathrm{ns}}$, $c^{(2),-}_{3,\mathrm{ns}} \leftrightarrow c^{(2),+}_{3,\mathrm{ns}}$ and $P^{(1),+}_{\mathrm{ns}} \leftrightarrow P^{(1),-}_{\mathrm{ns}}$ and so on. Again, all expressions for the coefficient and splitting functions are given in Refs. [89, 90] and [81, 88], respectively.

Eq. (4.2) with the explicit expressions for the DIS structure functions inserted provides the backbone of the NNLO QCD predictions for Higgs production in VBF. However, as emphasized above, the underlying factorization is not exact beyond NLO and therefore the non-factorizable corrections need to be estimated. This will be done in the following.

4.2.1.2 Non-factorizable contributions

In order to assess the quality of the factorization approach, I now turn to estimate the size of non-factorizable contributions, *i.e.* those contributions which come from diagrams involving the exchange of gluons between the two quark lines (not included in the structure function approach).

Neglecting interferences between t- and u-channel diagrams, which are, as said, kinematically suppressed, this class of diagrams vanishes at NLO because of color conservation, but contributes at NNLO for the first time. Here, the notion “class of diagrams” refers to a gauge invariant, finite subset of the diagrams. Examples of non-factorizable diagrams are shown in Fig. 4.1.

Before presenting a detailed numerical estimate of the size of the non-factorizable

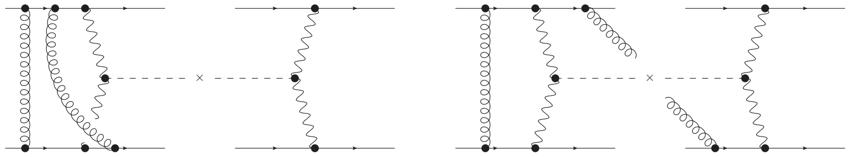

Figure 4.1: Examples of squared matrix elements contributing at NNLO to VBF involving a double gluon exchange between the two quark lines.

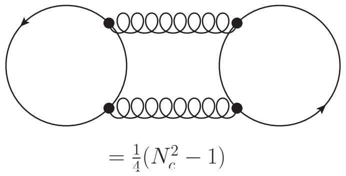

Figure 4.2: Color configurations associated to non-factorizable double-gluon exchange corrections to VBF at NNLO.

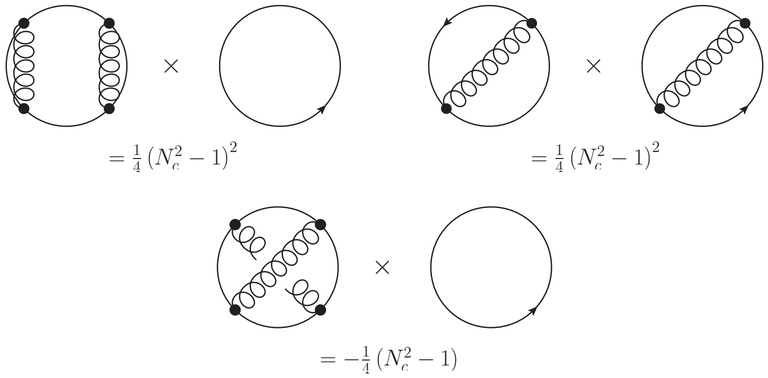

Figure 4.3: Color configurations associated to factorizable corrections to VBF at NNLO.

contributions, I briefly recall two general arguments from Refs. [20,25] justifying their omission.

The first argument is based on the study of the associated color factors. The possible color configurations for factorizable and non-factorizable corrections are shown in Figs. 4.2 and 4.3, respectively, together with the associated color factors. The color factor appearing in the factorizable corrections is $(N_c^2 - 1)^2/4 = 16$, while it is $(N_c^2 - 1)/4 = 2$ (for $N_c = 3$) for the double gluon exchange consisting of a double color-traces. Hence the non-factorizable corrections are suppressed by a factor $O(1/N_c^2)$ with respect to the leading factorizable ones.

The second argument is based on the kinematical dependence of diagrams like those shown in Fig. 4.1. Such contributions, see e.g., Fig. 4.1 (right), come from the interference of diagrams with one or two gluons radiated by the upper quark line with diagrams where gluons are radiated by the lower line. As explained in Sec. 3.4, angular ordering in gluon emission leads to QCD radiation close to the quark from which it is emitted, and for the peculiar structure of VBF events, discussed in Sec. 3.3, the two final state quarks are usually well separated in phase-space. Therefore VBF kinematics itself should suppress this kind of interferences.
These arguments have already been used in [93] to justify neglecting real and virtual double gluon exchange diagrams in the computation of NLO QCD corrections for Higgs production in VBF with an extra jet.

The arguments given before can be enforced in a more quantitative way. If the total cross-section is expanded up to order α_s^2 as

$$\sigma_{NNLO} = \sigma_0 \left(1 + \alpha_s \Delta_1 + \alpha_s^2 \Delta_2\right), \tag{4.21}$$

the terms Δ_i show the impact on the LO cross section of the N^{i}LO corrections. While, as explained above, Δ_1 can be completely identified with the NLO factorizable corrections, in general Δ_2 receives contributions both from factorizable and non-factorizable corrections:

$$\Delta_2 = \Delta_2^{fact} + \Delta_2^{non-fact}. \tag{4.22}$$

The exact calculation of $\Delta_2^{non-fact}$ is out of reach, but the ratio of the NNLO non-factorizable contributions $\Delta_2^{non-fact}$, vs. the factorizable ones, Δ_2^{fact}, can be estimated as

$$R_2 \equiv \frac{\Delta_2^{non-fact}}{\Delta_2^{fact}} \simeq \frac{1}{N_c^2-1} R_1 \equiv \frac{1}{N_c^2-1} \frac{\Delta_1^{non-fact,\,U(1)}}{\Delta_1^{fact,\,U(1)}}, \tag{4.23}$$

where $\Delta_1^{fact,U(1)} = \Delta_1^{fact}/C_F$ and $\Delta_1^{non-fact,U(1)}$ denotes the “would-be” impact of the corrections coming from non-factorizable diagrams at NLO, *i.e.*, the class of diagrams involving the exchange of one gluon between the two quark lines, computed as if the color factor were non-vanishing.
In other words, $\Delta_1^{non-fact,U(1)}$ can be thought of as the correction due to the gauge invariant class of diagrams where an extra $U(1)$ massless gauge boson is exchanged between the two quark lines including real and virtual diagrams. The $R_2 \simeq R_1$ approximation assumes, of course, that the ratios will not dramatically change in going

from NLO to NNLO. As there is no substantial difference in the kinematics and no non-Abelian vertices enter at NNLO in diagrams where two gluons are exchanged in a color singlet in the t-channel, this assumption looks quite reasonable.

The four diagrams shown in Fig. 4.4, along with the corresponding real emissions, contribute to $\Delta_1^{non-fact}$. As the given argument only needs to provide an estimate of the corrections and it is based on the kinematics the calculation of the tensor integrals can be slightly simplified by considering only vector couplings of the vector boson to the quarks. This simplification eliminates all the rank-1 five-point functions in the computation, leaving only the scalar ones, which can be more easily reduced in terms of scalar four-point functions [94–96]. These scalar four-point functions, together with the four- and three-point functions coming from the Passarino-Veltmann reduction can be evaluated by means, e.g. of the QcdLoop package [97]. The results for the virtual contributions have been checked against the amplitude automatically generated by MadLoop [98], where machine precision agreement has been found point by point in the phase space.

The combination of the virtual and the real emission part, with the subtraction of the soft divergences (no collinear divergences occur in this class of diagrams), has been done via MadFKS [99] that automatically generates all the needed counterterms and performs the integration over phase space. In practice, the computation of the $O(\alpha_s)$ part of the cross section that enters in $\Delta_1^{non-fact}$, has been obtained as the difference of the complete NLO and the corresponding Born cross sections, and special attention has been paid to controlling the uncertainty of the numerical integration of the real emission contributions.

m_H [GeV]	σ_0 [pb]	$\Delta_1^{non-fact,U(1)}$	$\Delta_1^{fact,U(1)}$	R_1
100	$3.06\cdot10^{-5}$	$3.00(4)\cdot10^{-2}$	$8.79\cdot10^{-2}$	0.34
120	$2.09\cdot10^{-5}$	$2.90(5)\cdot10^{-2}$	$9.22\cdot10^{-2}$	0.31
150	$1.19\cdot10^{-5}$	$2.21(5)\cdot10^{-2}$	$9.91\cdot10^{-2}$	0.22
200	$4.87\cdot10^{-6}$	$-3.2(5)\cdot10^{-3}$	$1.12\cdot10^{-1}$	−0.03
250	$2.04\cdot10^{-6}$	$8(4)\cdot10^{-4}$	$1.25\cdot10^{-1}$	0.01
300	$8.68\cdot10^{-7}$	$2.7(4)\cdot10^{-3}$	$1.39\cdot10^{-1}$	0.02

Table 4.1: Non-diagonal NLO QCD corrections to VBF at the Tevatron, $\sqrt{S} = 1.96\,\text{TeV}$. Numbers have been computed ignoring the vanishing color factors of the diagrams in Fig. 4.4. The MRST2002 [100] NLO PDF set has been used. Renormalization and factorization scales have been set to M_W. Integration errors, if relevant, are shown in parenthesis.

In Tabs. 4.1–4.3 the results for the non-factorizable corrections $\Delta_1^{non-fact}$ are shown, for the Tevatron and for the LHC, compared with the quark-initiated factorizable ones,

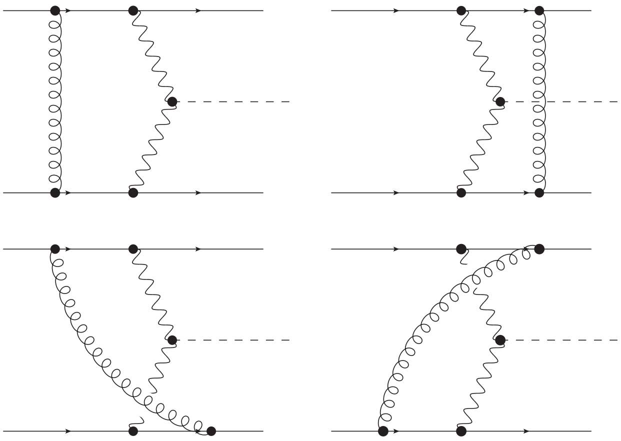

Figure 4.4: The four virtual topologies with one $U(1)$-gluon exchange between the quark lines, representing the virtual contribution to $\Delta_1^{non-fact}$.

m_H [GeV]	σ_0 [pb]	$\Delta_1^{non-fact,U(1)}$	$\Delta_1^{fact,U(1)}$	R_1
100	$2.04 \cdot 10^{-3}$	$6.6(3) \cdot 10^{-3}$	$1.57 \cdot 10^{-2}$	0.42
120	$1.74 \cdot 10^{-3}$	$5.4(4) \cdot 10^{-3}$	$1.54 \cdot 10^{-2}$	0.35
150	$1.39 \cdot 10^{-3}$	$3.4(2) \cdot 10^{-3}$	$1.53 \cdot 10^{-2}$	0.22
200	$9.84 \cdot 10^{-4}$	$-3.6(3) \cdot 10^{-3}$	$1.59 \cdot 10^{-2}$	−0.22
250	$7.12 \cdot 10^{-4}$	$-1.2(2) \cdot 10^{-3}$	$1.71 \cdot 10^{-2}$	−0.07
300	$5.26 \cdot 10^{-4}$	$-4(2) \cdot 10^{-4}$	$1.85 \cdot 10^{-2}$	−0.02
400	$3.00 \cdot 10^{-4}$	$2(2) \cdot 10^{-4}$	$2.24 \cdot 10^{-2}$	0.01
500	$1.78 \cdot 10^{-4}$	$1(2) \cdot 10^{-4}$	$2.69 \cdot 10^{-2}$	0.00
650	$8.66 \cdot 10^{-5}$	$5(2) \cdot 10^{-4}$	$3.45 \cdot 10^{-2}$	0.01
800	$4.41 \cdot 10^{-5}$	$2(2) \cdot 10^{-4}$	$4.28 \cdot 10^{-2}$	0.00
1000	$1.88 \cdot 10^{-5}$	$5(2) \cdot 10^{-4}$	$5.46 \cdot 10^{-2}$	0.01

Table 4.2: Non-diagonal NLO QCD corrections to VBF at the LHC, $\sqrt{S} = 7\,\text{TeV}$. Numbers have been computed ignoring the vanishing color factors of the diagrams in Fig. 4.4. The MRST2002 [100] NLO PDF set has been used. Renormalization and factorization scales have been set to M_W. Integration errors, if relevant, are shown in parenthesis.

Δ_1^{fact}. Both $\Delta_1^{non-fact}$ and Δ_1^{fact} are computed with the same color factor as the Born term.

The numbers shown are for the $ud \to udH$ channel with exchange of a Z-boson which couples vectorially to quarks.

m_H [GeV]	σ_0 [pb]	$\Delta_1^{non-fact,U(1)}$	$\Delta_1^{fact,U(1)}$	R_1
100	$5.63\cdot10^{-3}$	$4.0(4)\cdot10^{-3}$	$6.34\cdot10^{-3}$	0.63
120	$4.97\cdot10^{-3}$	$3.1(3)\cdot10^{-3}$	$5.76\cdot10^{-3}$	0.54
140	$4.42\cdot10^{-3}$	$2.8(3)\cdot10^{-3}$	$4.94\cdot10^{-3}$	0.56
150	$4.17\cdot10^{-3}$	$2.4(3)\cdot10^{-3}$	$4.62\cdot10^{-3}$	0.51
155	$4.06\cdot10^{-3}$	$1.7(3)\cdot10^{-3}$	$4.51\cdot10^{-3}$	0.37
160	$3.95\cdot10^{-3}$	$1.5(3)\cdot10^{-3}$	$4.39\cdot10^{-3}$	0.33
165	$3.84\cdot10^{-3}$	$8(2)\cdot10^{-4}$	$4.28\cdot10^{-3}$	0.18
170	$3.74\cdot10^{-3}$	$10(3)\cdot10^{-5}$	$4.20\cdot10^{-3}$	0.02
175	$3.64\cdot10^{-3}$	$-8(3)\cdot10^{-4}$	$4.08\cdot10^{-3}$	−0.21
180	$3.54\cdot10^{-3}$	$-1.3(2)\cdot10^{-3}$	$3.87\cdot10^{-3}$	−0.35
185	$3.45\cdot10^{-3}$	$-3.4(4)\cdot10^{-3}$	$3.86\cdot10^{-3}$	−0.89
190	$3.36\cdot10^{-3}$	$-2.8(3)\cdot10^{-3}$	$3.82\cdot10^{-3}$	−0.73
195	$3.27\cdot10^{-3}$	$-2.5(3)\cdot10^{-3}$	$3.74\cdot10^{-3}$	−0.67
200	$3.19\cdot10^{-3}$	$-2.6(2)\cdot10^{-3}$	$3.74\cdot10^{-3}$	−0.71
210	$3.03\cdot10^{-3}$	$-1.6(3)\cdot10^{-3}$	$3.62\cdot10^{-3}$	−0.43
230	$2.75\cdot10^{-3}$	$-7(5)\cdot10^{-4}$	$3.40\cdot10^{-3}$	−0.21
250	$2.50\cdot10^{-3}$	$-9(2)\cdot10^{-4}$	$3.32\cdot10^{-3}$	−0.26
300	$1.99\cdot10^{-3}$	$-5(2)\cdot10^{-4}$	$3.21\cdot10^{-3}$	−0.14
400	$1.32\cdot10^{-3}$	$2(2)\cdot10^{-4}$	$3.98\cdot10^{-3}$	0.05
500	$9.17\cdot10^{-4}$	$3(2)\cdot10^{-4}$	$5.32\cdot10^{-3}$	0.06
650	$5.59\cdot10^{-4}$	$6(2)\cdot10^{-4}$	$7.98\cdot10^{-3}$	0.07
800	$3.57\cdot10^{-4}$	$2(2)\cdot10^{-4}$	$1.11\cdot10^{-2}$	0.01
1000	$2.06\cdot10^{-4}$	$3(1)\cdot10^{-4}$	$1.63\cdot10^{-2}$	0.02

Table 4.3: Non-diagonal NLO QCD corrections to VBF at the LHC, $\sqrt{S} = 14\,\text{TeV}$. Numbers have been computed ignoring the vanishing color factors of the diagrams in Fig. 4.4. The MRST2002 [100] NLO PDF set has been used. Renormalization and factorization scales have been set to M_W. Integration errors, if relevant, are shown in parenthesis.

Looking at the numbers in Tabs. 4.1–4.3, an interesting fact can be pointed (not strictly related with the estimate of the non-factorizable corrections). $\Delta_1^{non-fact}$ displays a discontinuity, with sudden change of sign, at around $m_H = 180\,\text{GeV} = 2M_Z$, *i.e.*, the threshold of the $h \to ZZ$ process, which is due to the use of the zero-width approximation for the Z-bosons in the loop propagators, cf. also Refs. [101, 102]. A consistent inclusion of Z-boson width effects, which is beyond the scope of this analysis, would smoothen the discontinuity.

The results of Tabs. 4.1–4.3 show an R_1 always well below unity. Once the $O(1/N_c^2)$ color suppression in Eq. (4.23) is taken into account, one finds an upper bound on

$R_2 < 10\%$. As the impact of Δ_2^{fact} on the total cross-section is at the 1% level, the contribution of the non-factorizable corrections, omitted in the structure-function approach can be estimated to be at most at the per-mil level, hence completely negligible. Finally, it is interesting to note that $\Delta_1^{non-fact}$ decreases with increasing Higgs boson masses m_H, so that, as expected from the fact that the Higgs boson acts as a "kinematical de-correlator" between the two jets, the size of the non-factorizable corrections becomes totally negligible for $m_H > 300$ GeV.

4.2.1.3 Contributions from heavy-quark loops

Besides the non-factorizable corrections discussed above, the other class of diagrams which is not included in the structure function approach consists in diagrams in which the Higgs boson can couple to heavy quarks appearing in loops.
Following the definition of VBF given in Sec. 4.1 these contributions are classified in the strict sense as "non-VBF" processes. However these effects are genuinely new at NNLO and can be quite easily estimated or even exactly computed.

Three different classes of such contributions exist: the square-modulus of one-loop diagrams with no extra radiation requiring a quark-gluon initial state, Fig. 4.5; the interference of one-loop diagrams with an extra parton in the final state, Fig. 4.6, with the VBF real tree-level diagrams; finally the interference of two-loop diagrams, Fig. 4.7, with VBF diagrams at the Born level. Each of the three classes of loop diagrams has no soft/collinear divergences and is gauge invariant, thus can be treated independently.

Such contributions appear only for neutral weak currents. Moreover, in both boxes and triangles only the axial coupling of the Z-boson to the quarks survives, so that a mass-degenerate quark doublet gives zero contribution. Therefore only the top and bottom quarks need to be considered.

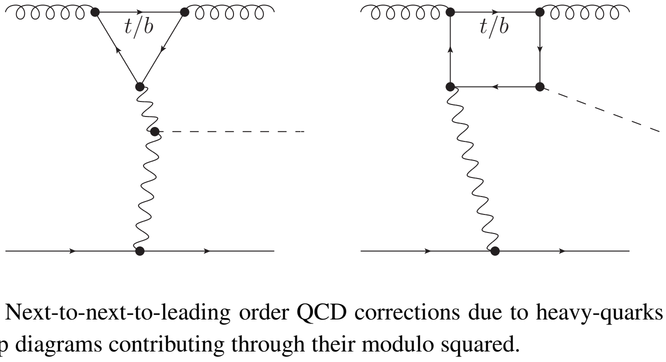

Figure 4.5: Next-to-next-to-leading order QCD corrections due to heavy-quarks (t/b) loops: pure one-loop diagrams contributing through their modulo squared.

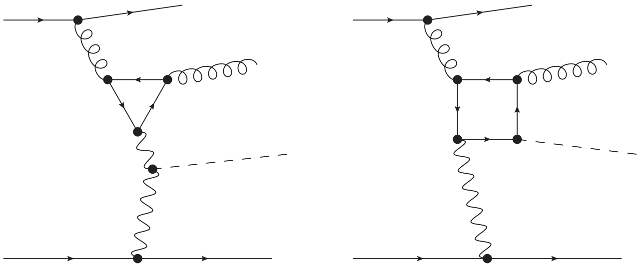

Figure 4.6: Next-to-next-to-leading order QCD corrections due to heavy-quarks (t/b) loops: one-loop plus extra parton diagrams interfering with VBF NLO real corrections.

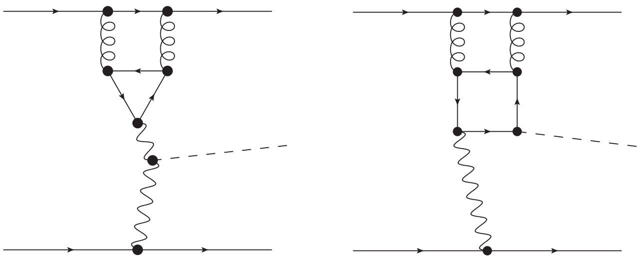

Figure 4.7: Next-to-next-to-leading order QCD corrections due to heavy-quarks (t/b) loops two-loop diagrams interfering with VBF LO diagrams.

4.2.1.3.1 Quark-gluon initiated contributions via the square of one-loop diagrams The first contribution to be considered is the one given by the diagrams shown in Fig. 4.5. A simple estimate [20] obtained in the limit $m_b \to 0$, $m_t \to \infty$, where only the contribution from the triangle is parametrically relevant, associates to this class an effect of less than one per-mil of the total cross section [25,27]. By itself this result is non-trivial given that the contributions of the diagrams in Fig. 4.5 are proportional to the quark-gluon parton luminosity, which is potentially large, especially at LHC. Thus, based on considering the triangle alone, it can be argued that contributions from the heavy-quark loops in Fig. 4.5 can be safely neglected.

It is interesting to investigate to which extent the conclusion above is confirmed by a complete calculation of these contributions. The corresponding one-loop diagrams are known since long time [103,104] (see also [59]), although in a different kinematic regime (*i.e.*, time-like) for the Z-boson. The contribution of these diagrams to Higgs boson production in VBF are shown in Fig. 4.8, where the sum of the triangle and the box, the triangle and the box alone and the limit $m_t \to \infty$ at $\sqrt{S} = 7\,\text{TeV}$ and $14\,\text{TeV}$ for the LHC and $\sqrt{S} = 1.96\,\text{TeV}$ for the Tevatron have been plotted. The pole mass values $m_b = 4.62\,\text{GeV}$, $m_t = 174.3\,\text{GeV}$ have been used. The numbers for the LHC

m_H [GeV]	$\sigma_{\rm LO}$	$\sigma_{\rm tri+box}$	$\sigma_{\rm tri}$	$\sigma_{\rm box}$	$\sigma^{\infty}_{\rm tri+box}$
100	1.49	$4.09\cdot10^{-4}$	$2.04\cdot10^{-4}$	$1.70\cdot10^{-4}$	$3.40\cdot10^{-4}$
120	1.22	$3.75\cdot10^{-4}$	$1.84\cdot10^{-4}$	$1.65\cdot10^{-4}$	$3.12\cdot10^{-4}$
150	$9.19\cdot10^{-1}$	$3.23\cdot10^{-4}$	$1.58\cdot10^{-4}$	$1.53\cdot10^{-4}$	$2.73\cdot10^{-4}$
200	$6.01\cdot10^{-1}$	$2.43\cdot10^{-4}$	$1.22\cdot10^{-4}$	$1.27\cdot10^{-4}$	$2.20\cdot10^{-4}$
250	$4.09\cdot10^{-1}$	$1.69\cdot10^{-4}$	$9.49\cdot10^{-5}$	$9.87\cdot10^{-5}$	$1.78\cdot10^{-4}$
300	$2.87\cdot10^{-1}$	$1.00\cdot10^{-4}$	$7.42\cdot10^{-5}$	$6.85\cdot10^{-5}$	$1.45\cdot10^{-4}$
400	$1.52\cdot10^{-1}$	$3.47\cdot10^{-5}$	$4.62\cdot10^{-5}$	$2.16\cdot10^{-5}$	$9.76\cdot10^{-5}$
500	$8.58\cdot10^{-2}$	$2.07\cdot10^{-5}$	$2.93\cdot10^{-5}$	$8.64\cdot10^{-6}$	$6.67\cdot10^{-5}$
650	$3.95\cdot10^{-2}$	$1.10\cdot10^{-5}$	$1.53\cdot10^{-5}$	$2.75\cdot10^{-6}$	$3.85\cdot10^{-5}$
800	$1.93\cdot10^{-2}$	$6.12\cdot10^{-6}$	$8.20\cdot10^{-6}$	$1.00\cdot10^{-6}$	$2.25\cdot10^{-5}$
1000	$8.00\cdot10^{-3}$	$2.89\cdot10^{-6}$	$3.71\cdot10^{-6}$	$2.97\cdot10^{-7}$	$1.12\cdot10^{-5}$

Table 4.4: Values of the contributions to the total NNLO VBF cross-section due to the heavy-quark loop diagrams shown in Fig. 4.5 at the LHC, $\sqrt{S} = 7\,\text{TeV}$. The MSTW2008 [71] NNLO PDF set has been used. The LO cross-section, computed with LO PDFs, is also shown for comparison. Renormalization and factorization scales have been set to M_W. Integration errors are below the 1% level. Cross-sections are in pb.

m_H [GeV]	$\sigma_{\rm LO}$	$\sigma_{\rm tri+box}$	$\sigma_{\rm tri}$	$\sigma_{\rm box}$	$\sigma^{\infty}_{\rm tri+box}$
100	5.08	$2.02\cdot10^{-3}$	$9.86\cdot10^{-4}$	$1.05\cdot10^{-3}$	$2.01\cdot10^{-3}$
120	4.29	$1.88\cdot10^{-3}$	$9.18\cdot10^{-4}$	$9.99\cdot10^{-4}$	$1.90\cdot10^{-3}$
150	3.40	$1.65\cdot10^{-3}$	$8.24\cdot10^{-4}$	$9.44\cdot10^{-4}$	$1.76\cdot10^{-3}$
200	2.40	$1.31\cdot10^{-3}$	$6.88\cdot10^{-4}$	$8.06\cdot10^{-4}$	$1.55\cdot10^{-3}$
250	1.76	$9.44\cdot10^{-4}$	$5.76\cdot10^{-4}$	$6.46\cdot10^{-4}$	$1.37\cdot10^{-3}$
300	1.33	$6.05\cdot10^{-4}$	$4.85\cdot10^{-4}$	$4.82\cdot10^{-4}$	$1.21\cdot10^{-3}$
400	$8.09\cdot10^{-1}$	$2.52\cdot10^{-4}$	$3.48\cdot10^{-4}$	$1.94\cdot10^{-4}$	$9.66\cdot10^{-4}$
500	$5.25\cdot10^{-1}$	$1.71\cdot10^{-4}$	$2.55\cdot10^{-4}$	$9.52\cdot10^{-5}$	$7.72\cdot10^{-4}$
650	$2.97\cdot10^{-1}$	$1.11\cdot10^{-4}$	$1.64\cdot10^{-4}$	$4.02\cdot10^{-5}$	$5.62\cdot10^{-4}$
800	$1.80\cdot10^{-1}$	$7.59\cdot10^{-5}$	$1.09\cdot10^{-4}$	$1.93\cdot10^{-5}$	$4.14\cdot10^{-4}$
1000	$9.82\cdot10^{-2}$	$4.76\cdot10^{-5}$	$6.53\cdot10^{-5}$	$8.05\cdot10^{-6}$	$2.79\cdot10^{-4}$

Table 4.5: Values of the contributions to the total NNLO VBF cross-section due to the heavy-quark loop diagrams shown in Fig. 4.5 at the LHC, $\sqrt{S} = 14\,\text{TeV}$. The MSTW2008 [71] NNLO PDF set has been used. The LO cross-section, computed with LO PDFs, is also shown for comparison. Renormalization and factorization scales have been set to M_W. Integration errors are below the 1% level. Cross-sections are in pb.

corresponding to the various scenarios in Fig. 4.8 are reported in Tabs. 4.4–4.5. From these numbers one can see that the limit $m_t \to \infty$, $m_b \to 0$ is a good estimate of the upper bound of the integrated cross section. In this case it has been verified that, as reported also in [103], the contribution of the box goes to zero.

Moreover, specially for large m_H, the triangle alone is also an upper bound, while for small m_H it approximates the total cross-section within a factor of 2.

The numbers shown have been obtained by two independent computations of the squared amplitude, and also agree point-by-point in phase space with the results of the code automatically generated by MadLoop [98]. The upshot is that the exact computation corroborates the findings of [20] that the impact of the diagrams in Fig. 4.5 on the VBF Higgs production cross section is always below the per-mil level of the Born contribution, and therefore can be safely neglected.

The exact result for the VBF cross section in the quark-gluon channel at NNLO allows for a comparison with the Higgs-Strahlung case. In this case a sizable destructive interference between the triangle and the box diagrams takes place [59, 104], while this does not happen for VBF (see also the plots in Fig. 4.8). It is instructive to find the origin of such a different behavior of the triangle and the box diagrams contributions in an s-channel process [104] compared to a t-channel one (cf. Fig. 4.8). To this aim it is useful to define the relative phase angle ϕ between the triangle and the box amplitudes $\mathcal{M}_{\text{tri}}$ and $\mathcal{M}_{\text{box}}$ by

$$|\mathcal{M}_{\text{tri}} + \mathcal{M}_{\text{box}}|^2 = |\mathcal{M}_{\text{tri}}|^2 + |\mathcal{M}_{\text{box}}|^2 + 2|\mathcal{M}_{\text{tri}}||\mathcal{M}_{\text{box}}|\cos\phi . \tag{4.24}$$

Recall that in the s-channel case in the large-m_t limit $\mathcal{M}_{\text{tri}}$ and $\mathcal{M}_{\text{box}}$ are real and opposite in sign thus implying $\phi \sim \pi$ [104]. This remains true for the crossed amplitudes in the t-channel case of Fig. 4.8 because, due to unitarity, the asymptotic behavior in the large-m_t limit remains the same. However, for finite top-quark masses away from large-m_t limit, both $\mathcal{M}_{\text{tri}}$ and $\mathcal{M}_{\text{box}}$ acquire an imaginary part above the threshold $\sqrt{S} \simeq 2m_t$ in the s-channel process. This is due to the gluon-gluon scattering process opening to real top-quark pair-production. Thus, $\mathcal{M}_{\text{tri}}$ and $\mathcal{M}_{\text{box}}$ become complex numbers pointing in almost opposite directions in the complex plane. and resulting in a strong destructive interference between them, see [104]. The different findings in the VBF case can now be easily understood: in the t-channel process of Fig. 4.5 only $\mathcal{M}_{\text{box}}$ can develop an imaginary part due to an intermediate real top-quark pair while $\mathcal{M}_{\text{tri}}$ remains real. As a net result $\mathcal{M}_{\text{tri}}$ and $\mathcal{M}_{\text{box}}$ are likely to be almost orthogonal in the complex plane thus suppressing the interference term in Eq. (4.24).

Finally, compared to the Higgs-Strahlung process, *i.e.*, the associated production of Higgs and a Z-boson in the gluon-fusion channel, the NNLO corrections in VBF from the heavy quarks are by far less important [59]. This difference has also a simple physical explanation, because in the Higgs-Strahlung this contribution proceeds through a

gg initiated s-channel, whereas VBF has the vector boson in the t-channel. The s-channel propagator enhances the small x-region where the gluon luminosity steeply rises. In the crossed case, *i.e.*, in VBF, the dominant contribution to the cross section comes from effective parton momentum fractions $\langle x \rangle \sim 0.05$, where the gluon luminosity is not large yet.

4.2.1.3.2 One-loop plus extra real parton diagrams

The next contributions to be studied are those coming from diagrams in Fig. 4.6 in the qq-channel and the crossed qg one. These diagrams feature one initial (final) state on-shell gluon attached to the heavy-quark loop, together with the Z-boson and a time-like (space-like) off-shell gluon. The overall contribution of this class of diagrams is estimated by computing only the triangles, yet keeping the m_t and m_b finite. This choice is justified by the fact that triangles are parametrically leading, in particular for large values of m_H and, as shown in Sec. 4.2.1.3.1, provide an approximate estimate for the total contribution, although reasonably close to the presumed true value. Furthermore the limit $m_t \to \infty$ can be computed, and (as shown in Sec. 4.2.1.3.1) is expected to behave as an upper upper bound for the cross-section. Indeed it is found to be quite close ($\simeq 20\%$) to the values computed for the triangle only. As for the contributions in the previous paragraph, the triangle diagrams as in Fig. 4.6 have already been computed before in other kinematic regimes (in the context of Z-boson decay into hadrons [105] or hadro-production [106]), but never with a space-like Z-boson.
As an additional simplification, consider only the parton channel with the extra gluon in the final state is considered, *i.e.*, the reaction $qq' \to qq'Hg$, the other parton channels having similar or smaller impact. This latter assumption is supported by the previous studies of Z-boson hadro-production [106], where it was shown that the entire class of diagrams in Fig. 4.6 is heavily suppressed with respect to the two-loop ones of Fig. 4.7 considered below in Sec. 4.2.1.3.3.

The necessary expressions for the interference of the one-loop diagrams with the tree-level ones have been computed analytically using MATHEMATICA and FEYNCALC [107] and have been put into MADGRAPH [108, 109] for the phase-space integration. The respective numbers for the contribution to the VBF total cross-section of the process $qq' \to Hqq'g$ due to the heavy-quark triangle in Fig. 4.6 at the LHC, at $\sqrt{S} = 7\,\text{TeV}$ and $14\,\text{TeV}$ are given in Tab. 4.6. Again, these contributions are totally negligible compared to the LO VBF cross-section, and also about one order of magnitude smaller than the ones studied in Sec. 4.2.1.3.1.

4.2.1.3.3 Two-loop diagrams

Finally, it is the turn of the two-loop contributions of Fig. 4.7 where the heavy-quark loop is attached via two gluons to the light-quark line originating from one of the protons. These diagrams interfere with the Born VBF

m_H [GeV]	σ_{LO}	$\sigma_{\mathrm{tri}}^{\mathrm{1loop+glu}}$
100	1.49	$5.10\cdot10^{-5}$
120	1.22	$4.02\cdot10^{-5}$
150	$9.19\cdot10^{-1}$	$2.89\cdot10^{-5}$
200	$6.01\cdot10^{-1}$	$1.74\cdot10^{-5}$
250	$4.09\cdot10^{-1}$	$1.11\cdot10^{-5}$
300	$2.87\cdot10^{-1}$	$7.41\cdot10^{-6}$
400	$1.52\cdot10^{-1}$	$3.53\cdot10^{-6}$
500	$8.58\cdot10^{-2}$	$1.84\cdot10^{-6}$
650	$3.95\cdot10^{-2}$	$7.72\cdot10^{-7}$
800	$1.93\cdot10^{-2}$	$3.52\cdot10^{-7}$
1000	$8.00\cdot10^{-3}$	$1.34\cdot10^{-7}$

m_H [GeV]	σ_{LO}	$\sigma_{\mathrm{tri}}^{\mathrm{1loop+glu}}$
100	5.08	$2.66\cdot10^{-4}$
120	4.29	$2.20\cdot10^{-4}$
150	3.40	$1.67\cdot10^{-4}$
200	2.40	$1.11\cdot10^{-4}$
250	1.76	$7.62\cdot10^{-5}$
300	1.33	$5.48\cdot10^{-5}$
400	$8.09\cdot10^{-1}$	$3.02\cdot10^{-5}$
500	$5.25\cdot10^{-1}$	$1.82\cdot10^{-5}$
650	$2.97\cdot10^{-1}$	$9.21\cdot10^{-6}$
800	$1.80\cdot10^{-1}$	$5.12\cdot10^{-6}$
1000	$9.82\cdot10^{-2}$	$2.54\cdot10^{-6}$

Table 4.6: Values of the contributions to the total NNLO VBF cross-section due to the heavy-quark triangle plus gluon emission diagrams shown in Fig. 4.6 at the LHC, at $\sqrt{S} = 7\,\mathrm{TeV}$ (left) and $\sqrt{S} = 14\,\mathrm{TeV}$ (right). The MSTW2008 [71] NNLO PDF set has been used. The LO cross-section, computed with LO PDFs, is also shown for comparison. Renormalization and factorization scales have been set to M_W. Integration errors are below the 1% level. Cross-sections are in pb.

amplitudes. The effective coupling to the light-quark line singles out the iso-triplet component of the proton in the squared matrix elements, since only the axial part of the Z-boson coupling contributes for non-degenerate heavy-quarks in the loop. That is to say, this class of diagrams is proportional to the (non-singlet) distribution $\delta q_{\mathrm{ns}}^{-}$ of Eq. (4.19), which is generally small.

In analogy to the previous Sec. 4.2.1.3.2, the aim is to have an estimate of the size of the contributions of Fig. 4.7 rather than their exact impact. Therefore, one can restrict to the two-loop triangle diagrams, also given the fact that the two-loop double box in Fig. 4.7 is currently unknown for the required VBF kinematic configuration and its computation would be a tremendous task in itself.

The two-loop triangles for the $q\bar{q}Z$ vertex have been computed in [105] for the case $m_b = 0$ and $m_t \neq 0$, see also [106]. Rather compact results in terms of harmonic polylogarithms [91] (see [92] for numerical routines) for all kinematic configurations have been obtained in [110] and the latter expressions have been used to compute the numbers shown in Tab. 4.7 for the LHC at $\sqrt{S} = 7\,\mathrm{TeV}$ and $14\,\mathrm{TeV}$. Again, a comparison of the cross section numbers in Tab. 4.7 for the reaction $qq' \to Hqq'$ at NNLO in QCD mediated by the two-loop triangle with the LO cross-section shows that such contributions are below the per-mil level.

In ending this discussion of heavy-quark loop contributions I briefly remark that, of course, the diagrams shown in Figs. 4.5–4.7, also contribute in heavy-quark DIS, if the full neutral-current reactions are considered, *i.e.*, both γ and Z-boson exchange at high Q^2. Currently available DIS data on heavy-quark production, however, is usually taken at Q^2 values where these contributions are not relevant. Their existence is an issue, though, to be recalled in the definition of variable-flavor number schemes, see e.g., [111].

m_H [GeV]	σ_{LO}	$\sigma_{\text{tri}}^{\text{2loop}}$
100	1.49	$8.38 \cdot 10^{-4}$
120	1.22	$7.08 \cdot 10^{-4}$
150	$9.19 \cdot 10^{-1}$	$5.60 \cdot 10^{-4}$
200	$6.01 \cdot 10^{-1}$	$3.90 \cdot 10^{-4}$
250	$4.09 \cdot 10^{-1}$	$2.81 \cdot 10^{-4}$
300	$2.87 \cdot 10^{-1}$	$2.06 \cdot 10^{-4}$
400	$1.52 \cdot 10^{-1}$	$1.18 \cdot 10^{-4}$
500	$8.58 \cdot 10^{-2}$	$7.08 \cdot 10^{-5}$
650	$3.95 \cdot 10^{-2}$	$3.52 \cdot 10^{-5}$
800	$1.93 \cdot 10^{-2}$	$1.84 \cdot 10^{-5}$
1000	$8.00 \cdot 10^{-3}$	$8.18 \cdot 10^{-6}$

m_H [GeV]	σ_{LO}	$\sigma_{\text{tri}}^{\text{2loop}}$
100	5.08	$2.30 \cdot 10^{-3}$
120	4.29	$2.01 \cdot 10^{-3}$
150	3.40	$1.67 \cdot 10^{-3}$
200	2.40	$1.25 \cdot 10^{-3}$
250	1.76	$9.63 \cdot 10^{-4}$
300	1.33	$7.60 \cdot 10^{-4}$
400	$8.09 \cdot 10^{-1}$	$4.99 \cdot 10^{-4}$
500	$5.25 \cdot 10^{-1}$	$3.44 \cdot 10^{-4}$
650	$2.97 \cdot 10^{-1}$	$2.10 \cdot 10^{-4}$
800	$1.80 \cdot 10^{-1}$	$1.35 \cdot 10^{-4}$
1000	$9.82 \cdot 10^{-2}$	$7.91 \cdot 10^{-5}$

Table 4.7: Values of the contributions to the total NNLO VBF cross-section due to the two-loop trinagle diagram shown in Fig. 4.7 at the LHC, at $\sqrt{S} = 7\,\text{TeV}$ (left) and $\sqrt{S} = 14\,\text{TeV}$ (right). The MSTW2008 [71] NNLO PDF set has been used.The LO cross-section, computed with LO PDFs, is also shown for comparison. Renormalization and factorization scales have been set to M_W. Integration errors are below the 1% level. Cross-sections are in pb.

4.2.2 One-loop electroweak corrections

I will now briefly discuss the one loop electroweak corrections to VBF, and explain how they can be combined with the (NNLO) QCD ones. The detailed computation of such corrections can be found in [55, 56] and is beyond the scope of this thesis.

In [55, 56] the NLO EW and NLO QCD corrections have been computed and have been implemented in the public computer code HAWK [112]. The full computation of the $O(\alpha_s^2 \alpha_{EW}) \times$ Born corrections being impossible, one has to establish a safe way to combine NNLO QCD corrections and NLO EW ones.

If one calls

$$\sigma_{NNLO}^{QCD} = \sigma_0 + \alpha_s \sigma_1^{QCD} + \alpha_s^2 \sigma_2^{QCD} \tag{4.25}$$

the total cross-section up to NNLO in QCD and

$$\sigma_{NLO}^{EW} = \sigma_0 + \alpha_{EW}\sigma_1^{EW} \tag{4.26}$$

the total cross-section up to NLO EW, the combined NNLO QCD and NLO EW total cross-section can be defined as

$$\sigma_{NNLO+EW} = \sigma_{NLO}^{EW} + \alpha_s\sigma_1^{QCD} + \alpha_s^2\sigma_2^{QCD} = \sigma_{NNLO}^{QCD} + \alpha_{EW}\sigma_1^{EW}. \tag{4.27}$$

This combination, which is exact and does not include any spurious term in the calculation, is called the “additive” scheme.
However, to be completely consistent, this scheme implies that all terms are computed with exactly the same parameters (EW parameters, PDF, scale choices,. . .) and settings, request that can be difficult (or at least error-prone) to be fulfilled when different codes are used.

An alternative approach to the combination is the so-called “multiplicative” scheme. This approach is mainly driven by the hypothesis that EW and QCD corrections factorize to a very good approximation at NLO and NNLO. In this scheme the combined cross-section is defined as

$$\sigma_{NNLO+EW} = \sigma_{NNLO}^{QCD}\left(1 + \frac{\alpha_{EW}\sigma_1^{EW}}{\sigma_0}\right). \tag{4.28}$$

With respect to the additive scheme, the multiplicative one is more practical: since most of the PDF/scale dependence cancels in the ratio $\frac{\alpha_{EW}\sigma_1^{EW}}{\sigma_0}$, it loosens the constraint of having the same parameters in the two codes, at the cost of introducing spurious terms of order $\alpha_{EW}\alpha_s$ and $\alpha_{EW}\alpha_s^2$. Anyway, as far as the total cross-section is concerned, an excellent agreement is found between the two schemes and, as the multiplicative one is the most practical, it will be used in the following.

4.2.3 Off-shell effects

The last class of corrections I want to discuss is the one that involves effects due to the fact that the Higgs boson is an unstable particle.
Consider the production of a particle P by an initial state I decaying to a final state X: the roughest way to compute the cross-section of this process is simply to multiply

the cross-section for the production of $I \to P$ and the branching-ratio for the decay $P \to X$. This is the so-called zero-width approximation (ZWA):

$$\sigma^{ZWA}_{I\to P\to X} = \sigma_{I\to P}(m_P)\,\mathrm{Br}_{P\to X}, \tag{4.29}$$

where $\sigma_{I\to P}(m_P)$ is the production cross-section computed with P on shell.
As said, this is the roughest way, and neglects effects due to the virtuality of P[2]. These effects affect both the decay and the production cross-section, however they are of order Γ_P/m_P, so they are quite small for a narrow particle. If this approximation may be correct for a light Higgs ($m_H < 300\,\mathrm{GeV}$), it completely breaks down for a heavy one, as in this case the width becomes comparable to its mass.

The expression for the total cross-section which includes these effects is

$$\sigma^{OFF}_{I\to P\to X} = \int dQ^2 \frac{Q\Gamma(Q)}{\pi} \sigma_{I\to P}(Q)\left(\left(Q^2 - m_P^2\right)^2 + m_P^2\Gamma_P(m_P)^2\right)^{-1} \mathrm{Br}_{P\to X}(Q), \tag{4.30}$$

which, since

$$\lim_{\Gamma_P\to 0}\left(\left(Q^2 - m_P^2\right)^2 + m_P^2\Gamma_P(m_P)^2\right)^{-1} = \frac{\pi}{m_p\Gamma_P(m_p)}\delta Q^2 - m_P^2, \tag{4.31}$$

reduces to the ZWA if the width is small enough. The interesting fact about σ^{OFF} is that the expression Eq. (4.30) is equivalent to computing the cross-section for the production of the final state X retaining only the diagrams with P in the s-channel.
However, as soon as P goes off-shell, gauge invariance can be broken. Indeed, gauge invariance is guaranteed only for the full process $I \to X$. While usually at LO gauge invariance is kept, it can be a serious problem when higher order corrections are taken into account. In order to preserve gauge invariance for QCD, extra radiation should be included both in the production and in the decay, including all possible interferences. However, for colorless resonances, interferences between production and decay arising from QCD corrections usually vanish because of color conservation, so in the end gauge invariance is not an issue in the case of QCD corrections. Conversely, for EW corrections, this is not a priori true. In addition, the appearance of the width in the denominator can spoil cancellations due to relations between parameters which are usually crucial to ensure gauge invariance.

---

[2] The factorization into production and decay is not correct in quantum-mechanics. This is because it neglects interferences between different polarization states of P. However, since the topic of this thesis is the scalar Higgs boson, quantum mechanics effects due to interferences of different helicity states will play no role in this case and will not be mentioned in the text.

To this aim, the so-called complex-mass scheme (CMS) [113, 114] has been developed: gauge invariance is ensured by promoting masses as complex quantities, defined as the location of the poles in the complex p^2 plane, where p is the momentum flowing in the propagator. These complex masses need to be introduced everywhere in the Feynman rules, for example in the weak mixing angle

$$\cos^2\theta_w = \frac{s_W^2}{s_Z^2}\,, \tag{4.32}$$

which is derived from the ratio of the complex masses of the gauge vectors,

$$s_V^2 = m_V^2 - \mathrm{i} m_V \Gamma_V\,. \tag{4.33}$$

In the case of the Higgs boson, the CMS needs to be further dug [115]: if the Higgs propagator Δ_H is written as

$$\frac{1}{\Delta_H(s)} = s - m_H^2 + S_{HH}(s, m_H, m_X)\,, \tag{4.34}$$

in terms of the renormalized mass m_H and self energy S_{HH} (m_X symbolically represents the masses of any other particle ($W, Z, t, \ldots$), its complex pole s_H is defined as the complex solution of the equation

$$s_H - m_H^2 + S_{HH}(s_H, m_H, m_X) = 0\,. \tag{4.35}$$

Indeed, in the CMS, all the masses appearing as argument of the self-energy S_{HH} have to be replaced by the corresponding complex poles.

The peculiarity of the Higgs boson, with respect to other particles (e.g. the vector bosons), can be understood by considering its branching ratios: even for a light Higgs, below the WW threshold, the branching ratio into four fermions is comparable with that in a pair of b quarks. In terms of the Higgs boson self-energy, this means that cuts from 1-loop diagrams and from 3-loop diagrams are equally important.

Therefore the extraction from the Higgs boson lineshape of the on-shell mass and width is not as simple as it would be in the case of the W (or Z) boson, where the predominant decay mode is into two massless fermions. In the case of the W, on-shell quantities are simply related to the real and imaginary part of the complex pole. If it is parameterized as

$$s_W^2 = \mu_W^2 - \mathrm{i}\mu_W \gamma_W\,, \tag{4.36}$$

then one has

$$\mu_W^2 = m_{W\,OS}^2 - \Gamma_{W\,OS}^2 + \dots , \qquad \gamma_W = \Gamma_{W\,OS}\left(1 - \frac{1}{2}\frac{\Gamma_{W\,OS}^2}{m_{W\,OS}^2}\right) + \dots , \tag{4.37}$$

where the ellipses denote higher order contributions.
In the case of the Higgs boson, due to the non-perturbativity of its self-energy, the expansion is more complicated [115], and on-shell quantities are ill-defined. This can be understood from the definition of the on-shell width (or analogously from that of the on-shell mass)

$$\Gamma_H^{OS}\, m_H^{OS} = \mathrm{Im} S_{HH,\,OS} + \dots , \tag{4.38}$$

and from the fact that the bosonic part of the Higgs boson self-energy is gauge-parameter dependent at lowest order. This is possible since in a gauge theory only the complex pole of the propagator is gauge independent.

The preferred way to include off-shell effects for the Higgs boson is to write its propagator as

$$\frac{1}{\Delta_H(s)} = s - s_H , \tag{4.39}$$

with

$$s_H = \mu_H^2 - \mathrm{i}\gamma_H\mu_H , \tag{4.40}$$

where μ_H is treated as an independent parameter (set equal to the Higgs mass) and γ_H is obtained from the relation

$$\mu_H\gamma_H = \mathrm{Im} S_{HH}(s_H, S_X) , \tag{4.41}$$

where s_X replaces the corresponding mass in all parameters, and fixing the renormalization scale to μ_H.

To solve Eq. (4.41), the HTO code [116] is used.

4.3 Results for the $\sqrt{S} = 8\,\mathrm{TeV}$ LHC

In this chapter I will present the results for the total cross-section of VBF. In particular, I will focus on results computed for a center-of-mass energy $\sqrt{S} = 8\,\mathrm{TeV}$, corresponding to the LHC run during 2012. Results for $\sqrt{S} = 7, 14\,\mathrm{TeV}$ can be found in [21,23]. Ref. [21] also contains results for the $\sqrt{S} = 1.96\,\mathrm{TeV}$ run at the Tevatron.
The values for the SM parameters used in the computation are those recommended by the Higgs Cross-Section Working Group (HXSWG) [35]:

$$\begin{aligned} M_W &= 80.398\,\mathrm{GeV}, & \Gamma_W &= 2.089\,\mathrm{GeV}, \\ M_Z &= 91.188\,\mathrm{GeV}, & \Gamma_Z &= 2.496\,\mathrm{GeV}, \\ G_F &= 1.166\times 10^{-5}\,\mathrm{GeV}^{-2} & . \end{aligned} \tag{4.42}$$

In the first plot, shown in Fig. 4.3.1, I present results including only QCD corrections, up to NNLO. This helps in understanding the behaviour of the perturbative series, and how much such behaviour is affected by the choice of renormalization and factorization scale. Three choice of reference scales are presented, each one with the corresponding theoretical uncertainty band obtained by varying independently the renormalization and factorization scales around the reference scale μ_{REF}:

$$\mu_R = x_R\, \mu_{REF}\,, \qquad \mu_F = x_F\, \mu_{REF}\,. \tag{4.43}$$

Since there is not any special prescription about the variation range of the scale factors $x_{R,F}$, I have considered two possible ranges, one smaller, used by the HXSWG [23,24]

$$1/2 < x_{R,F} < 2\,, \tag{4.44}$$

and one larger, corresponding to a more conservative uncertainty estimate

$$1/4 < x_{R,F} < 4\,. \tag{4.45}$$

In the DIS-inspired structure function approach, the most natural scale choice is to set the scales equal to Q, the virtuality of the vector boson attached to each proton. This scale choice corresponds to the curves in the upper frame of Fig. 4.3.1, and to the ratios in the first inset. From this inset, one can appreciate the very good convergence of the perturbative series: the effect of NLO corrections is to increase the total rate of 6% in the whole scanned mass range; NNLO corrections have a very tiny effect on the total rate, but their inclusion lead in a stabilization of the theoretical uncertainties at the $\pm 2 - 3\%$ level if scales variations of up to a factor 4 are considered. Almost no change in the NNLO cross-section is observed when scales are varied by a factor of 2, witnessing for an almost flat scale dependence.

This scale choice, which, as said, looks the most natural in the approach that I presented for the computation, however is not suitable for being implemented in fully differential codes: as soon as an extra radiated particle is explicitly considered, it makes impossible to define unambiguously "the virtuality of the vector boson attached to each proton" in terms of the momenta of the external particles. Furthermore, in view of the inclusion of the EW corrections obtained from HAWK, as this code does not allow to choose a variable reference scale, a fixed scale has to be used.

Two possible fixed scales looks most natural: the Higgs mass, or the mass of the vector bosons. The second choice, although non related to any of the external particle, is the one that most reproduces the Q choice. This can be understood from the fact that, because of the t-channel propagators, the largest part of the contribution to the cross-section comes from virtualities smaller than or of the order of the mass of the vector-boson in the propagator. The behaviour of the total VBF cross-section with this scale choice ($\mu_{REF} = M_W$) is shown in the second inset of Fig. 4.3.1, where it is compared with the NNLO prediction obtained choosing Q as reference scale. As can be observed by comparing the first two insets, the behaviour of the perturbative series, as well as the residual theoretical uncertainties are similar in the two cases, and complete agreement is found between the two NNLO predictions. The third inset shows results with the Higgs mass as reference scale, which shows a worse behaviour of the perturbative series at large Higgs masses (where also large uncertainties still affect the NNLO computation), confirming the fact that VBF is mostly governed by low scales.

I now turn to discuss results which include EW corrections and off-shell effects, computed in the complex-pole scheme. These results, which have also been published in [24], represent the best available prediction for the total cross-section of VBF. They are shown in Fig. 4.3.2. In this figure, the main frame shows three curves: the red curve is the NNLO prediction already shown before. The green curve includes Higgs off-shell effects on top of the NNLO QCD corrections, and the blue curve also incorporates electroweak corrections as computed with HAWK. The lower inset shows the same curves normalized to the NNLO prediction, together with the contribution from EW corrections alone (in orange, not shown in the main frame).

All predictions have been computed using the NNLO MSTW 08 PDF set, fixing renormalization and factorization scale to M_W. The low mass range ($100 < M_H < 300$) of the lower inset is expanded in Fig. 4.3.3.

The impact of EW corrections can be sizable, depending on the mass range considered. For a light Higgs boson, below the VV thresholds, EW corrections are negative and fairly constant (-4%). When the WW and ZZ thresholds are crossed, their impact slightly softens, but starts to slowly grow again (in magnitude) until the $t\bar{t}$ threshold is reached. From the $t\bar{t}$ threshold the behaviour changes, as EW corrections start a trend that will eventually bring them positive after $M_H = 500\,\text{GeV}$, with an almost-linear growth up to the end of the explored mass-range (1 TeV), where their impact reaches the 25% of the total cross-section.

Turning to the impact of off-shell corrections, their effect is positive in the entire mass range, and generally grows with the Higgs boson mass. As expected, for large masses, off-shell effects are quite important (15%). It is however surprising to see visible effects also at low masses, below the VV thresholds. For a 125 GeV Higgs, even if the narrow width approximation is supposed to be correct, being the width of the Higgs boson almost five order of magnitudes smaller than the Higgs boson mass ($\Gamma(M_H = 125\,\text{GeV}) = 4.07\,\text{MeV}$), off-shell effects are already visible, accounting for a $1-2\%$ correction on the total rate. This has been understood and explained in details (for the gluon-fusion production channel) in [117]. When the Higgs boson propagator is incorporated in the computation, to account for off-shell effects, it enters with the Higgs boson width, sampled at the Higgs boson virtuality Q, in the numerator (check Eq. (4.30)). Therefore off-shell effects are sampled proportionally to $\Gamma(Q^2)/\left|M_H^2 - s_H\right|^2$. While normally the denominator damps contributions away from the pole, if the width grows fast enough with the virtuality, as it does for the Higgs boson, this is not the case any longer. This explains why one has visible effects due to the Higgs boson off-shellness even in a region where, naively, the narrow-width approximation is expected to be accurate.

Scale uncertainties are not significantly affected by the inclusion of off-shell effects.

I conclude this chapter discussing the residual theoretical uncertainties on the total cross-section. I have already discussed the uncertainties estimated by varying the renormalization and factorization scales, which are at the $2-3\%$ level in the whole mass range. The impact of these variations can be used to estimate the size of the next terms in the perturbative series.

The other source of theoretical uncertainties is related to the choice of parton distribution functions (PDFs). As PDFs are a non-perturbative ingredient of the computation and have to be extracted by previous data, the way they are determined can bias, or at least affect the prediction. All the main PDF collaborations have delivered sets including NNLO QCD evolution, which can be used to obtain consistent NNLO predictions. Results with the most recent NNLO sets are shown in Fig. 4.3.4. These sets are HERAPDF 1.5 [118, 119], ABM 11 [120], JR 09 [121, 122], MSTW 08 [71], NNPDF 2.1 [123] and CT 10 [124]. From the plot one can appreciate the fact that all central sets lie in a band not wider than 5% of the total cross-section for almost all the mass range, while the width of the error bands envelope ranges from 7% at low masses to 15% at large masses.

4.4 Conclusion

In this chapter I have presented the state-of-art predictions for the VBF total cross-section. A large part of this chapter has been spent in studying NNLO QCD corrections to the total cross-section. After having classified the possible contributions, I have shown that the numerically dominant part comes from contributions that can be computed in the structure-function approach.
Since in this approach QCD corrections are completely separated from the weak boson which fuse into the Higgs, it can be generalized to the production of new fermiophobic scalar and vectorial resonances, both neutral or charged. The interested reader can find some benchmark result in [21, 26]. The formulae corresponding to Eq. (4.5) for the case of a scalar resonance with anomalous coupling to vector bosons or for a vector resonance can be found in App. B.

I continued the chapter presenting results for the $\sqrt{S} = 8\,\text{TeV}$ LHC: NLO corrections, even if rather small, are important in order to get the correct total rate, while the main effect of the inclusion of the NNLO is the reduction of the renormalization and factorization scale dependence at the $2-3\%$ level, in the whole range of the Higgs boson mass.
The computation of the total cross-section has been improved by including NLO EW corrections and off-shell effects. The former are computed using the public, third-party code HAWK, while the latter have been obtained by including the Higgs boson propagator in the complex-pole scheme in the computation. These non-QCD corrections are mandatory in order to claim an accuracy on the total rate at the level of few percents, and their inclusion make the VBF total cross-section being possibly the most precisely known LHC cross-section.

To conclude, I want to stress that the validity of the structure function approach at NNLO, together with modern NNLO subtraction techniques [125], pave the way to the fully differential (parton level) computation of VBF. This would be a spectacular result, as no $2 \to 3$ hadronic process is known at NNLO yet.

The code used to compute NNLO corrections in the structure function approach can be run on-line from the web-interface [126].

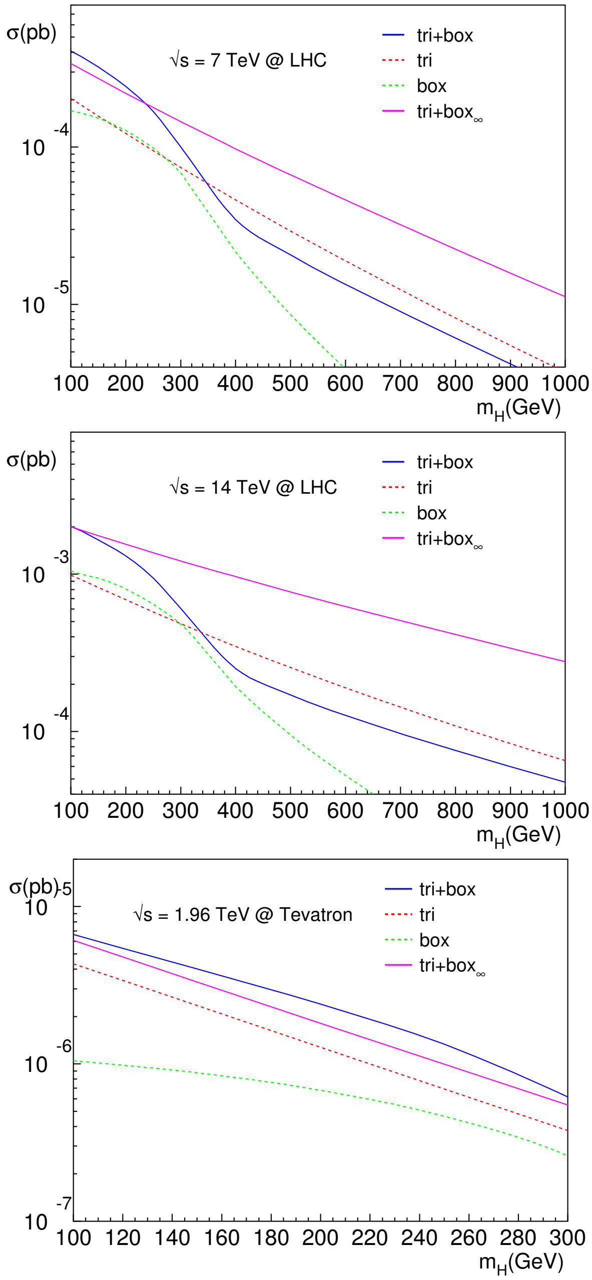

Figure 4.8: Contribution of the heavy-quarks (t/b) loops to the total NNLO VBF cross section, at the LHC with $\sqrt{S} = 7\,\text{TeV}$ (top-left), $\sqrt{S} = 14\,\text{TeV}$ (top-right) and at the Tevatron, $\sqrt{S} = 1.96\,\text{TeV}$. Numbers are computed with the MSTW 2008 [71] NNLO PDF set. The renormalization and factorization scales have been set to M_W.

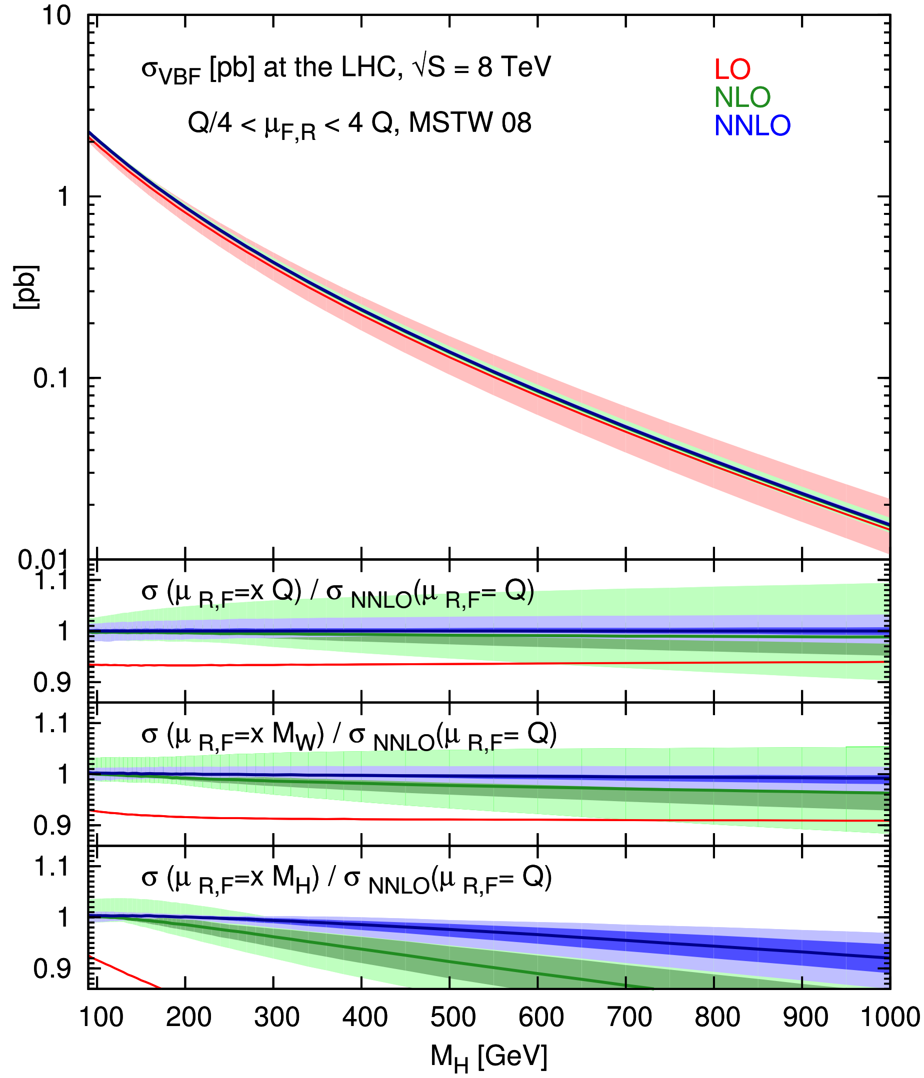

Figure 4.3.1: Total cross-section predictions for VBF at the LHC, $\sqrt{S} = 8\,\mathrm{TeV}$, at LO (red), NLO (green) and NNLO (blue) in QCD. Bands correspond to the independent variations of renormalization and factorization scales around the reference value in the range $\mu_{REF}/4 < \mu_{R,F} < 4\mu_{REF}$. The main frame shows prediction obtained setting $\mu_{REF} = Q$ where Q is the virtuality of the vector boson. The first inset shows the curves in the main frame rescaled to the NNLO prediction. The second and third insets show respectively predictions obtained with $\mu_{REF} = M_W$ and $\mu_{REF} = M_H$, rescaled to the NNLO curve obtained with $\mu_{REF} = Q$. In the insets, the darker (lighter) bands (LO bands are not shown) correspond to scale variations in the range $\mu_{REF}/4 < \mu_{R,F} < 4\mu_{REF}$ ($\mu_{REF}/2 < \mu_{R,F} < 2\mu_{REF}$). The LO, NLO and NNLO MSTW 2008 pdf sets [71] have been used (consistently with the order of the cross-section).

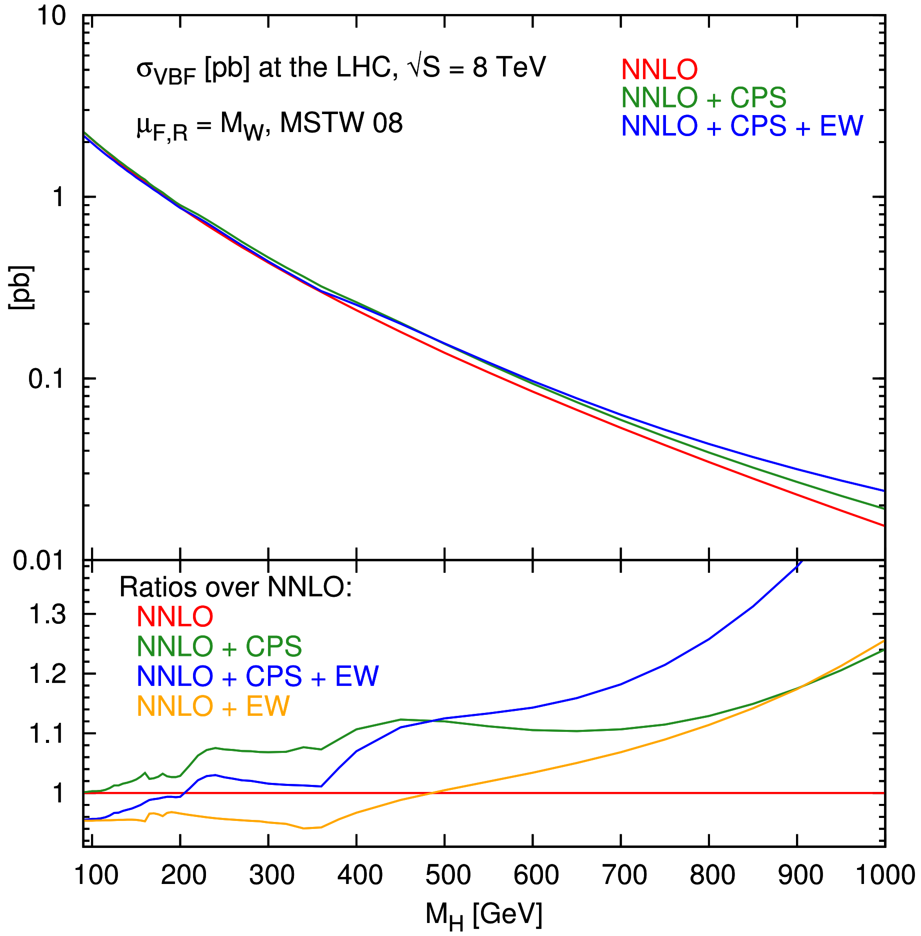

Figure 4.3.2: Impact of off-shell effects and EW corrections on the total cross-section for VBF at the LHC, $\sqrt{S} = 8\,\text{TeV}$. The curves in the main frame represent the total rate at NNLO in QCD (red), on top of which off-shell effects have been added in the complex pole scheme (CPS), with (blue) or without (green) electroweak corrections. The lower inset shows the ratio of the curves in the main frame over the NNLO prediction (with the same color pattern). The orange curve (absent in the main frame) shows the impact of EW corrections alone, without off-shell effects. Numbers have been computed with the NNLO MSTW 08 PDF set [71], setting renormalization and factorization scales to M_W.

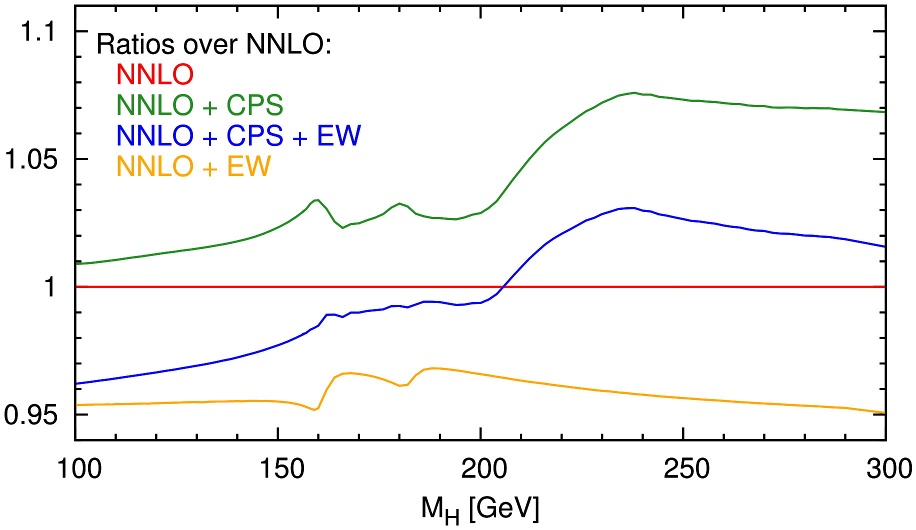

Figure 4.3.3: Impact of off-shell effects and EW corrections on the total cross-section for VBF at the LHC, $\sqrt{S} = 8\,\text{TeV}$, in the low-mass range. Curves are rescaled to the NNLO prediction (in red), and represent off-shell effects with (blue) or without (green) electroweak corrections, and electro-weak corrections alone (orange). Numbers have been computed with the NNLO MSTW 08 PDF set [71], setting renormalization and factorization scales to M_W.

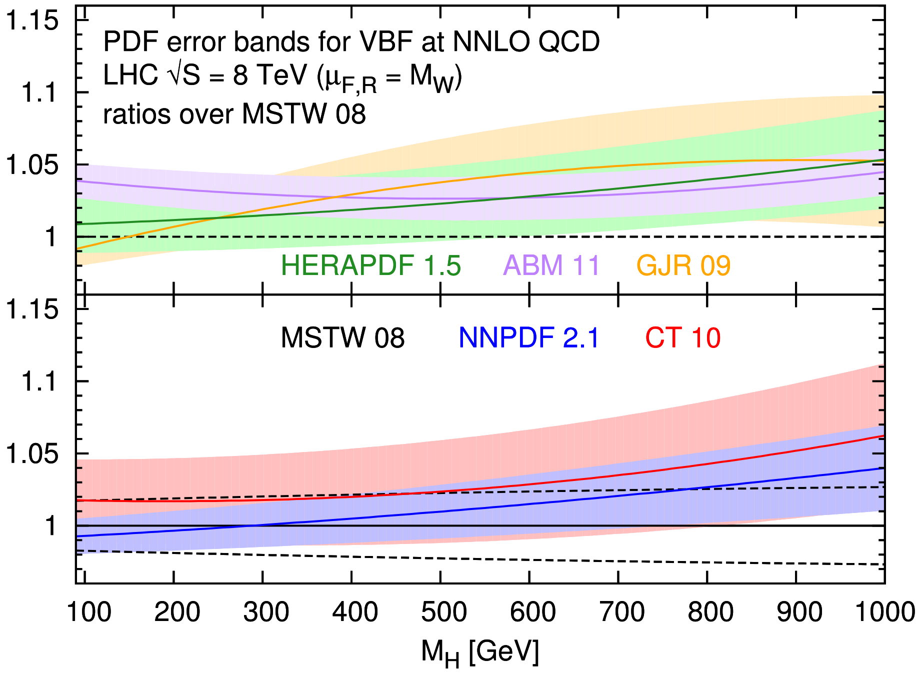

Figure 4.3.4: Comparison between NNLO predictions for the total VBF cross-section obtained with different PDF sets, shown as ratios over MSTW 2008 [71]. The upper plot shows results obtained with the HERAPDF 1.5 [118,119], ABM 11 [120] and JR 09 [121,122] sets. The lower plot shows results obtained with MSTW 08 [71] (68% CL), NNPDF 2.1 [123] and CT 10 [124]. Bands (or dashed lines for MSTW 08) correspond to the estimate of PDF uncertainties. The NNLO set delivered by each collaboration has been used. Scales are fixed to M_W.

Chapter 5

Simulating VBF at hadron colliders

The results presented in this chapter are based on [22] and on the VBF chapter of [24].

5.1 Introduction

In the previous chapter I discussed how to obtain very precise predictions for the total VBF cross-section. However, an accurate knowledge of the total cross-section is not useful if a comparable accuracy is not achieved also on differential observables: first of all, because the total cross-section is never directly measured at experiments: what is actually measured is the cross-section within some given cuts, either dictated by the finite acceptance of the detector (so-called acceptance cuts) or imposed to better distinguish the signal over the background (the selection cuts). On top of the cross-section, usually some specific observables are measured, like the transverse momentum of a jet or the invariant mass of two particles. Higher order corrections need to be included also in the prediction of these observables.
Furthermore, the distance between the few partons taking part to the theoretical description and the large number of hadrons that usually populate events at hadron colliders has to be reduced in order to achieve a higher degree of realism. This is done by passing the parton-level events to a parton shower Monte Carlo (PSMC), which will add extra QCD radiation to the events and cluster the partons into hadrons.

The two aspects, of including higher order corrections in fully differential programs, and of using such programs to generate events which are suitable for being showered, need to be carefully put together. On one hand, one has to cancel the IR singularities that typically affect the ingredients (real-emission and virtual matrix-elements) of a NLO computation in a way which is suitable for being integrated numerically (in 4 dimensions). Process-independent approaches have been developed to this aim, such as the dipole [127, 128], FKS [129, 130] and antenna [131, 132] subtraction schemes. On the other hand, matching a NLO prediction with PSMCs requires some care, in order not to double count configurations generated by the shower and by the real-emission matrix-element. Two methods to match predictions at NLO QCD with parton showers have been developed: POWHEG [133, 134] and MC@NLO [135].

This chapter will be structured as follows: the first part Sec. 5.2 will be devoted to introduce the FKS subtraction scheme, which is employed both in POWHEG and MC@NLO. I will continue introducing how a PSMC works in Sec. 5.3, and presenting, in Sec. 5.4, issues related with matching NLO computations to parton showers and the basics of the MC@NLO and POWHEG methods. Finally in Sec. 5.5 I will present results for VBF at the LHC.

5.2 The FKS subtraction scheme

The computation of a NLO cross-section is built from two main ingredients: the contribution coming from the interference of loop and born diagrams, $\mathcal{V}$, known as virtual matrix-element and the contribution $\mathcal{R}$ coming from the real radiation of an extra massless particle:

$$d\sigma_{NLO} = d\Phi_n \left(\mathcal{B} + \mathcal{V} + d\Phi_1 \mathcal{R}\right) , \tag{5.1}$$

with n the number of final-state particles. These two contributions, the real-emission and the virtual matrix element, are in general separately non-finite, while their sum is finite, according to the Kinoshita-Lee-Nauenberg (KLN) theorem [136, 137]. In brief, this theorem relies on the fact that, in the singular limit when the extra particle accounted for in the real-emission matrix-element becomes soft and/or collinear to any other particle, the final state configuration cannot be distinguished from the configuration without radiation. This configuration is considered, at the same order in the coupling constant, by the virtual matrix-element.

Typically, when one uses dimensional regularization to control these singularities, divergences manifest as poles in the dimensional regularization parameter ε, when the loop momentum or the extra particle in the real-emission matrix-element is integrated:

$$\mathcal{V} = -\frac{C_2}{\epsilon^2} - \frac{C_1}{\epsilon} + \mathcal{V}_{fin} , \tag{5.2}$$

$$\int d\Phi_1 \mathcal{R} \quad = \quad \frac{C_2}{\epsilon^2} + \frac{C_1}{\epsilon} + \mathcal{R}_{fin}\,. \tag{5.3}$$

The analytic integration of the extra particle phase-space becomes impossible, or at least very difficult, as soon as the number of final-state particles starts to grow. On top of this, an exclusive description of the final state requests to explicitly consider also effects which are due to the radiation of an extra particle.

In order to perform a numerical integration, finite (four dimensionsional) n and $n+1$ body contributions are needed, which will be integrated independently. To achieve this one has to subtract the divergent part from the real-emission matrix-element before performing the integration, by introducing suitable counterterms C such that (in four dimensions) the integral

$$\int d\Phi_1 \left(\mathcal{R} - C\right) \tag{5.4}$$

converges. This implies

$$\int d\Phi_1 C = \frac{C_2}{\epsilon^2} + \frac{C_1}{\epsilon} + C_{fin}\,. \tag{5.5}$$

Typically C is not zero only close to the singular limit, where "close" is specified by some cuts on energy and angles (it will become more clear in the following). This makes it possible to choose C such that the integral in Eq. (5.5) can be done analytically, such that the NLO cross-section can be written as

$$\begin{aligned} d\sigma_{NLO} \quad &= \quad d\Phi_n \left(\mathcal{B} + \mathcal{V} + \int d\Phi_1 C + d\Phi_1 \left(\mathcal{R} - C\right)\right) = \\ &= \quad d\Phi_n \left(\mathcal{B} + \mathcal{V}_{fin} + C_{fin} + d\Phi_1 \left(\mathcal{R} - C\right)\right) = \\ &= \quad d\Phi_n \left(\mathcal{B} + \mathcal{V}_{fin} + C_{fin}\right) + d\Phi_{n+1} \left(\mathcal{R} - C\right). \end{aligned} \tag{5.6}$$

In the last line of Eq. (5.6) the n- and $n+1$-body integrals are separately finite. The choice of a specific structure for the counterterms C and the prescription to practically obtain the NLO cross-section is called the "subtraction scheme". I will now turn to explain the choice originally presented in [129] by Frixione, Kunszt and Signer, referring to it as to the FKS subtraction.

5.2.1 Notation

In this section I will briefly introduce the notation that I will use in presenting the FKS subtraction. I will focus on the case of a hadronic scattering process, but all definitions can be simply adapted to the case of leptonic or lepto-hadronic initial states, as well as of a decay. As done previously, I will assume the born and real-emission kinematics to correspond respectively to n and $n+1$ final-state particles. Focusing to the case of QCD corrections, I will call n_0 the number of non-strongly interacting particles, n_H, and n_L respectively the number of massive and massless strongly interacting particles. Born and real configuration can differ only by one unit of n_L. Therefore:

$$\begin{aligned} n_L^R &= n_L^B + 1\,, && (5.7)\\ n &= n_L^B + n_H + n_0\,, && (5.8)\\ n+1 &= n_L^R + n_H + n_0\,. && (5.9) \end{aligned}$$

A partonic subprocess P is defined by a list of particle identities $\mathcal{I}_k$ with the convention of putting first initial-state particles, then strongly interacting particles (first massless, then massive ones), finally non strongly interacting particles:

$$P = (\mathcal{I}_1, \mathcal{I}_2, \underbrace{\mathcal{I}_3, \ldots, \mathcal{I}_{2+n_L}}_{n_L}, \underbrace{\mathcal{I}_{2+n_L+1}, \ldots, \mathcal{I}_{2+n_L+n_H}}_{n_H}, \underbrace{\mathcal{I}_{2+n_L+n_H+1}, \ldots, \mathcal{I}_{2+n_L+n_H+n_0}}_{n_0})\,. \tag{5.10}$$

The sets of n and $n+1$-body subprocesses will be denoted as $\mathcal{P}_n$ and $\mathcal{P}_{n+1}$.
A given n-body subprocess can always be related to at least one $n+1$-body subprocess, and vice-versa[1]. If i and j are two strongly interacting particles, with i massless and in the final state ($3 < i < 2+n_L$, $1 < j < 2+n_L+n_H$) one can define, starting from a process $P \in \mathcal{P}_{n+1}$, the processes $P^{\backslash\!\!\!i}$, $P^{j\oplus i,\backslash\!\!\!i}$ (when they exist). $P^{\backslash\!\!\!i}$ is simply obtained removing i from the list of particles, $P^{j\oplus i,\backslash\!\!\!i}$ removing both i and j, and replacing j with the parton which enters the $(\mathcal{I}_i, \mathcal{I}_j, \mathcal{I}_{i\oplus j})$ QCD vertex. Even if in some cases $P^{\backslash\!\!\!i}$ and $P^{j\oplus i,\backslash\!\!\!i}$ may coincide, the use of two different notations is justified by the fact that they are associated to different singularities of the real-emission process P.
The processes $P^{\backslash\!\!\!i}$, $P^{j\oplus i,\backslash\!\!\!i}$ are called the underlying born processes of P.

5.2.2 Ingredients

I will now list the amplitudes that are needed in order to have a full computation of a NLO cross-section. Once this amplitudes are provided, they can be put together using the formulae in Sec. 5.2.3.
The amplitudes needed for a full NLO computation are born amplitudes $A_{\mathcal{B}}(P)$, the

---

[1] This is not strictly true as in some peculiar cases some real-emission subprocesses are not related to any born process because they are finite, e.g. the real subprocess $q\bar{q} \to Hg$ does not reduce to the born subprocess $gg \to H$.

virtual (loop) amplitudes $A_{\mathcal{V}}(P)$ and the real emission amplitudes $A_{\mathcal{R}}(P)$. For the first two classes $P \in \mathcal{P}_n$, while for the last class $P \in \mathcal{P}_{n+1}$. From now on, I will assume it is understood which class of processes P belongs to.

From these amplitudes the terms entering the short-distance cross-sections are computed, which are defined as

$$\begin{aligned}
\mathcal{B}(P) &= \frac{1}{2s}\overline{\sum_{CH}}|A_{\mathcal{B}}(P)|^2 \,, && (5.11)\\
\mathcal{B}_{kl}(P) &= \frac{1}{2s}\overline{\sum_{CH}}A_{\mathcal{B}}(P)\; Q(\mathcal{I}_k)\cdot Q(\mathcal{I}_l)\; A_{\mathcal{B}}(P)^* \,, && (5.12)\\
\mathcal{V}(P) &= \frac{1}{2s}\overline{\sum_{CH}}2\mathrm{Re}\left(A_{\mathcal{B}}(P)A_{\mathcal{V}}(P)^*\right) , && (5.13)\\
\mathcal{R}(P) &= \frac{1}{2s}\overline{\sum_{CH}}|A_{\mathcal{R}}(P)|^2 \,. && (5.14)
\end{aligned}$$

In all expressions explicitly sum (average) over color and helicities of final (initial) state particles, and include the flux factor (s is the partonic center-of-mass energy defined as $s = 2k_1 \cdot k_2$).
It can be instructive to spend some words about $\mathcal{B}_{kl}$, the so-called "color-linked borns". These matrix-elements correspond to the born amplitude $\mathcal{B}$ with color-factors corresponding to the exchange of an extra gluon between external legs k and l, and will enter the counterterms for soft singularities. The color-operators $Q(\mathcal{I})$ which enter the definition depend on the nature of k and l.

One practical way to generate the color-linked born is the following:

- Consider the born amplitude $A_{\mathcal{B}}$, with colors of the external particles fixed, as a sum of Feynman diagrams, which are written as a product of a Lorentz part D_i and a color-algebra part $C_i^{a_1,\dots,a_{n_C}}$

  $$A_{\mathcal{B}}^{a_1,\dots,a_{n_C}} = \sum_i C_i^{a_1,\dots,a_{n_C}} D_i \,, \qquad (5.15)$$

  where $n_C = 2 + n_H + n_L$ is the number of colored particles.
  The color-algebra part typically corresponds to an expression involving generators of the color group $SU(3)$ in different representations (*i.e.* t^a and f^{abc}), and carries indexes for each colored external particle.

- The inclusion of the color structure corresponding to the exchange of a gluon between two legs will only affect C_i. In particular, one has to compute the interference between $A_{\mathcal{B}}^{a_1,\dots,a_{n_C}}$ and the modified (color-linked) amplitude $A_{\mathcal{B}}^{a_1,\dots,a_{n_C};\,kl}$ which accounts, in its color-algebra, for the exchange of a gluon between legs k and l[2]. The new color coefficients will be written as

  $$C_i^{a_1,\dots,\,a_{n_C};\,kl} = C_i^{a_1,\,\dots,\,a_k\to a_{k_0},\,a_l\to a_{l_0},\,\dots,\,a_{n_C}}\, Q(\mathcal{I}_k)^{a_{k_0},a_g,a_k}\, Q(\mathcal{I}_l)^{a_{l_0},a_g,a_l}\,, \tag{5.16}$$

  where a_{k_0}, a_{l_0} are dummy indexes and

  $$\begin{aligned} Q(\mathcal{I} = q)^{a,b,c} &= -t^b_{ca}\,, & (5.17)\\ Q(\mathcal{I} = \bar{q})^{a,b,c} &= t^b_{ac}\,, & (5.18)\\ Q(\mathcal{I} = g)^{a,b,c} &= \mathrm{i} f^{abc}\,, & (5.19) \end{aligned}$$

  (the definition can be trivially extended in the case of new representations of the color group).

- Once the color-linked amplitude is available, the color linked borns can be simply obtained as

  $$\mathcal{B}_{kl}(P) = \frac{1}{2s}\overline{\sum_{CH}} 2\mathrm{Re}\left(A_{\mathcal{B}}(P) A^{kl}_{\mathcal{B}}(P)^*\right)\,, \tag{5.20}$$

  where the color-indexes of the external particles are understood.

The final formulae of the FKS subtraction method, which will be given in Sec. 5.2.3, will only involve non-divergent quantities. The explicit proof of the cancellation of soft and collinear singularities that arise in the intermediate steps of the computation is given in the original FKS paper [129].

In a generic computation, the finiteness of the partonic cross-section is usually a consequence of having imposed kinematic cuts on final state particles. In general, these cuts will be equivalent to ask to have either n_L^B or $n_L^B + 1$ jets in the final state, to be reconstructed with an arbitrary algorithm. This condition, together with other possible kinematic cuts, is understood to be included in all matrix-elements in Eqs. (5.11)–(5.14), in the sense that if the condition is not fulfilled the matrix element is zero. With such a definition, $\mathcal{B}$, $\mathcal{B}_{kl}$ and $\mathcal{V}$ are guaranteed to be finite, whereas $\mathcal{R}$ will still diverge in the soft and collinear limit. These divergences are subtracted by means of

---

[2] Strictly speaking one would have to compute the interference between the amplitude which accounts for the radiation of a gluon from leg k and the amplitude which account for the radiation from leg l. However, the two approaches are completely equivalent, and the one presented here has the advantage of re-using the color-informations of the born.

the counterterms.
In order to classify these divergences, for any given real-emission process $P \in \mathcal{P}_{n+1}$ the following set of pairs (called FKS pairs) is introduced:

$$\begin{aligned}\mathbf{P}_{FKS}(P) \quad = \quad & \{(i,j) : 3 \leq i \leq n_L + n_H + 2,\ j \leq n_L + n_H + 2,\ i \neq j, \\ & \mathcal{R}(P) \to \infty \text{ if } k_i \cdot k_j \to 0\Big\}\,. \qquad (5.21)\end{aligned}$$

In words, a pair of particles belongs to the FKS pairs if these particles can generate soft or collinear singularities in the real-emission matrix element. The first element, i, is called the FKS parton, and has to be a final state particle, while the second, j, is called its sister. $\mathbf{P}_{FKS}(P)$ takes into account all the singularities of the real-emission matrix-element which can arise after having imposed kinematic cuts; each of such pairs will correspond to a set of soft and/or collinear counterterms, which, once combined with the real-emission matrix-element, will result in a finite contribution to physical observables. Each of these finite contributions can be computed independently from the others, and integrated with numerical methods.

Using a naive point of view, the number of FKS pairs seems to grow as $(n_L + n_H)^2$. However, it is clear that, in order to have a singularity, at least one of the two particles has to be massless, reducing the scaling to $n_L(n_L + n_H)$. This massless particle will be identified, without loss of generality, with the FKS parton. On the other hand, depending on the identities of the particles in the given process, some of the contributions due to the FKS pairs will be identical, because of symmetry properties of the matrix-element and of the phase-space. This implies a drastic reduction of the number of independently terms actually needed in the computation. As an example, for the process $q\bar{q} \to ng$, only three independent contributions $\{(g,q),\ (g,\bar{q}),\ (g,g)\}$ survive.

5.2.3 Computing the cross-section

The cross-section at NLO for a generic process involving hadrons $1,2$ in the initial state, with momenta K_1, K_2 is

$$\begin{aligned} d\sigma_{12}(K_1,K_2) = & \sum_{P_\mathcal{B} \in \mathcal{P}_n} \int dx_1 dx_2 f^1_{I_1}(x_1) f^2_{I_2}(x_2) d\sigma^n(P_\mathcal{B}, k_1, k_2) \\ & + \sum_{P_\mathcal{R} \in \mathcal{P}_{n+1}} \int dx_1 dx_2 f^1_{I_1}(x_1) f^2_{I_2}(x_2) \Big(d\sigma^{n+1}(P_\mathcal{R}, k_1, k_2) + d\bar{\sigma}^{n+1}(P_\mathcal{R}, k_1, k_2)\Big)\,, \quad (5.22)\end{aligned}$$

with

$$k_i = x_i K_i\,. \qquad (5.23)$$

The short-distance cross-sections $d\sigma^n$, $d\sigma^{n+1}$ and $d\bar{\sigma}^{n+1}$ have respectively an n-body, $(n+1)$-body and degenerate $(n+1)$-body kinematics. The degenerate $(n+1)$-body contribution comes from the remainders of the subtraction of initial-state singularities, which are not canceled by the virtual matrix-elements, but by a redefinition of the parton densities. Each of them is separately finite.
I turn to discuss these three contributions in the next three subsections.
In the discussion, I will assume renormalization and factorization scales fixed to the same value $\mu_R = \mu_F = \mu$.

5.2.3.1 $(n+1)$-body contributions

The short distance cross-sections $d\sigma^{n+1}$ in Eq. (5.22) are due to contributions of the real-emission matrix-elements $\mathcal{R}$ with their phase-space singularities suitably subtracted. The integration of the subtracted matrix-elements is the most involved from the numerical point of view, and the difficulty increases with the number of external legs, because of the proliferation of singularities. In the FKS formalism, this problem is simplified by partitioning the phase-space in such a way that, in each of the regions resulting from the partition, at most one soft and one collinear singularity are present. This partition is achieved by introducing a set of positive-definite functions

$$\mathcal{S}_{ij}(P), \qquad (i,j) \in \mathbf{P}_{FKS}(P), \tag{5.24}$$

which obey the constraint

$$\sum_{(i,j)\in\mathbf{P}_{FKS}(P)} \mathcal{S}_{ij}(P) = 1\,. \tag{5.25}$$

Each of this function must go to zero in all singular regions of the phase-space, except for the region which corresponds to parton i being soft or collinear to j.

Using Eq. (5.25) one can write

$$\mathcal{R}(P) = \sum_{(i,j)\in\mathbf{P}_{FKS}(P)} \mathcal{S}_{ij}(P)\mathcal{R}(P)\,, \tag{5.26}$$

where, thanks to the conditions imposed on the $\mathcal{S}$-functions, each of the terms appearing in the sum in the right-hand side will only be singular when i is soft or collinear to j. Therefore, each term can be regarded as describing a production process with the simplest possible divergence structure. Furthermore, these contributions are fully independent from each other.

I turn now to provide the expression for the subtracted real-emission cross-section. To this aim, I work in the center-of-mass of the two incoming partons

$$k_1 = \frac{\sqrt{s}}{2}(1,0,0,1), \qquad k_2 = \frac{\sqrt{s}}{2}(1,0,0,-1), \tag{5.27}$$

and define in this frame, for each FKS pair, the variables ξ_i and y_{ij} as

$$E_i = \frac{\sqrt{s}}{2}\xi_i\,, \tag{5.28}$$

$$\vec{k}_i \cdot \vec{k}_j = \left|\vec{k}_i\right|\left|\vec{k}_j\right| y_{ij}\,. \tag{5.29}$$

The interpretation of ξ_i and y_{ij} is apparent from their definition: ξ_i is the rescaled energy of the FKS parton, and y_{ij} is the cosine of the angle between the FKS parton and its sister. The soft and collinear singularity will correspond respectively to the limits $\xi_i \to 0$ and to $y_{ij} \to 1$. In these limits, the real-emission matrix-element will diverge as

$$\mathcal{R} \sim \frac{1}{\xi_i}, \quad \text{if}\ \xi_i \to 0\,, \qquad \mathcal{R} \sim \frac{1}{1-y_{ij}}, \quad \text{if}\ y_{ij} \to 1\,. \tag{5.30}$$

The (finite) $(n+1)$-body contributions in Eq. (5.22) can be written as

$$d\sigma^{n+1}(P) = \sum_{(i,j)\in \mathbf{P}_{FKS}(P)} d\sigma_{ij}^{n+1}(P)\,, \tag{5.31}$$

where

$$d\sigma_{ij}^{n+1}(P) = \left(\frac{1}{\xi_i}\right)_c \left(\frac{1}{1-y_{ij}}\right)_\delta \Big((1-y_{ij})\xi_i^2\mathcal{R}(P)\Big) S_{ij}(P)\frac{d\Phi_{n+1}}{\xi_i}\,. \tag{5.32}$$

The $(n+1)$ body phase-space can be written in terms of ξ_i and y_{ij} (and an azimuthal angle ϕ_i) as

$$d\Phi_{n+1} = \xi_i d\xi_i\, dy_{ij}\, d\varphi_i\, d\tilde{\Phi}_n^{ij}\,. \tag{5.33}$$

In Eq. (5.32) the singularities of the real-emission matrix-element have been regularized by the plus-prescriptions defined as

$$\int_0^{\xi_{max}} d\xi_i f(\xi_i)\left(\frac{1}{\xi_i}\right)_c \;=\; \int_0^{\xi_{max}} d\xi_i \frac{f(\xi_i) - f(0)\Theta(\xi_{cut}-\xi_i)}{\xi_i}\,, \tag{5.34}$$

$$\int_{-1}^{1} dy_{ij} g(y_{ij})\left(\frac{1}{1-y_{ij}}\right)_\delta \;=\; \int_{-1}^{1} dy_{ij} \frac{g(y)_{ij} - g(1)\Theta(\delta - 1 + y_{ij})}{1-y_{ij}}\,. \tag{5.35}$$

These plus-prescriptions will define the counterterms, as I will show in the following. The parameters δ and ξ_{cut} define the boundaries of the singular region, *i.e.*the region in which counterterms are subtracted from the real-emission matrix-element. The physical cross-section Eq. (5.22), as well as any infrared-safe observable will be strictly independent on these parameters.

I will now turn to expand the plus-prescriptions in Eq. (5.32) using the definitions in Eqs. (5.34) and (5.35). First, I rewrite Eq. (5.32) in a more compact form as

$$d\sigma_{ij}^{n+1} = \left(\frac{1}{\xi_i}\right)_c \left(\frac{1}{1-y_{ij}}\right)_\delta \Sigma_{ij}\left(\xi_i, y_{ij}\right) d\xi_i dy_{ij}. \tag{5.36}$$

Then, expanding the plus-prescriptions, I obtain

$$\begin{aligned} d\sigma_{ij}^{n+1} \quad = \quad & \int_0^{\xi_{max}} d\xi_i \int_{-1}^{1} dy_{ij} \frac{1}{\xi_i(1-y_{ij})} \Big[\Sigma_{ij}(\xi_i, y_{ij}) - \Sigma_{ij}(\xi_i, 1)\Theta(\delta - 1 + y_{ij}) - \\ & \Sigma_{ij}(0, y_{ij})\Theta(\xi_{cut} - \xi_i) + \Sigma_{ij}(0,1)\Theta(\delta - 1 + y_{ij})\Theta(\xi_{cut} - \xi_i)\Big]. \end{aligned} \tag{5.37}$$

After having expanded the plus-prescriptions, four terms have appeared. They are called the “event” ($\Sigma_{ij}(\xi_i, y_{ij})$), the “collinear counterevent” ($\Sigma_{ij}(\xi_i, 0)$), the “soft counterevent” ($\Sigma_{ij}(0, y_{ij})$) and the “soft-collinear counterevent“ ($\Sigma_{ij}(0,0)$). If the matrix-element has no collinear singularity (e.g. because j is massive), the corresponding counterterms will vanish because of the damping factor $(1 - y_{ij})$ included in their definition. Similarly in the case of no soft singularity.

I will conclude this subsection by giving the explicit form of the counterterms in term of the matrix-elements introduced in Sec. 5.2.2. The major ingredient in all counterterms is the damped real-emission matrix-element

$$\mathcal{R}_{ij} = (1 - y_{ij})\xi_i^2 \mathcal{R}. \tag{5.38}$$

In particular, the damping factors need to be canceled out analytically in order to ensure the numerical stability of the computation. If $\{k\}$ are the momenta for the real-emission process P and $\{\bar{k}\}$ the corresponding (born-like) momenta for the born process $P^{\setminus i}$, the soft limit of the damped matrix-element is

$$\lim_{\xi_i \to 0} \mathcal{R}_{ij}(P, \{k\}) = g_s^2 \sum_{p=1}^{n_L^{\mathcal{B}} + n_H + 2} \sum_{l=p}^{n_L^{\mathcal{B}} + n_H + 2} \left. \frac{(1 - y_{ij})\xi_i^2 \, \bar{k}_p \cdot \bar{k}_l}{\bar{k}_p \cdot k_i \, \bar{k}_l \cdot k_i} \right|_{\xi_i = 0} \mathcal{B}_{pl}\left(P^{\setminus i}, \{\bar{k}\}\right), \tag{5.39}$$

if i is a gluon, otherwise it simply vanishes.
The eikonal factors which appear in Eq. (5.39) are finite at $\xi_i = 0$, since the factor ξ_i^2 in

the numerator cancels with the factor resulting from E_i^2 in the scalar product appearing in the denominator. Furthermore Eq. (5.39) is also finite in the soft-collinear limit (relevant if $m_j = 0$), because of the cancellation of the factor $1 - y_{ij}$ in the numerator with the corresponding factor appearing in the denominator when $p = j$ or $l = j$. These cancellations can be carried out analytically, assuring a stable behaviour of the soft counterevent in the whole phase-space.

Turning to the collinear limit, relevant if $m_i = m_j = 0$ one obtains

$$\begin{aligned}\lim_{y_{ij}\to 1} \mathcal{R}_{ij}(P,\{k\}) \quad &= \quad g_s^2 \left. \frac{(1-y_{ij})\xi_i^2}{k_i \cdot k_j} \right|_{y_{ij}=1} \\ &\times \left[P^0_{\mathcal{I}_j \mathcal{I}_{i\oplus j}}(z_{ji}) \mathcal{B}\left(P^{i\oplus j,\setminus i}, \{\bar{k}\}\right) + Q^0_{\mathcal{I}_j \mathcal{I}_{i\oplus j}}(z_{ji}) \widetilde{\mathcal{B}}\left(P^{i\oplus j,\setminus i}, \{\bar{k}\}\right)\right].\end{aligned} \tag{5.40}$$

In Eq. (5.40) P^0_{ba} is the Altarelli-Parisi splitting function [138], $\widetilde{\mathcal{B}}$ is the spin-connected born, which accounts for the interferences of different polarization states of particle $\mathcal{I}_i \oplus \mathcal{I}_j$ and Q is the spin-correlated Altarelli-Parisi splitting kernel. The spin-correlated part vanishes after the integration over φ_i. However, pointwise in the phase-space it is non-zero and has to be included in order to have a proper local counterterm. Finally z_{ji} is the energy fraction carried by particle j

$$z_{ji} = \frac{E_j}{E_i + E_j}. \tag{5.41}$$

Again, the factor $1 - y_{ij}$ appearing in Eq. (5.40) cancels with the corresponding factor appearing in the denominator $k_i \cdot k_j$, leading to a well-behaved expression in the whole phase-space.

5.2.3.2 Degenerate $(n+1)$-body contributions

I turn now to the degenerate $(n+1)$-body contributions, denoted with $d\bar{\sigma}^{n+1}$ in Eq. (5.22). As said, these contributions are the remainders left by the subtraction of initial-state collinear counterterms. In the case I am considering, the one of a hadronic collider, two contributions have to be included, one per hadron:

$$d\bar{\sigma}^{n+1}(P) = \sum_{(i,1)\in \mathbf{P}_{FKS}} d\bar{\sigma}^{n+1}_{i1}(P) + \sum_{(i,2)\in \mathbf{P}_{FKS}} d\bar{\sigma}^{n+1}_{i2}(P). \tag{5.42}$$

The explicit form of $d\bar{\sigma}^{n+1}_{ij}$, which has been derived in [129], is

$$d\bar{\sigma}^{n+1}_{i1}(P; k_1, k_2) \;=\; \frac{\alpha_s}{2\pi} \times$$

$$\times\left\{\overline{P}^{0}_{\mathcal{I}_{1\oplus\bar{i}}\mathcal{I}_1}(1-\xi_i)\left[\left(\frac{1}{\xi_i}\right)_c\log\frac{s\delta}{2\mu^2}+2\left(\frac{\log\xi_i}{\xi_i}\right)_c\right]-\overline{P}^{1}_{\mathcal{I}_{1\oplus\bar{i}}\mathcal{I}_1}(1-\xi_i)\left(\frac{1}{\xi_i}\right)_c\right\}$$
$$\times\mathcal{B}\left(P^{1\oplus\bar{i},\bar{\not{i}}};(1-\xi_i)k_1,k_2\right)d\Phi_n\,(1-\xi_i k_1,k_2)\,d\xi_i\,. \tag{5.43}$$

The expression for $d\bar{\sigma}^{n+1}_{i2}$ can be trivially derived from Eq. (5.43) by replacing 1 → 2. The only care is that the born matrix-element and the phase space have now to be computed with initial-state momenta $(k_1,(1-\xi_i)k_2)$. Eq. (5.43) is valid if the PDFs are given in the $\overline{\text{MS}}$ scheme, which is the standard choice for all modern sets. The damped Altarelli-Parisi splitting-function $\overline{P}_{ab}$ appear in the expressions, defined as

$$\overline{P}_{ab}(z,\epsilon)=(1-z)P_{ab}(z,\epsilon)=\overline{P}^{0}_{ab}(z,\epsilon)+\epsilon\overline{P}^{1}_{ab}(z,\epsilon)+\ldots\,. \tag{5.44}$$

I also have introduced the distribution (defined in analogy with Eq. (5.34))

$$\int_0^{\xi_{max}} d\xi_i f(\xi_i)\left(\frac{\log\xi_i}{\xi_i}\right)_c=\int_0^{\xi_{max}} d\xi_i\left(f(\xi_i)\;-f(0)\Theta(\xi_{cut}-\xi_i)\right)\frac{\log\xi_i}{\xi_i}\,. \tag{5.45}$$

5.2.3.3 n-body contributions

Finally, I turn to discuss the n-body cross-section, which, for clarity, can be decomposed into four terms

$$d\sigma^n=d\sigma^n_{\mathcal{B}}+d\sigma^n_{C}+d\sigma^n_{S}+d\sigma^n_{\mathcal{V}}, \tag{5.46}$$

respectively, the born contribution, the integrated collinear and soft counterterms, and the virtual contribution.
The born contribution is simply

$$d\sigma^n_{\mathcal{B}}(P)=\mathcal{B}(P)d\Phi_n,\qquad P\in\mathcal{P}_n, \tag{5.47}$$

while the collinear and soft contributions can be written as

$$d\sigma^n_C(P)=\frac{\alpha_s}{2\pi}\mathcal{Q}(P)\mathcal{B}\,d\Phi_n, \tag{5.48}$$

$$d\sigma^n_S(P)=\frac{\alpha_s}{2\pi}\sum_{k=1}^{n_L+n_H+2}\sum_{l=k}^{n_L+n_H+2}\mathcal{E}_{kl}(m_k,m_l)\mathcal{B}_{kl}\,d\Phi_n\,. \tag{5.49}$$

I have introduced two functions, $\mathcal{Q}$ and $\mathcal{E}$, which correspond to the finite part of the integrated prefactors in Eqs. (5.40) and (5.39). Their explicit definition can be found in [99, 129]. Both functions depend on the parameters δ, ξ_{cut}, which have also been used in the subtraction of the soft and collinear divergences. As said before, any infrared-safe observable does not depend on these parameters, as the dependence from the n-body contribution exactly compensates for the dependence from the $(n+1)$-body one.

Finally, the virtual contribution is written as

$$d\sigma^n_{\mathcal{V}}(P) = \frac{\alpha_s}{2\pi}\mathcal{V}_{fin}(P)d\Phi_n, \tag{5.50}$$

in terms of the finite part of th virtual contribution $\mathcal{V}$, computed in the Conventional Dimensional Regularization (CDR) scheme.
For what concerns the computation of $\mathcal{V}_{fin}$, after the first methods inspired by Passarino and Veltman [139], many efforts have been spent in the recent years developing efficient numeric techniques [140–142] which have led to the construction several codes [98, 143–146], with different degrees of automation and generality.

To conclude the discussion on the FKS subtraction scheme I just want to stress again the fact that, once the necessary matrix-elements are provided, it can be applied to any process. A completely automatic implementation of this method (the only missing ingredient being $\mathcal{V}_{fin}$), based on MadGraph [74, 109], is available and is dubbed MadFKS [99].

5.3 Parton shower Monte Carlos

This section will be devoted to the presentation of PSMCs. Their role, as said in the introduction, is to fill the gap between parton-level events, where only a few final state partons, those taking part to the hard scattering, are taken into account, and what one observes at hadron-colliders, *i.e.*final states with thousands of hadrons. This is done in two stages: in the first stage, the shower, the PSMC includes extra QCD radiation by generating extra partons from those taking part to the hard scattering, until the non-perturbative QCD regime is reached. In the second stage, the hadronization, partons generated by the shower are clustered into color singlets forming the hadrons.

Sec. 5.3.1 and Sec. 5.3.2 will be dedicated respectively to the shower and hadronization stage. In Sec. 5.3.3 I will present the most widely used PSMCs.

5.3.1 Shower

During the shower the partons taking part to the hard scattering are evolved from the hard scattering scale down to a scale at which QCD is no longer perturbative. The dominant evolution comes from the emission of soft/collinear extra partons. Exploiting the collinear factorization, that will be presented in Sec. 5.3.1.1, it is possible to define a branching probability encoded by the so-called Sudakov form factor, as will be explained in Sec. 5.3.1.2. Using this branching probability, extra parton emission can be simulated. A slightly different approach has to be used for partons in the initial state, and this issue will be explained in Sec. 5.3.1.3.

5.3.1.1 The collinear factorization

As said, the first action of a PSMC is to generate extra partons from those present at the matrix-element level. This is achieved by exploiting the collinear factorization. Consider a scattering process with n final state legs, described by the matrix-element $\mathcal{M}_n$, and the same process with one extra parton, described by $\mathcal{M}_{n+1}$. If in the latter the angle θ_{ab} between two partons a, b becomes small, then it factorizes as

$$\lim_{\theta_{ab}\to 0} |\mathcal{M}_{n+1}|^2 \, d\Phi_{n+1} = |\mathcal{M}_n|^2 \, d\Phi_n \frac{dt}{t} dz \frac{d\phi}{2\pi} \frac{\alpha_s}{2\pi} P_{c\to ab}(z) \,. \tag{5.51}$$

The function $P_{c\to ab}(z)$ is the (unregularized) Altarelli-Parisi splitting kernel [138]. It is universal and only depends on the identity (spin and color) of the particles a, b, c (in Sec. 5.2 a different notation has been used).
t is called the "evolution variable". While in this example it identifies with the virtuality $p_c^2 = (p_a + p_b)^2$ of the particle c, in general other choices, such as the relative transverse momentum of particles a and b, or their angle, are possible. This freedom of choice is due to the fact that in the collinear limit one has

$$\frac{dp_c^2}{p_c^2} = \frac{dp_T^2}{p_T^2} = \frac{dE^2\theta_{ab}^2}{E^2\theta_{ab}^2} \,. \tag{5.52}$$

The variable z is called the "energy variable", and represent the relative energy of particle b with respect to c:

$$z = \frac{E_b}{E_c} \,. \tag{5.53}$$

The $z \to 1$ limit corresponds to emitting particle a with very low energy, and is therefore called the soft limit.

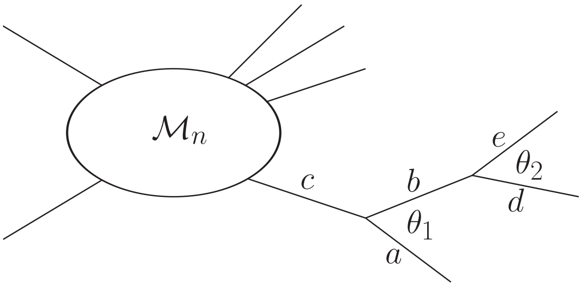

Figure 5.3.1: Sketch of the two extra emission configuration considered in Eq. (5.54)

This relation between n and $n+1$ final state particles can be easily extended to multiple emissions. Consider for instance the case of $n+2$ final particles sketched in Fig. 5.3.1. One has:

$$\lim_{\theta_{ab}\gg\theta_{de}\to 0} |\mathcal{M}_{n+2}|^2\, d\Phi_{n+2} = |\mathcal{M}_n|^2\, d\Phi_n\, \frac{dt_{ab}}{t_{ab}} dz_{ab} \frac{d\phi_{ab}}{2\pi} \frac{\alpha_s}{2\pi} P_{c\to ab}(z_{ab}) \times \\ \frac{dt_{de}}{t_{de}} dz_{de} \frac{d\phi_{de}}{2\pi} \frac{\alpha_s}{2\pi} P_{b\to de}(z_{de})\,. \qquad (5.54)$$

This means that one can approximate via m multiple splittings the leading behaviour of the matrix element $\mathcal{M}_{n+m}$ starting from $\mathcal{M}_n$. The regime of validity of this approximation is when each of the splittings is in the collinear limit, which turns into asking the following order for the angles θ_i of the i-th splitting:

$$\theta_1 \gg \theta_2 \gg \ldots \gg \theta_m\,. \qquad (5.55)$$

It is interesting to note that each splitting probability does not depend on the previous history of the system, so the whole process can be simulated as a Markov chain.

The angular ordering condition in Eq. (5.55) comes from the fact that the leading contribution to the $n+m$-body cross-section comes from

$$\sigma_{n+m} \simeq \sigma_n \alpha_s^m \int_{Q_0^2}^{Q^2} \frac{dt_1}{t_1} \int_{Q_0^2}^{t_1} \frac{dt_2}{t_2} \ldots \int_{Q_0^2}^{t_{m-1}} \frac{dt_m}{t_m} = \sigma_n \alpha_s^m \log^m\left(\frac{Q^2}{Q_0^2}\right). \qquad (5.56)$$

Where Q_0 is an infrared cutoff to separate perturbative and non-perturbative regime. As $\log\left(\frac{Q^2}{Q_0^2}\right)$ can be large, the perturbative expansion in α_s breaks down. Eq. (5.56) shows that a PSMC can reproduce the leading-logarithmic (LL) behaviour of the total

$m+n$ rate.

The so-called parton shower is indeed the branching sequence from a given leg, and describes the history of that given leg, starting from the hard subprocesses down to the non-perturbative region characterised respectively by the scale Q^2 and Q_0^2. Histories from different legs, as well as subsequent emission from one leg, are completely uncorrelated. The parton shower indeed misses all kind of interferences between the various legs, nevertheless it can predict the leading singularity of the matrix element. Missing the interferences also means missing the exact description of the color flow between the QCD particles. However, looking at the process from the point of view of the color flow can help in justifying the approach of the parton shower. Since interferences are always suppressed by some power of the number of colors N_c, neglecting them can be understood as working in the large N_c limit.
I turn now to a more rigorous definition of the splitting probability, which is needed since Eqs. (5.51)–(5.54) are divergent in the collinear limit.

5.3.1.2 The Sudakov form factor

In this section, I try to give a well-defined meaning to the concept of splitting probability. This is needed as one has to perform the parton shower as a subsequent sequence of splitting, starting from the hard scale down to the non-perturbative cutoff.
I start defining the probability dp for the splitting of parton c into partons a,b, between the two scales t and $t+dt$, knowing that no emission has occurred before. This is given by:

$$dp(t) = \frac{dt}{t}\int dz \frac{d\phi}{2\pi}\frac{\alpha_s}{2\pi}P_{c\to ab}(z)\,. \tag{5.57}$$

If now one has to define the probability $\Delta(Q^2,t)$ that no emission occurred from the scale Q^2 down to the scale t, he can proceed in the following way: divide the interval from t to Q^2 into many subintervals dt_k, for each of them consider the probability of non-splitting, and take the product of all this terms:

$$\begin{aligned}
\Delta(Q^2,t) &= \prod_k\left(1-\frac{dt_k}{t_k}\int dz\frac{d\phi}{2\pi}\frac{\alpha_s}{2\pi}P_{c\to ab}(z)\right)= \\
&= \exp\left(-\int_t^{Q^2}\frac{dt'}{t'}dz\frac{d\phi}{2\pi}\frac{\alpha_s}{2\pi}P_{c\to ab}(z)\right)= \\
&= \exp\left(-\int_t^{Q^2}dp(t')\right).
\end{aligned} \tag{5.58}$$

The probability $\Delta(Q^2, t)$ is commonly known as the "Sudakov form factor" or simply Sudakov.

As said before, the shower just associates an history to a given event, it does not change the probability that the event occurs. The property of unitarity is therefore mandatory for a parton shower, and I will now prove that it holds for the definition of probability given in Eq. (5.58). Unitarity can be reformulated as asking that

$$\sum_{k=0}^{\infty} P_k = 1\,, \tag{5.59}$$

where P_k is the probability of having exactly k splittings between the hard scale and the cutoff. To compute it, one can start from the probability dP_k of having k splittings, the first at scale t_1, the second at scale t_2 and so on, which is simply the product of the probability for each splitting:

$$dP_k = \Delta\left(Q^2, t_1\right) dp(t_1)\, \Delta\left(t_1, t_2\right) dp(t_2)\, \ldots\, \Delta\left(t_{k-1}, t_k\right) dp(t_k)\, \Delta\left(t_k, Q_0^2\right). \tag{5.60}$$

A remarkable property of the Sudakov is that

$$\Delta(t_a, t_b) = \Delta(t_a, t_c)\Delta(t_c, t_b)\,, \tag{5.61}$$

for $t_a > t_c > t_b$. This can be understood as computing the probability of not splitting between a and b as the product of the probabilities of not splitting between a and c and between c and b. Using this property Eq. (5.60) simply collapses to

$$dP_k = \Delta\left(Q^2, Q_0^2\right) \prod_{i=1}^{k} dp(t_i)\theta(t_{i-1} - t_i)\,, \tag{5.62}$$

from which the probability P_k of having k splittings regardless of their scale can be obtained integrating over t_i as

$$P_k = \int dt_1 \ldots dt_k dP_k = \Delta\left(Q^2, Q_0^2\right) \frac{1}{k!} \left(\int_{Q_0^2}^{Q^2} dp(t) \right)^k . \tag{5.63}$$

The probability of having any number of splitting is, as said, the sum of P_k, which can be easily computed as

$$\sum_k P_k = \Delta\left(Q^2, Q_0^2\right) \sum_k \frac{1}{k!} \left(\int_{Q_0^2}^{Q^2} dp(t) \right)^k = \Delta\left(Q^2, Q_0^2\right) \exp\left(\int_{Q_0^2}^{Q^2} dp(t) \right) = 1, \tag{5.64}$$

which terminates the proof.

The discussion about the Sudakov form factor up to this point has been not formally complete, as the infra-red singularity of the unregularized Altarelli-Parisi splitting kernels at $z = 1$ needs to be removed for the forms factors to be defined. So far the main focus has been given to extra emission matrix elements, which are know to be divergent when the extra parton becomes soft or collinear to any of the others. This divergence cancels with the corresponding one in the matrix element where the extra parton is virtual.
In fact the Sudakov encloses both the approximated real-emission and the approximated virtual matrix elements, and the cancellation of divergences between the two reflects into the unitarity of the shower.

In practice the z integration range is restricted from $[0,1]$ to $[z_{min}, z_{max}]$ with $0 < z_{min} < z_{max} < 1$, where the new integration bounds depend on the infra-red cutoff Q_0, for a virtuality-ordered shower as

$$z_{min} = 1 - z_{max} = \frac{1}{2}\left(1 - \sqrt{1 - 4\frac{Q_0^2}{t}}\right). \tag{5.65}$$

A similar relation holds also for p_T- and angular-ordered showers.
The t dependence of the integration bounds is responsible for the inclusion of the soft logarithms on top of the collinear ones.

5.3.1.3 Initial state radiation

The discussion which has been developed so far has taken care of the extra radiation coming from final state legs. At a hadron collider such as the Tevatron or the LHC, the problem of including extra radiation coming from initial state legs also appears.
The inclusion of final state radiation, carried out so far, proceeds forward in time, evolving the hard subprocess down to the cutoff scale. Using the same approach also for initial state radiation would mean to evolve from the proton to the hard scale, with the result of an extremely poor efficiency in getting the right kinematic configuration. The way initial state radiation is implemented in a PSMC is instead to evolve backward in time, from the hard kinematic back to the colliding hadrons. This is performed by applying the Dokshitzer-Gribov-Lipatov-Altarelli-Parisi (DGLAP) equation [138, 147–149] to evolve backward the parton distributions. I will now derive

these equations in a way which helps in applying them to the shower context.

The DGLAP equations regulate the evolution of parton distribution functions (PDFs)

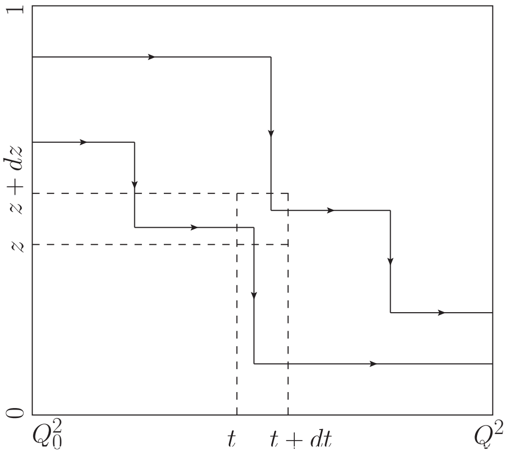

Figure 5.3.2: Representation of parton branching by paths in the (t,z) plane.

with respect to the process scale. The change of the PDF $f_a(z,t)$ when t is increased between t and $t+d_t$ can be pictorially represented as in Fig. 5.3.2. Starting from a single parton which carries the full momentum of the proton (hence $z=1$) at the proton scale, the probability that its evolution stops at the point (z,t) in the plane, is given by the difference between the number (or probability) of evolutions arriving at this point and the number of evolutions that from this point start. The number of evolutions arriving at the point can be understood as the probability of having a parent parton b with any energy $z' > z$ and the probability to branch into a in the interval between t and $t+dt$:

$$\begin{aligned} df_a^{in}(z,t) &= \frac{dt}{t}\sum_{bc}\int_z^1 dz'\int_0^1 dw f_b(z',t)\frac{\alpha_s}{2\pi}P_{b\to ac}(w)\delta(z-wz') = \\ &= \frac{dt}{t}\sum_{bc}\int_0^1 \frac{dw}{w} f_b\left(\frac{z}{w},t\right)\frac{\alpha_s}{2\pi}P_{b\to ac}(w)\,. \end{aligned} \tag{5.66}$$

Similarly, the number of evolutions starting from (z,t) is the probability to find a parton b at (z,t) times the probabilities that it branches to a parton a with any energy fraction $z' < z$:

$$df_a^{out}(z,t) = \frac{dt}{t}\sum_{bc} f_b(z,t)\int_0^z dz'\int_0^1 dw\frac{\alpha_s}{2\pi}P_{b\to ac}(w)\delta(z'-wz) =$$

$$= \frac{dt}{t}\sum_{bc} f_b(z,t)\int_0^1 dw\frac{\alpha_s}{2\pi}P_{b\to ac}(w)\,. \tag{5.67}$$

Therefore the variation in f_a is

$$\begin{aligned} df_a(z,t) &= df_a^{in}(z,t) - df_a^{out}(z,t) = \\ &= \frac{dt}{t}\sum_{bc}\int_0^1 dw\frac{\alpha_s}{2\pi}P_{b\to ac}(w)\left(\frac{1}{w}f_b\left(\frac{z}{w},t\right) - f_b(z,t)\right) = \\ &= \frac{dt}{t}\sum_{bc}\int_0^1 \frac{dw}{w}\frac{\alpha_s}{2\pi}\,P_{b\to ac}(w)|_+ f_b\left(\frac{z}{w},t\right), \end{aligned} \tag{5.68}$$

from which one can define the (azimuth-averaged) probability $d\hat{p}(t)$ of a backward emission as

$$d\hat{p}(t,z) = \frac{df_a(z,t)}{f_a(z,t)} = \frac{dt}{t}\sum_{bc}\int_0^1 \frac{dw}{w}\frac{\alpha_s}{2\pi}\,P_{b\to ac}(w)|_+\,\frac{f_b\left(\frac{z}{w},t\right)}{f_a(z,t)}\,. \tag{5.69}$$

Analogously to what has been done for final state radiation, the initial state Sudakov is defined as

$$\hat{\Delta}(Q^2,t,z) = \exp\left(-\int_t^{Q^2} d\hat{p}(t)\right). \tag{5.70}$$

5.3.2 Hadronization

I will now briefly cover how hadronization is performed. A detailed explanation of the underlying non-perturbative physics exceeds the aims of this thesis, and can be found e.g. in [150, 151].

When all the partons generated by the shower are characterized by a scale below the cutoff Q_0 the shower stops, and these partons are put on their mass-shell. In order to give a picture of the event as close as possible as what happens in nature, these partons need to be combined into color-singlet hadrons. The physics of hadronization is highly non-perturbative, and to build a model to explain this phenomenon is very delicate. Fortunately, some features of perturbative QCD come to help in this task.

The most important of these features is the color-preconfinment. In the case of angular-ordered showers (*i.e.*showers in which the evolution variable t is related to the angle of the splitting), this is most apparent: consider a quark from the hard process which radiates gluons. Angular ordering will enforce these gluons to be close in the phase space. Furthermore, as shown in Fig. 5.3.3 two subsequently emitted gluon can

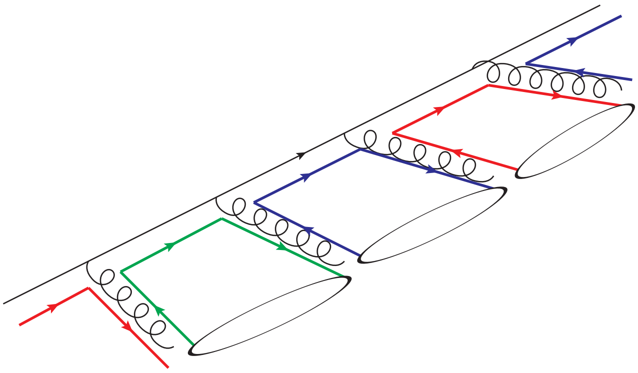

Figure 5.3.3: Color flow in the emission of multiple gluons off a quark line. Two subsequent gluons can always form a color-singlet, represented as a blob in the picture.

always form a color singlet. This leads naturally to the clustering in phase-space of color-singlet parton pairs, strongly suppressing long-range color correlations. This approach to hadronization is known as the "cluster model".

An alternative approach is inspired from the low-energy behaviour of QCD. At low energies the color confinement potential of a $q\bar{q}$ pair grows linearly with their distance, and can be modeled with a sting of uniform tension. Gluons which color-connects the two quaks can be seen as excitations (or kinks) of the string. Such a string can reach a more energetically favorable condition if it breaks by the creation of a new $q\bar{q}$ pair. Once all strings have been created, hadrons are created starting from them as clusters. The two approaches here discussed, the cluster and the string model, are the ones mostly used in the available PSMCs.

5.3.3 Commonly used PSMCs

I will conclude the section on PSMCs by quickly presenting the most known implementations.

5.3.3.1 HERWIG

The two versions of the HERWIG [152] PSMC, HERWIG6 [69, 70] in Fortran and the more modern HERWIG++ [153] in c++ are an example of angular-ordered showers, where subsequent emissions are characterized by smaller and smaller angles.

In an angular-ordered PSMC the parton shower, which does not retain all the matrix-element correlations, cannot populate the full phase-space. Some regions of the phase space, called dead-zones, are left without radiation. This enforces the shower to act only in the region where it is supposed to be reliable, which is the region controlled by the collinear approximation. The cluster model is used for the hadronization.

5.3.3.2 PYTHIA

As happens for HERWIG, two versions the PYTHIA PSMC, in FORTRAN and C++ are available. The first is known as PYTHIA6 [150], the second as PYTHIA8 [154]. PYTHIA6 allows both for virtuality and p_T ordered showers, while PYTHIA8 is only p_T ordered. Using such variables, on one hand gives a more physical interpretation of the scale of each splitting, but on the other hand does not guarantee any longer the property of having decreasing angles. Angular ordering is restored in PYTHIA6 by rejecting the events that do not obey it. In PYTHIA8 no rejection is done, since angular ordering violation effects are very small for a p_T ordered shower. PYTHIA showers typically populate all the phase space without dead-zones.
In both versions the string model is used for hadronization.

5.3.3.3 SHERPA

The last PSMC that I will discuss is SHERPA [155]. While HERWIG and PYTHIA are based on the collinear picture to generate the shower which is done by subsequential $1 \to 2$ splittings, SHERPA is based on the soft picure. While in the collinear picture the radiated parton only knows about one other particle (the one which it has to be collinear to), a soft particle k need to know all the two pair i and j which it can connect. This is the dipole picture [127, 128], which approximate the extra emission matrix element by a sum of dipoles $D_{ij,k}$ in the leading color approximation:

$$|\mathcal{M}_{n+1}|^2 \simeq \sum_{ij} D_{ij,k} = |\mathcal{M}_n|^2 \sum_{ij} \frac{\alpha_s}{p_i \cdot p_j} K_{ij,k}\,, \tag{5.71}$$

where $K_{ij,k}$ is in the soft limit of what the Altarelli-Parisi splitting functions are in the collinear one.
The soft limit has the advantage of automatically ensuring the angular ordering.
Each of these splitting is now a $2 \to 3$ splitting, driven by a Sudakov of the form

$$\Delta\left(t, Q^2\right) = \exp\left(-\int_t^{Q^2} \frac{dt}{t} \int dz \alpha_s K_{ij,k}\right). \tag{5.72}$$

Hadronization is carried out in the cluster model.

5.4 Matching NLO computations with parton showers

In the previous section I introduced PSMCs and briefly explained how they work, adding extra emissions to the matrix-element exploiting the collinear factorization. However in general they fail in describing correctly extra hard emissions, for which the collinear factorization clearly breaks down; furthermore, the accuracy of observables is quite poor, since the events that are passed to the shower are computed at LO. The first of these two limitations is solved by including higher multiplicity matrix-elements in the simulation, in order to have the exact description of the first extra emissions, with a suitable prescription to avoid double counting [156, 157].
The second limitation is solved by showering events generated at NLO accuracy. This is not as simple as it may seem for at least two reasons: since the real-emission matrix-element of a NLO calculation diverges, naive (unweighted) event generation is impossible; moreover, one must avoid double counting the emission generated by the shower and the one included by the real-emission.

This section will be devoted to describe how NLO computations can be matched to a PSMC in two different approaches, MC@NLO [135] and POWHEG [133, 134]. I will introduce the two approaches respectively in Sec. 5.4.1 and Sec. 5.4.2. A more detailed description and a general comparison of the two methods can be found in [158].

5.4.1 MC@NLO

In order to understand how NLO corrections and parton showers can be matched in the MC@NLO framework, I start from the definition of the differential LO, NLO and shower (MC) cross-section:

$$d\sigma_{LO} = d\Phi_n \mathcal{B}, \tag{5.73}$$

$$d\sigma_{NLO} = d\Phi_n \left(\mathcal{B} + \mathcal{V} + d\Phi_1 \mathcal{R}\right), \tag{5.74}$$

$$d\sigma_{MC} = d\Phi_n \mathcal{B} I^n_{MC}(O) dO, \tag{5.75}$$

where $\mathcal{B}$, $\mathcal{V}$ and $\mathcal{R}$ are respectively the Born, virtual and real-emission matrix-element (I assume n final state legs for the Born matrix-element), $I^n_{MC}(O)$ is the spectrum for observable O generated by the parton shower starting from n final state particles.

One may be tempted to simply extend Eq. (5.77) to NLO, by writing

$$d\sigma_{MC@NLO} = \Big[(\mathcal{B}+\mathcal{V})\; d\Phi_n\; I^n_{MC}(O) + \mathcal{R}\, d\Phi_n\; d\Phi_1\; I^{n+1}_{MC}(O)\Big] dO\,. \tag{5.76}$$

This naive definition is not correct for two reasons: the first is that the real-emission and the virtual matrix-element are divergent, therefore the n and $n+1$ body configurations will not be finite. This could be regulated by an infrared cutoff, however the generation of unweighted event will be extremely inefficient, and, at the end of the day, one should prove the independence of results upon this cutoff. The second reason is that some configurations in Eq. (5.76) are double counted.

Both these issues can be cured by modifying Eq. (5.76) introducing the so-called Monte Carlo counterterms MC:

$$\frac{d\sigma_{MC@NLO}}{dO} = \left(\mathcal{B}+\mathcal{V}+\int d\Phi_1 MC\right) d\Phi_n\; I^n_{MC}(O) + (\mathcal{R}-MC)\, d\Phi_n\; d\Phi_1\; I^{n+1}_{MC}(O)\,. \tag{5.77}$$

The Monte Carlo counterterm is defined as the cross-section for the first emission in the parton shower. Its expression is

$$MC = \left|\frac{\partial\left(t^{MC}, z^{MC}, \phi\right)}{\partial\Phi_1}\right| \frac{1}{t^{MC}} \frac{\alpha_s}{2\pi} \frac{1}{2\pi} P\left(z^{MC}\right)\mathcal{B}\,. \tag{5.78}$$

MC has the remarkable property of having the same soft and collinear singularities as $\mathcal{R}$, so it also acts as a local counterterm, allowing for numerical integration and for the generation of unweighted events. It is process independent, only depending on the chosen PSMC.
Finally it can be proven that Eq. (5.77) avoids double counting, and is correctly normalized to the NLO rate.
To begin the proof, I expand the shower operator $I^n_{MC}(O)$ considering only the case of 0 or 1 emission (see also Eq. (5.62)):

$$I^n_{MC}(O) = \Delta + \Delta d\Phi_1 \frac{MC}{\mathcal{B}}\,, \tag{5.79}$$

where the arguments in the Sudakov have been dropped for simplicity. The Sudakov form factor Eq. (5.58) written in terms of MC has the simple expression

$$\Delta\left(Q^2, Q_0^2\right) = \exp\left(-\int d\Phi_1 \frac{MC}{\mathcal{B}}\right), \tag{5.80}$$

so that the expansion of $I^n_{MC}(O)$ up to order α_s reads

$$I^n_{MC}(O) = 1 - \int d\Phi_1 \frac{MC}{\mathcal{B}} + d\Phi_1 \frac{MC}{\mathcal{B}} \,. \tag{5.81}$$

It is understood that MC, as well as $\mathcal{V}$ and $\mathcal{R}$, has one extra power of α_s with respect to $\mathcal{B}$.
To conclude the proof, I simply insert the expansion Eq. (5.81) into Eq. (5.77), keeping only the terms which are genuine NLO:

$$\begin{aligned} \frac{d\sigma_{MC@NLO}}{dO} &= \mathcal{B}\left(1 - \int d\Phi_1 \frac{MC}{\mathcal{B}} + d\Phi_1 \frac{MC}{\mathcal{B}}\right) d\Phi_n + \mathcal{V}\, d\Phi_n + \int d\Phi_1\, MC\, d\Phi_n \\ &\quad + \mathcal{R}\, d\Phi_n\, d\Phi_1 - MC\, d\Phi_n\, d\Phi_1 = \\ &= \mathcal{B}\, d\Phi_n + \mathcal{V}\, d\Phi_n + \mathcal{R}\, d\Phi_n\, d\Phi_1 \,, \end{aligned} \tag{5.82}$$

which completes the proof.

The MC@NLO matching described so far reproduces the shape of the chosen PSMC in the soft-collinear region, where $\mathcal{R} - MC$ is very small. In this region the normalization takes into account also the contribution from the virtuals. In the hard region, where MC is zero, all the observables are dominated by $\mathcal{R}$, as they should.

In practice, events with n and $n+1$ final state partons, respectively called $\mathbb{S}$ and $\mathbb{H}$ events, are generated according to Eq. (5.77). Because of the inclusion of the MC counterterms, both samples correspond to a finite cross-section.
Given the fact that the difference $\mathcal{R} - MC$ can be negative, the events are unweighted up to the sign. To deal with this, one has to compute the integrals of the $\mathbb{S}$ and $\mathbb{H}$ contributions, and those of their absolute value. If I call I the integrands and J their absolute values, then events are distributed according to J, with the sign of their weight according to the sign of I.
The generation of negative weights is not a problem as long as enough events are generated to neglect statistical fluctuations. Indeed, all distributions are positively definite as they should, apart from fluctuations. Negative weight only affect the efficiency, defined as the number of events to be generated in order to get smooth histograms.

MC@NLO, which is born as a library of processes coded by hand [159], counts now some 30 processes matched to HERWIG6 and HERWIG++ and a few matched to PYTHIA6 Q^2-ordered [160].

Quite recently, aMC@NLO [68], has come as the automatic version of MC@NLO, where automatic means that, given a process as input, the code to generate events in the MC@NLOframework is written on the fly. aMC@NLO relies on MadGraph [74,161] for the matrix element generation, MadLoop [98], which is based on the OPP [140] method as implemented in CutTools [162] to compute virtual matrix-elements, and MadFKS [99] for the computation of the counterterms and for the phase-space integration.

5.4.2 POWHEG

POWHEG is a NLO matching framework alternative to MC@NLO, with the distinguishing feature of having only positive-definite weights. While MC@NLO can be seen as subtracting from the real-emission matrix element the first emission that would be generated by the shower before showering the event, POWHEG generates itself the hardest emission (with the largest p_T) with its own Sudakov, then it passes the event to the shower.

Using the notation of Sec. 5.4.1, the hardest-emission LO cross-section is defined as

$$d\sigma_{LO} = d\Phi_n \mathcal{B}\Big(\Delta\big(Q^2,Q_0^2\big) + \Delta\big(Q^2,t\big)MC\Big)\,, \tag{5.83}$$

and corresponds to the probability of having zero emission, or an emission at scale t following by any number of emissions at lower scale.

A naive extension at NLO of Eq. (5.83) would be

$$d\sigma_{POWHEG} = d\Phi_n\left(\mathcal{B}+\mathcal{V}+\int d\Phi_1\mathcal{R}\right)\left(\Delta\big(Q^2,Q_0^2\big)+\Delta\big(Q^2,t\big)\frac{MC}{\mathcal{B}}\right), \tag{5.84}$$

but it is found not to be correct, as it does not reproduce the NLO expansion (last line of Eq. (5.82)) once expanded at $\mathcal{O}(\alpha_s)$. It is easy to see that the mismatch can be traced back to terms proportional to $\mathcal{R}-MC$, which suggests to introduce a modified Sudakov factor with the replacement $MC \to \mathcal{R}$

$$\tilde{\Delta}\big(Q^2,Q_0^2\big) = \exp\left(-\int d\Phi_1\frac{\mathcal{R}}{\mathcal{B}}\right), \tag{5.85}$$

corresponding to a modified splitting probability

$$d\tilde{p} = d\Phi_1\frac{\mathcal{R}}{\mathcal{B}}\,. \tag{5.86}$$

Indeed this replacement correctly reproduces the NLO expansion at $O(\alpha_s)$.
The POWHEG cross-section is thus defined as

$$d\sigma_{POWHEG} = d\Phi_n\left(\mathcal{B}+\mathcal{V}+\int d\Phi_1\mathcal{R}\right)\left(\tilde{\Delta}\left(Q^2,Q_0^2\right)+\tilde{\Delta}\left(Q^2,t\right)\frac{\mathcal{R}}{\mathcal{B}}\right), \tag{5.87}$$

As the real-emission matrix element does not depend on the chosen parton-shower, events generated by POWHEG can be passed to any PSMC, unlike those generated by MC@NLO. However a definition of the Sudakov such as that in Eq. (5.85) exponentiates also the finite part of the real-emission matrix-element, introducing extra higher-order contributions than those generated by the shower. Such contributions, which, are formally higher order, can affect observables in certain kinematic configurations [163].
This issue is cured by damping the real-matrix element in the Sudakov with the function

$$f(p_T^2) = \frac{h^2}{h^2+p_T^2}\,. \tag{5.88}$$

The limit $h \to \infty$ corresponds to no damping, and is the default setting in POWHEG.

POWHEG is distributed as a process library, giving also a framework to allow the user to implement new processes, the so-called POWHEG-box [164]. Several level of automation of this framework exist: POWHEL is an interface of POWHEG and Helac-NLO [165], which provides the necessary contributions to automatically compute a NLO cross-section. An interface exploiting MadFKS also exists [166], which however needs the user to link virtual matrix-elements from external codes.

5.5 NLO predictions for VBF matched with parton shower

In this section I will present predictions for VBF observables obtained in the MC@NLO (using the automatic aMC@NLO version) and POWHEG frameworks, for a 125 GeV SM Higgs boson at the $\sqrt{S} = 8\,\text{TeV}$ LHC. As the matching with the parton shower is performed differently in the two approach, this comparison helps in better understanding the possible systematics. Furthermore, for both POWHEG and aMC@NLO I will present results obtained by the matching with HERWIG6, virtuality ordered Pythia6 and HERWIG++.
Before showing the results in Sec. 5.5.2, I will discuss in Sec. 5.5.1 the setup for POWHEG and aMC@NLO and the cuts used in the analyse.

5.5.1 Setup: parameters and cuts

I will now list the input parameters and cuts used in this compuatation. The values for the SM parameters used in the computation are those recommended by the Higgs Cross-Section Working Group (HXSWG) [35]:

$$\begin{aligned} M_W &= 80.398\,\mathrm{GeV}, & \Gamma_W &= 2.089\,\mathrm{GeV}, \\ M_Z &= 91.188\,\mathrm{GeV}, & \Gamma_Z &= 2.496\,\mathrm{GeV}, \\ G_F &= 1.166\times 10^{-5}\,\mathrm{GeV}^{-2} & . \end{aligned} \tag{5.89}$$

Results are computed using the MSTW 2008 NLO pdf set [71], with errors estimated at 68% confidence level. Renormalization and factorization scales are fixed to the W mass. The choice of a dynamic scale choice will be discussed in App. C, and will be shown not to have any drastic effect on all observables.

Parton level events are generated without imposing cuts[3], and each sample consists of one million events. After shower and hadronization, typical cuts used in experimental VBF analyses are applied: hadrons are clustered into jets by using the anti-k_T algorithm [75] as implemented in FastJet [76], with $\Delta R = 0.5$. At least two jets are required, with $p_T > 20\,\mathrm{GeV}$ and $|y| < 4.5$. Furthermore, the two hardest jets (*i.e.*the two jets with the largest transverse momenta) passing these criteria are asked to have an invariant mass $m(j_1, j_2) > 600\,\mathrm{GeV}$ and a rapidity separation $|y(j_1) - y(j_2)| > 4$.

The generation of VBF in aMC@NLO (in the five-flavour scheme) is simply done by typing the following lines in the aMC@NLO shell:

```
import model loop_sm-no_b_mass
define p = g u c d s b u~ c~ d~ s~ b~
define p = j
generate p p > h j j $$ w+ w- z [QCD]
```

Note the $$ sign used not to include diagrams with a W or a Z in the s-channel.

The aMC@NLO event files store additional informations in order to obtain scale and PDF uncertainties via reweighting, *i.e.*without the need of extra runs [167].

For what concerns POWHEG, the original computation of VBF [168] has been used, as it is publicly available in the POWHEG-box.

---

[3] In order not to have numerical instabilities, at least two jets with $p_T > 2\,\mathrm{GeV}$ are required in the aMC@NLO samples. This cut is however completely irrelevant for what concerns distributions and total rates.

In all cases, no simulation of the underlying event is performed by the PSMC.

5.5.2 Results

I will now present the results obtained for various kinematic observables. For simplicity, the same format is kept for all figures: in the upper frame of each figure, the three curves that correspond to the aMC@NLO samples are shown: black solid for HERWIG6, red dashed for Pythia6 and blue dot-dashed for HERWIG++. Below the plots, the first and second insets shows the ratios for the aMC@NLO and POWHEG samples over the fixed order NLO, in order to assess the impact of the different PSMC on the observable (same pattern as the main frame). The third inset shows the scales (red dashed) and PDF (black solid) uncertainty band, computed from the aMC@NLO plus HERWIG6 sample. Scale uncertainties are computed varying independently the factorization and renormalization scale in the range

$$\frac{M_W}{2} < \mu_R, \mu_F < 2M_W\,, \tag{5.90}$$

while PDF errors are computed with the Hessian method [100], as it is the prescription for the MSTW set.

Most of the differences which will appear in the first and second insets are mainly due to the impact of the VBF cuts on the different PSMCs. To better understand this effect, in Tab. 5.5.1 I quote the ratios of the matched cross-section after cuts and the fixed order NLO one ($\sigma^{NLO}_{CUTS} = 0.388(2)\,\text{pb}$). It can be highlighted that these ratios are all smaller than one, as typically parton showers tend to spread the radiation hardness in the phase space, therefore slightly more events will fail the cuts. On top of this, there is a clear pattern $\sigma_{HW6} > \sigma_{PY6} > \sigma_{HW++}$ both for POWHEG and aMC@NLO. These differences are quite large, specially if compared with the size of NLO theoretical uncertainties and/or with the NNLO effects on the total cross section. They have been found to depend on the way extra radiation is generated by the shower, in particular on how much of this radiation is lost because it falls outside the jet “cone”. Furthermore, they are found to depend also on the details of the hadronization model. A more inclusive jet definition, with larger jet radii, reduces these differences, as it is explained in App. D.

In Fig. 5.5.4, Fig. 5.5.5 and Fig. 5.5.6 I show the transverse momentum and rapidity respectively of the Higgs boson, and of the first and second jet. As all these observable are computed at NLO accuracy, I expect general agreement among the two different implementations of the parton shower matching as well as among different PSMCs. Indeed, all NLO-matched curves are fairly compatible with each other once the ratios in table Tab. 5.5.1 and the theoretical uncertainties in the lower insets are taken into

	HERWIG6	PYTHIA6	HERWIG++
AMC@NLO	0.93	0.89	0.83
POWHEG	0.92	0.86	0.83

Table 5.5.1: Ratios of matched NLO+PSMCs and fixed order NLO cross-sections in the AMC@NLO and POWHEG formalism.

account. The comparison with the fixed-order NLO prediction, on top of the overall normalisation effect already shown in table 5.5.1, displays a consistent action of the shower in affecting the jet spectra, an effect which is increasingly important as one moves downwards in the jet hierarchy (*i.e.* from the hardest to the softest jets); in fact this trend will become even more evident in the case of the third jet (see later). As a consequence of the recoil against the shower-enriched jet activity, NLO-matched curves display harder and more central Higgs-boson distributions. For the observables shown in these figures, PDF and scale uncertainties are generally small (typically of the order of ±3% to ±5%), and fairly constant, with only mild increases at large transverse momenta.

Similar consideration can be done for the azimuthal separation between the two tagging jets, shown in the top plot of Fig. 5.5.7, which also show excellent agreement between fixed order ad matched computations. This is extremely comforting, since this observable is very sensitive to the Higgs boson properties, such as spin and parity and therefore any theoretical uncertainty can reflect on the Higgs properties determination [169–172].

Shower effects are more important for observables such as the invariant mass or the rapidity separation of the two hardest jets. These observable, shown in Fig. 5.5.8 can probe extreme kinematic configurations, where the two jets lie at very large rapidities in opposite hemispheres. As the energy of a (massless) parton is written in terms of its p_T and rapidity as[4]

$$E = p_T \cosh y, \tag{5.91}$$

a parton at the edge of the p_T and rapidity region allowed by the cuts will have an energy $E \simeq 1\,\mathrm{TeV}$. Therefore such partons at large rapidity will typically have a transverse momentum just above the cut, and, because of this, they will be very sensitive to shower effects. This is reflected in the quite large deficit (20-30 %) at large invariant mass and rapidity separation of the matched curves with respect to the fixed order NLO one. In the same region, it is possible to see the theoretical uncertainties which start growing, in particular at large rapidity difference. For the PDFs this corresponds

---

[4] This expression holds also for massive particles, if one replaces $p_T \to m_T = \sqrt{p_T^2 + m^2}$.

to the larger uncertainty at $x \sim 1$, whereas for the scale uncertainty this can be understood as the inadequacy of the choice $\mu_{R,F} = M_W$ in a region dominated by radiation just above the 20 GeV cut. Indeed, a dynamic scale choice (see App. C) cures the growth of the scale uncertainty band, without affecting the central value.
Observables related to the third jet are more sensitive to the different matching procedures and to the effect of parton showers, because their description at the matrix-element level is only LO. In the bottom plot of Fig. 5.5.7 the exclusive jet multiplicity is shown. While the two-jet bin reflects the ratios in Tab. 5.5.1, the three-jet bin shows larger deviations, with POWHEG predicting less events than aMC@NLO. The deficit with respect to the fixed-order result in this bin ranges from 15% to 20% for aMC@NLO, whereas it is larger, 30% or more, for POWHEG, irrespectively of the PSMC employed. This indicates that such an effect is mainly a matching systematics rather than being induced by different shower models. It has to be stressed, however, that the POWHEG and aMC@NLO predictions are still compatible within scale uncertainties, which for the 3-jet bin are about ±10%, consistently with the LO precision of this observable. From the 4-jet bin onwards, the description is completely driven by the leading-logarithmic (LL) accuracy of the showers and by the tunes employed, which translates in large differences among the various generators. For such jet multiplicities, theoretical-uncertainty bands are completely unrepresentative. The fixed order prediction for these bins is zero.
The 3-jet-bin pattern described above determines the normalisation of the third-jet transverse-momentum and rapidity distributions, shown in figure Fig. 5.5.9. These variables can be significantly affected by the different radiation produced by the PSMC's. In particular the aMC@NLO results, which are quite close to the pure NLO on average, display a ±15% dependence on the shower adopted. Conversely, the three POWHEG predictions are slightly closer to each other; we reckon that this is a consequence of the hardest emission being generated in this formalism by a Sudakov which is independent of the actual PSMC employed, as already mentioned in the introduction. The POWHEG curves show a 30%-deficit with respect to the pure NLO, and are more central and softer than the aMC@NLO ones. Scale uncertainties are again compatible with the LO nature of these observables, of the order of ±10% in the whole rapidity range, and growing from ±10% to ±20% with transverse momentum.

Before concluding this section, one more set of observables has to be considered. Because of the peculiar radiation pattern of VBF, which prefers radiation far from the central region, one way to reduce the contamination coming from background processes as well as from other production channels (e.g. gluon fusion) is to reject the event if an extra jet, called veto-jet, is found within the two hardest jets:

$$\min(y_1, y_2) < y_{veto} < \max(y_1, y_2)\,. \tag{5.92}$$

The predictions for the transverse momentum and rapidity of the veto jet are shown in figure Fig. 5.5.10. The definition in equation (5.92) implies that the more central the third jet, the larger the probability that it be the veto jet. Since POWHEG predicts a more central third jet with respect to aMC@NLO, the veto condition has the effect that the two predictions for the veto jet are slightly closer to each other than for the third jet. aMC@NLO yields visibly less central distributions, predicting larger rates (up to 20% to 30%) with respect to the pure NLO at small transverse momentum and large rapidity. The POWHEG predictions for the transverse momentum are softer than aMC@NLO (with the exception of the matching to Pythia6, where shapes are similar), while rapidities are more central, with 20%- to 30%-discrepancies with respect to the pure NLO at the edges of the spectra. As was the case for the third-hardest jet, observables related to the veto jet are described only at LO accuracy, and affected by large uncertainties, roughly ±15%.

5.6 Conclusion and outlook

In this chapter I have presented the results for VBF at next-to-leading order accuracy, matched with parton shower. After having presented the principles underlying the way parton showers work, I have shown the problems that arise when they are applied to NLO computations. To solve these problems, two matching schemes are known, MC@NLO and POWHEG, and have been presented.

I continued the chapter showing predictions for several VBF observables, obtained using different parton-shower Monte-Carlos. I have shown that there is a non-trivial interplay between the shower and hadronization details and the cuts applied to the events, which can be seen in the $O(5-10\%)$ differences in the rate after cuts obtained with different PSMCs. The proper way these differences have to be considered, since they cannot be simply estimated via scale variations, may be the subject for further studies. Once such differences are taken into account, predictions for observables described with NLO accuracy at the parton level display small theoretical uncertainties, up to ±5%, and show a good agreement between the two matching schemes. Differences with respect to the pure-NLO predictions result from the action of the shower on the jet activity of the events. For quantities described with LO precision, theoretical uncertainties are consistently larger, of the order of ±10% to ±15%, as well as the discrepancy between the two matching prescriptions, with aMC@NLO generally closer to the fixed-order NLO than POWHEG; in particular there is a visible effect in the observables related to the third jet. Still, all results are largely compatible once theoretical error bands are taken into account.

In order to improve the description of these observables, one should either consider VBF + 1 jet at NLO, which is known at fixed order [93], or, better, generate an Fx-Fx matched [173] event sample including both 0 and 1 extra-jet.

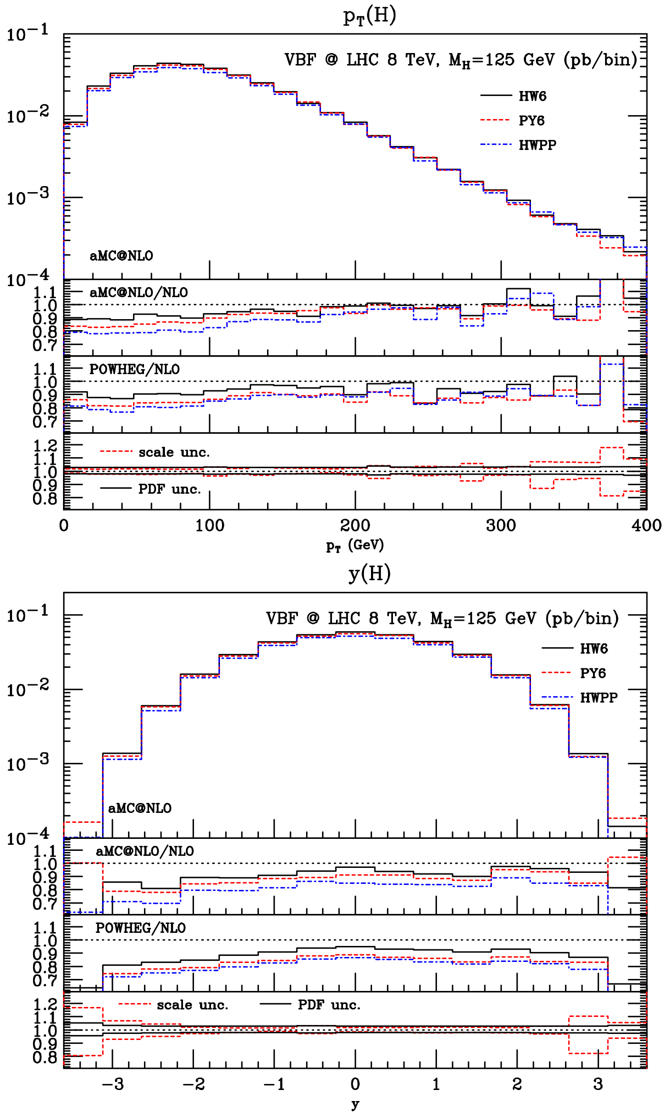

Figure 5.5.4: Higgs boson transverse momentum (top) and rapidity (bottom) distributions for VBF. The main frame shows the aMC@NLO samples, matched with HERWIG6 (black solid), virtuality-ordered Pythia6 (red dashed) and HERWIG++ (blue dot-dashed). The first (second) inset shows the ratios of the aMC@NLO (POWHEG) distributions over the fixed-order NLO one, with the same color pattern as the main frame. The third inset shows scale (red-dashed) and PDF uncertainties (black solid) computed from the aMC@NLO + HERWIG6 sample. Scale uncertainties are obtaining by varying independently the renormalization and factorization scale in the range $M_W/2 < \mu_R, \mu_F < 2M_W$. The MSTW 2008 NLO PDF set has been used, with error bands corresponding to 68% confidence level.

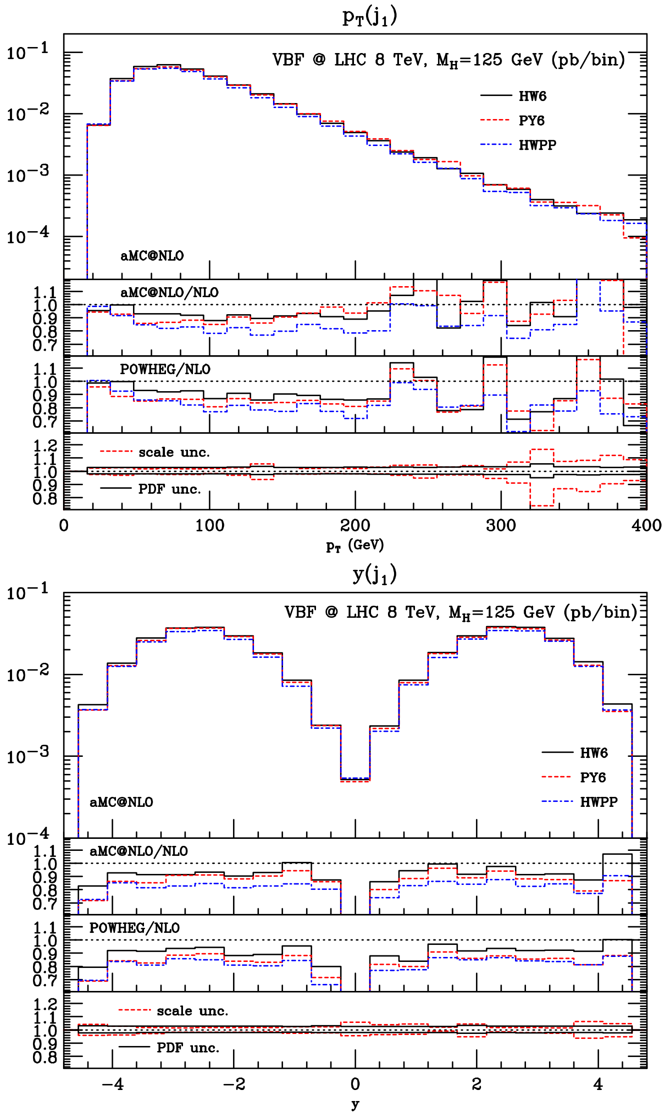

Figure 5.5.5: Hardest jet transverse momentum (top) and rapidity (bottom) distributions for VBF. The main frame shows the aMC@NLO samples, matched with HERWIG6 (black solid), virtuality-ordered Pythia6 (red dashed) and HERWIG++ (blue dot-dashed). The first (second) inset shows the ratios of the aMC@NLO (POWHEG) distributions over the fixed-order NLO one, with the same color pattern as the main frame. The third inset shows scale (red-dashed) and PDF uncertainties (black solid) computed from the aMC@NLO + HERWIG6 sample. Scale uncertainties are obtaining by varying independently the renormalization and factorization scale in the range $M_W/2 < \mu_R, \mu_F < 2M_W$. The MSTW 2008 NLO PDF set has been used, with error bands corresponding to 68% confidence level.

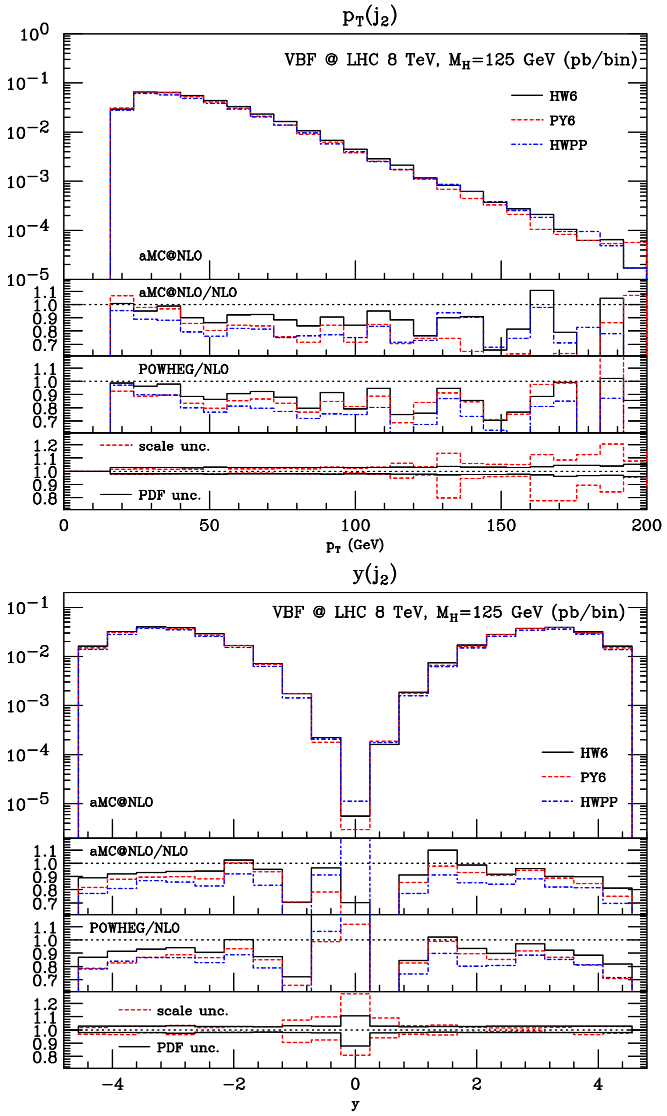

Figure 5.5.6: Second hardest jet transverse momentum (top) and rapidity (bottom) distributions for VBF. The main frame shows the aMC@NLO samples, matched with HERWIG6 (black solid), virtuality-ordered Pythia6 (red dashed) and HERWIG++ (blue dot-dashed). The first (second) inset shows the ratios of the aMC@NLO (POWHEG) distributions over the fixed-order NLO one, with the same color pattern as the main frame. The third inset shows scale (red-dashed) and PDF uncertainties (black solid) computed from the aMC@NLO + HERWIG6 sample. Scale uncertainties are obtaining by varying independently the renormalization and factorization scale in the range $M_W/2 < \mu_R,\mu_F < 2M_W$. The MSTW 2008 NLO PDF set has been used, with error bands corresponding to 68% confidence level.

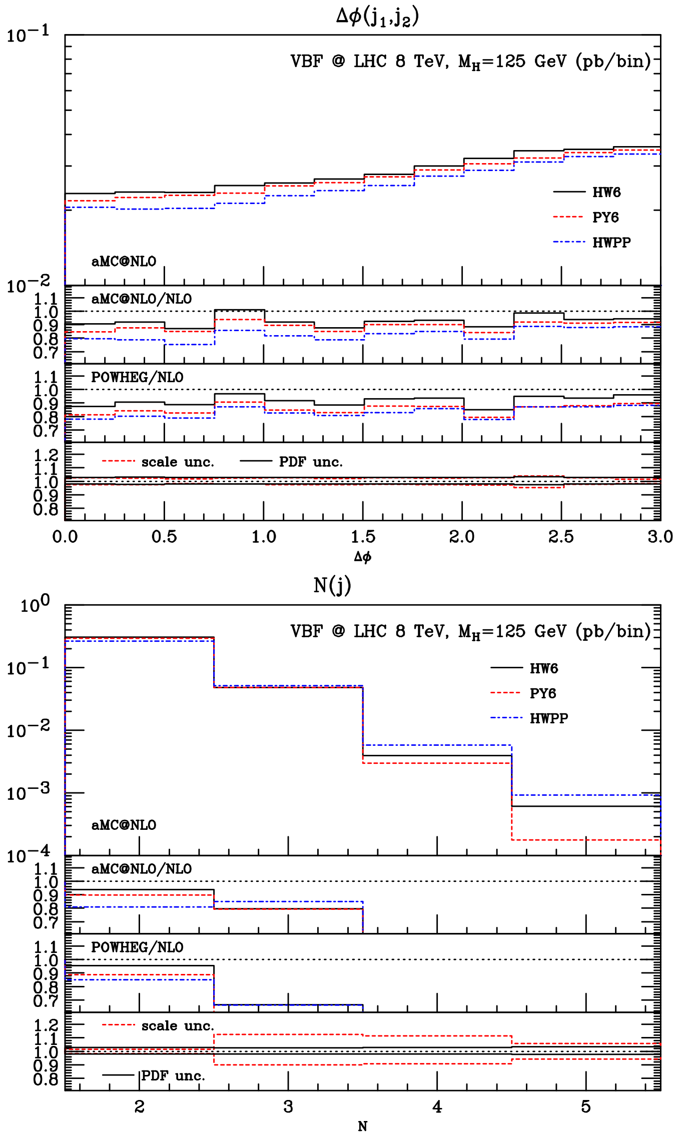

Figure 5.5.7: Azimuthal separation of the two hardest jets (top) and exclusive jet multiplicities (bottom) distributions for VBF. The main frame shows the aMC@NLO samples, matched with HERWIG6 (black solid), virtuality-ordered Pythia6 (red dashed) and HERWIG++ (blue dot-dashed). The first (second) inset shows the ratios of the aMC@NLO (POWHEG) distributions over the fixed-order NLO one, with the same color pattern as the main frame. The third inset shows scale (red-dashed) and PDF uncertainties (black solid) computed from the aMC@NLO + HERWIG6 sample. Scale uncertainties are obtaining by varying independently the renormalization and factorization scale in the range $M_W/2 < \mu_R, \mu_F < 2M_W$. The MSTW 2008 NLO PDF set has been used, with error bands corresponding to 68% confidence level.

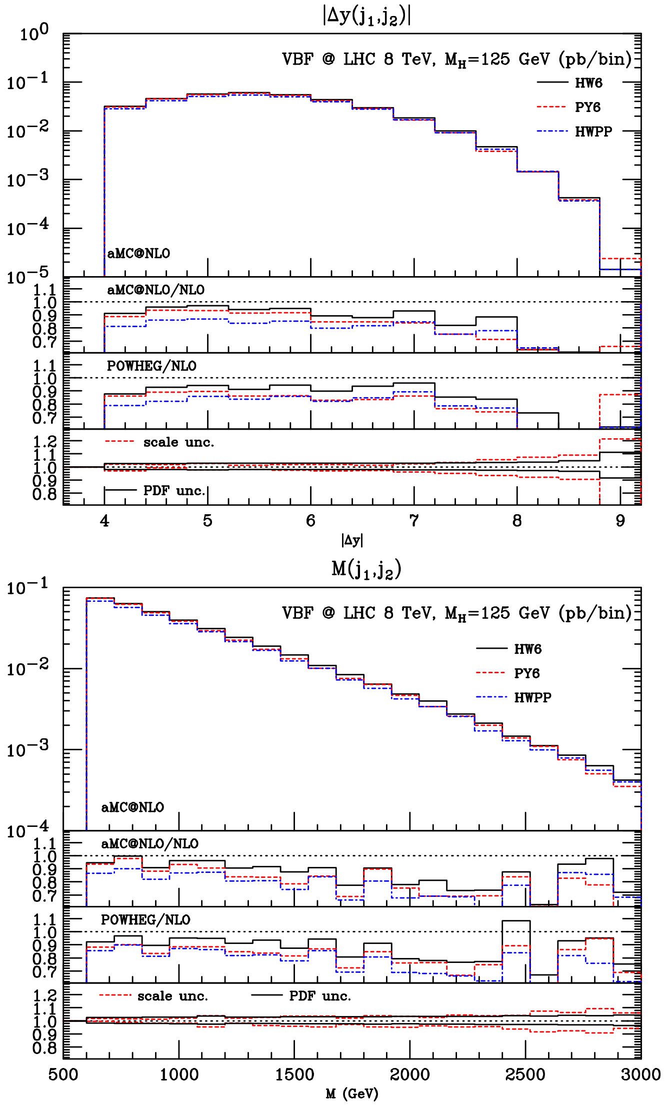

Figure 5.5.8: Rapidity separation (top) and invariant mass (bottom) of the two hardest jets distributions for VBF. The main frame shows the aMC@NLO samples, matched with HERWIG6 (black solid), virtuality-ordered Pythia6 (red dashed) and HERWIG++ (blue dot-dashed). The first (second) inset shows the ratios of the aMC@NLO (POWHEG) distributions over the fixed-order NLO one, with the same color pattern as the main frame. The third inset shows scale (red-dashed) and PDF uncertainties (black solid) computed from the aMC@NLO + HERWIG6 sample. Scale uncertainties are obtaining by varying independently the renormalization and factorization scale in the range $M_W/2 < \mu_R, \mu_F < 2M_W$. The MSTW 2008 NLO PDF set has been used, with error bands corresponding to 68% confidence level.

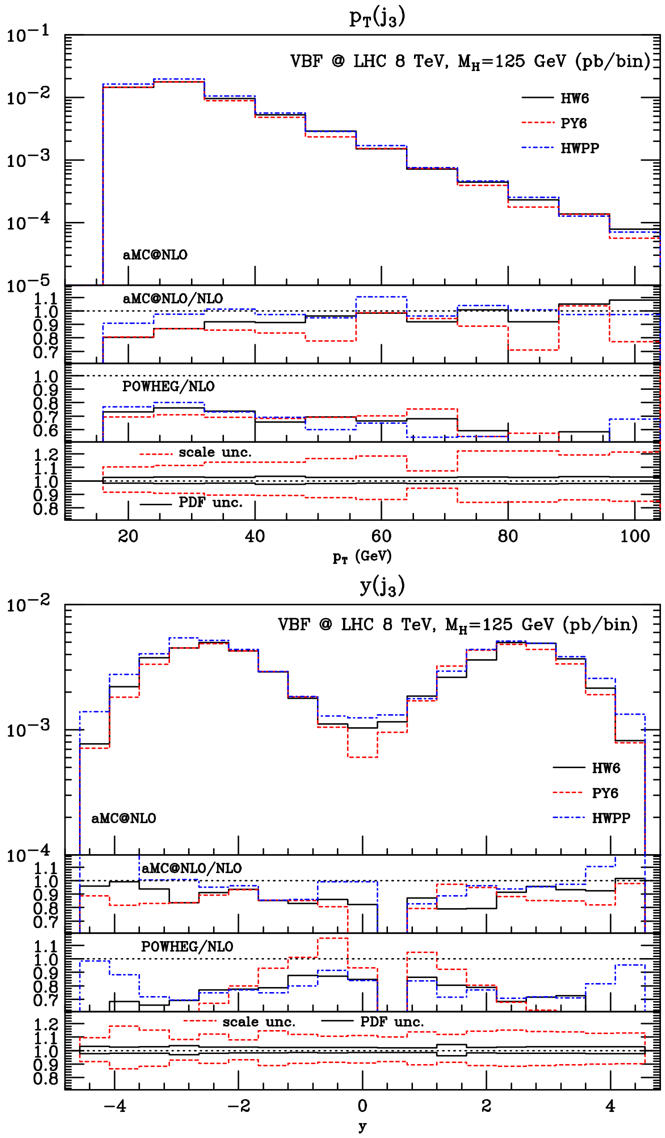

Figure 5.5.9: Third hardest jet transverse momentum (bottom) and rapidity (top) distributions for VBF. The main frame shows the aMC@NLO samples, matched with HERWIG6 (black solid), virtuality-ordered Pythia6 (red dashed) and HERWIG++ (blue dot-dashed). The first (second) inset shows the ratios of the aMC@NLO (POWHEG) distributions over the fixed-order NLO one, with the same color pattern as the main frame. The third inset shows scale (red-dashed) and PDF uncertainties (black solid) computed from the aMC@NLO + HERWIG6 sample. Scale uncertainties are obtaining by varying independently the renormalization and factorization scale in the range $M_W/2 < \mu_R, \mu_F < 2M_W$. The MSTW 2008 NLO PDF set has been used, with error bands corresponding to 68% confidence level.

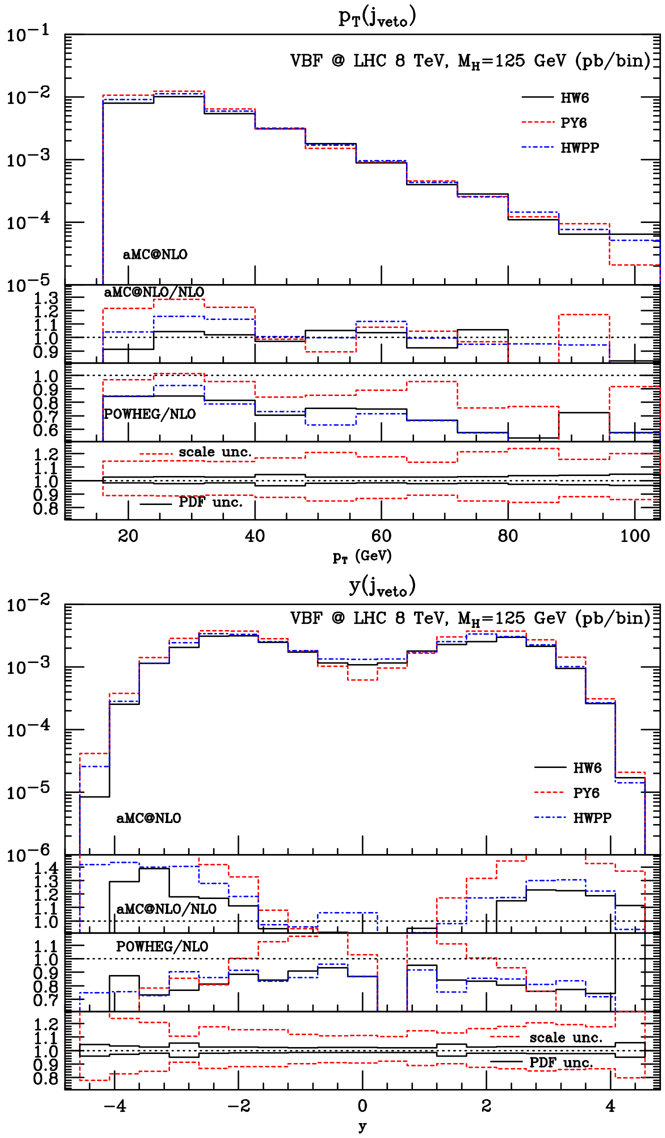

Figure 5.5.10: Veto jet transverse momentum (top) and rapidity (bottom) distributions for VBF. The main frame shows the aMC@NLO samples, matched with HERWIG6 (black solid), virtuality-ordered Pythia6 (red dashed) and HERWIG++ (blue dot-dashed). The first (second) inset shows the ratios of the aMC@NLO (POWHEG) distributions over the fixed-order NLO one, with the same color pattern as the main frame. The third inset shows scale (red-dashed) and PDF uncertainties (black solid) computed from the aMC@NLO + HERWIG6 sample. Scale uncertainties are obtaining by varying independently the renormalization and factorization scale in the range $M_W/2 < \mu_R,\mu_F < 2M_W$. The MSTW 2008 NLO PDF set has been used, with error bands corresponding to 68% confidence level.

Chapter 6

Prospects

After the discovery of the Higgs-like particle at the LHC, and the conclusion of the 8 TeV run, the main challenge for the scientific community is to determine the nature of the newly discovered resonance. In particular, it is of greatest importance to assess if this particle is the Higgs boson as predicted in the SM or not, and in the latter case to understand which new physics scenario it is going to unveil. The measurement of the Higgs boson spin, parity and couplings to the SM particles has now become a "hot topic", which demands strong commitment from both experiments and theory.

From the theory point of view, this means delivering predictions which can cover all the possible cases (spin 0, 1, 2, . . .) with consistent inclusion of higher orders QCD corrections in the predictions, possibly in all production (and decay) channels. Up to the present moment, most of the studies consider the dominant $2 \to 1$ production channel and/or do not include higher order corrections or parton-shower effects.

Indeed, on top of the usual observables related to the Higgs decay products (e.g. angular correlations among the leptons), lot of information about the nature of the produced resonance is also carried by angular correlations of the two tagging jets which accompany VBF events, (partially) compensating for the smaller total rate with respect the dominant Higgs production channel.

Because of the peculiar nature of VBF, in which QCD factors out and does not involve the produced resonance, it should cost very little effort to study e.g. the production of a vectorial or spin-2 resonance, providing complementary informations to the $2 \to 1$ case. The advantage of having a fully automated tool such as aMC@NLO, presented in Chapter 5, allows the user to have trustful, accurate and realistic results with almost no effort, once the relevant model file will be made available. On top of this, one could even easily obtain the total NNLO normalization, exploiting the structure function approach presented in Chapter 4.

Work in these directions is in progress [174].

Appendices

Appendix A

The VBF phase space in the structure-function approach

In this appendix I briefly document the parameterization for the phase space of VBF in the structure function approach. I will first take the most general case, which is the production of an n-particles final state via VBF with momenta $K_1, \ldots, K_n$, then I will specialize to the case of one particle.

In the structure function approach I can consider the proton remnants as massive particles, and integrate over their masses, which are labeled s_1, s_2.

I will call P_1, P_2 the momenta of the incoming protons, and P_{X_1}, P_{X_2} the momenta of the proton remnants. The choice of kinematic variables is guided by the requirement to resemble the DIS kinematics as much as possible. I work in the hadronic center-of-mass reference frame, with

$$P_1 = \frac{1}{2}\left(\sqrt{S}, 0, 0, \sqrt{S}\right), \qquad P_2 = \frac{1}{2}\left(\sqrt{S}, 0, 0, -\sqrt{S}\right), \tag{A.1}$$

Then, the Lorentz invariant phase space for this process is (cf. Eq. (4.2)),

$$\begin{aligned} dPS \; = \; & \prod_{i=1,2} ds_i \, \frac{d^4 P_{X_i}}{(2\pi)^4} \, 2\pi\delta\left(P_{X_i}^2 - s_i\right) \, dPS_n(K_1, \ldots, K_n) \, \times \\ & \times (2\pi)^4 \delta^4 \left(P_1 + P_2 - P_{X_1} - P_{X_2} - \sum_{j=1,n} K_j \right). \end{aligned} \tag{A.2}$$

In Eq. (A.2) the phase space of the proton remnants has been separated from the one of the particles produced via VBF. In order to solve the kinematics, let q_i be the momentum exchanged by each of the two protons, with the convention, as for DIS, that the direction of q_i is incoming with respect to the proton vertex (see Fig. 3.1),

$$q_i = P_{X_i} - P_i \,. \tag{A.3}$$

The momenta q_i are parameterized in terms of the two light-like momenta P_i and the transverse components $\mathbf{q_i^\perp}$:

$$q_1 = \frac{2P_1 \cdot q_1}{2P_1 \cdot P_2} P_2 + \frac{2P_2 \cdot q_1}{2P_1 \cdot P_2} P_1 + \mathbf{q_1^\perp} \,, \tag{A.4}$$

$$q_2 = \frac{2P_2 \cdot q_2}{2P_1 \cdot P_2} P_1 + \frac{2P_1 \cdot q_2}{2P_1 \cdot P_2} P_2 + \mathbf{q_2^\perp} \,. \tag{A.5}$$

The Bjorken scaling variables x_i for the DIS process are given by the scalar products $P_i \cdot q_i$

$$2P_i \cdot q_i = \frac{-q_i^2}{x_i} = \frac{Q_i^2}{x_i} \,, \tag{A.6}$$

where $Q_i^2 = -q_i^2$. In analogy one can also define variables y_i via the relation

$$2P_2 \cdot q_1 = \frac{Q_1^2}{y_1} \,, \qquad 2P_1 \cdot q_2 = \frac{Q_2^2}{y_2} \,. \tag{A.7}$$

so that

$$y_i = -\frac{Q_i^4}{x_i S \,(Q_i^2 - q_i^{\perp 2})} \,, \tag{A.8}$$

with $q_i^\perp = \sqrt{\left|\mathbf{q_i^{\perp}}^2\right|}$.
Then, the integration measure can be expressed as

$$d^4 q_i = dQ_i^2 \, d^2\mathbf{q_i^\perp} \, \frac{dx_i}{2x_i} \,, \tag{A.9}$$

and

$$P_{X_i}^2 = Q_i^2 \left(\frac{1}{x_i} - 1 \right) . \tag{A.10}$$

The phase space Eq. (A.2) reduces now to the following form,

$$dPS = \frac{1}{(2\pi)^2}\prod_{i=1,2} dQ_i^2\, d^2\mathbf{q_i}^\perp\, \frac{dx_i}{2x_i}\, dPS_n(K_1,\dots,K_n)\,(2\pi)^4\delta^4\left(q_1+q_2+\sum_{j=1,n}K_j\right), \tag{A.11}$$

and the integrations on the transverse components can be cast in polar coordinates,

$$d^2\mathbf{q_1}^\perp\, d^2\mathbf{q_2}^\perp = q_1^\perp\, dq_1^\perp d\varphi_1\, q_2^\perp\, dq_2^\perp d\varphi_2 = 2\pi\, q_1^\perp\, dq_1^\perp\, q_2^\perp\, dq_2^\perp d\varphi_{12}\,. \tag{A.12}$$

The momentum-conservation condition imposed by the Dirac delta-function in Eq. (A.11) provides a relation between the proton remnants variables and the total energy of the VBF products:

$$\begin{aligned} S_{VBF} &= (K_1+\ldots+K_n)^2 = (q_1+q_2)^2 = \qquad\qquad\qquad \text{(A.13)}\\ &= \frac{1}{Q_1^2Q_2^2} S\,x_1x_2\left(Q_1^2-q_1^{\perp 2}\right)\left(Q_2^2-q_2^{\perp 2}\right)+\frac{Q_1^2Q_2^2}{S\,x_1x_2}-Q_1^2-Q_2^2-2q_1^\perp q_2^\perp\cos\varphi_{12} \end{aligned}$$

Using this equation one can generate the phase space of the VBF-produced particles once the proton remnants variables are fixed, simply in the same way as for the decay of a particle.

I will finally go through the details of the case in which only one particle with mass m and momentum K is produced via VBF. In this case one simply has

$$dPS_1(K) = \frac{d^4K}{(2\pi)^4}\, 2\pi\delta\left(K^2-m^2\right), \tag{A.14}$$

and the d^4K integration can be eliminated using the momentum-conservation Dirac delta-function, so that it is only necessary to solve the mass-shell condition imposed by the delta-function in Eq. (A.14) (which is nothing but Eq. (A.13) with $S_{VBF} = m^2$):

$$m^2 = \frac{1}{Q_1^2Q_2^2} S\,x_1x_2\left(Q_1^2-q_1^{\perp 2}\right)\left(Q_2^2-q_2^{\perp 2}\right)+\frac{Q_1^2Q_2^2}{S\,x_1x_2}-Q_1^2-Q_2^2-2q_1^\perp q_2^\perp\cos\varphi_{12}\,. \tag{A.15}$$

This equation can, of course, be easily solved for $\cos\varphi_{12}$, but in this case it would lead to an (integrable) singularity in the Jacobian, and therefore to numerical problems. Therefore, the choice has been to write Eq. (A.15) as a second degree equation for $q_2^\perp$:

$$A q_2^{\perp 2} + B q_2^\perp + C = 0\,, \tag{A.16}$$

with

$$
\begin{aligned}
A &= \frac{S\,x_1 x_2 \left({q_1^{\perp}}^2 - Q_1^2\right)}{Q_1^2 Q_2^2}\,, && \text{(A.17)}\\
B &= -2 q_1^{\perp} \cos\varphi_{12}\,, && \text{(A.18)}\\
C &= \frac{Q_1^2 Q_2^2}{S\,x_1 x_2} - \frac{S\,x_1 x_2 q_1^{\perp}}{Q_1^2} + S\,x_1 x_2 - m^2 - Q_1^2 - Q_2^2\,. && \text{(A.19)}
\end{aligned}
$$

Since two solutions of $q_2^{\perp}$ exist for each set of parameters x_1, x_2, Q_1^2, Q_2^2, $q_1^{\perp}$, φ, two phase space points are evaluated. “Physical” phase space points are required to have positive $q_2^{\perp}$ and the number of rejected points can be greatly reduced if one asks

$$
0 < Q_2^2 < S\,x_1 x_2 \frac{\left(Q_1^2 - {q_1^{\perp}}^2\right)\left[Q_1^4 - Q_1^2\left(S\,x_1 x_2 - m^2\right) + {q_1^{\perp}}^2 S\,x_1 x_2\right]}{Q_1^2\left[Q_1^4 - Q_1^2\left({q_1^{\perp}}^2 \sin^2\varphi_{12} + S\,x_1 x_2\right) + {q_1^{\perp}}^2 S\,x_1 x_2\right]}\,, \tag{A.20}
$$

which corresponds to the positivity of the discriminant of Eq. (A.16). The other parameters are generated in the following ranges:

$$
\begin{aligned}
&x_1 \cdot x_2 \in \left[\frac{m^2}{S}, 1\right], \qquad \log x_1 \in \left[\log\frac{m^2}{S}, 0\right], \qquad Q_1^2 \in \left[Q_0^2, \left(\sqrt{S} - m\right)^2\right],\\
&q_1^{\perp} \in [0, Q_1]\,, \qquad \varphi \in [0, 2\pi]\,, \qquad\qquad \text{(A.21)}
\end{aligned}
$$

where Q_0 is a technical cut set to 1 GeV which prevents sampling PDFs and α_s at too low scales. It also sets the lower bound for Q_2; the total cross-section has been checked not to depend on Q_0. The differential cross-section from Eq. (4.2), multiplied by the Jacobian corresponding to Eqs. (A.20)–(A.21), is integrated using VEGAS [175].

Appendix B

The structure function approach and the production of new resonances in VBF

In this appendix, I will report the expression of the contraction of the hadronic tensors and the $VV \to X$ matrix element in the case X is a scalar with anomalous couplings to vector bosons or a fermiophobic vector resonance.
The first case is considered in Sec. B.1, the second in Sec. B.2.

B.1 The VBF cross-section with anomalous VVH couplings

The most generic structure for the VVH vertex which generalizes Eq. (4.1), has the form [176]:

$$\Gamma^{\mu\nu}(q_1,q_2) = 2M_V^2\left(\left(\sqrt{2}G_F\right)^{1/2} + \frac{a_1}{\Lambda}\right)g_{\mu\nu} + \frac{a_2}{\Lambda}\left(q_1\cdot q_2 g^{\mu\nu} - q_2^{\mu}q_1^{\nu}\right) + \frac{a_3}{\Lambda}\varepsilon^{\mu\nu\rho\sigma}q_{1\rho}q_{2\sigma}, \tag{B.1}$$

Which can be rewritten as

$$\Gamma^{\mu\nu}(q_1,q_2) = A_1 g_{\mu\nu} + A_2\left(q_1\cdot q_2 g^{\mu\nu} - q_2^{\mu}q_1^{\nu}\right) + A_3\varepsilon^{\mu\nu\rho\sigma}q_{1\rho}q_{2\sigma}, \tag{B.2}$$

using the replacements

$$
\begin{aligned}
A_1 &= 2M_V^2\left(\left(\sqrt{2}G_F\right)^{1/2}+\frac{a_1}{\Lambda}\right),\\
A_2 &= \frac{a_2}{\Lambda},\\
A_3 &= \frac{a_3}{\Lambda}.
\end{aligned}
\tag{B.3}
$$

Eq. (4.5), with the replacement $\mathcal{M}^{\mu\nu} = \Gamma^{\mu\nu}(q_1, q_2)$ has now the form:

$$
W_{\mu\nu}\left(x_1, Q_1^2\right)\mathcal{M}^{\mu\rho}\mathcal{M}^{*\nu\sigma}W_{\rho\sigma}\left(x_2, Q_2^2\right) = \sum_{i,j=1}^{3} C_{ij}F_i\left(x_1, Q_1^2\right)F_j\left(x_2, Q_2^2\right),. \tag{B.4}
$$

Defining

$$
q_1 \cdot q_2 = q_{12}, \qquad P_a \cdot q_b = P_{ab}, \tag{B.5}
$$

the non-vanishing C_{ij} read

$$
\begin{aligned}
C_{11} = &\left(2+\frac{{q_{12}}^2}{{q_1}^2{q_2}^2}\right)|A_1|^2 + 6\,q_{12}\,\mathrm{Re}\left(A_1A_2^*\right) + \left({q_1}^2{q_2}^2+2{q_{12}}^2\right)|A_2|^2\\
&+2\left({q_{12}}^2-{q_1}^2{q_2}^2\right)|A_3|^2,
\end{aligned}
\tag{B.6}
$$

$$
\begin{aligned}
C_{12} = &\frac{1}{P_{22}}\left[\frac{{P_{22}}^2}{{q_2}^2}+\frac{1}{{q_1}^2}\left(P_{21}-\frac{P_{22}}{{q_2}^2}q_{12}\right)^2\right]|A_1|^2 + 2\frac{P_{22}\,q_{12}}{{q_2}^2}\,\mathrm{Re}\left(A_1A_2^*\right)\\
&+P_{21}\left(2\,q_{12}-\frac{P_{21}\,{q_2}^2}{P_{22}}\right)|A_2|^2+\left(2\,P_{21}\,q_{12}-\frac{{P_{21}}^2\,{q_2}^2}{P_{22}}-P_{22}\,{q_1}^2\right)|A_3|^2,
\end{aligned}
\tag{B.7}
$$

$$
\begin{aligned}
C_{21} = &\frac{1}{P_{11}}\left[\frac{{P_{11}}^2}{{q_1}^2}+\frac{1}{{q_2}^2}\left(P_{12}-\frac{P_{11}}{{q_1}^2}q_{12}\right)^2\right]|A_1|^2 + 2\frac{P_{11}\,q_{12}}{{q_1}^2}\,\mathrm{Re}\left(A_1A_2^*\right)\\
&+\left(2\,P_{12}\,q_{12}-\frac{{P_{12}}^2\,{q_1}^2}{P_{11}}\right)|A_2|^2+\left(2\,P_{12}\,q_{12}-\frac{{P_{12}}^2\,{q_1}^2}{P_{11}}-P_{11}\,{q_2}^2\right)|A_3|^2,
\end{aligned}
\tag{B.8}
$$

$$\begin{aligned}
C_{22} \;=\; & \frac{1}{P_{11}\,P_{22}}\left(\frac{s}{2}-\frac{P_{11}\,P_{21}}{{q_1}^2}-\frac{P_{12}\,P_{22}}{{q_2}^2}+\frac{P_{11}\,P_{22}\,q_{12}}{{q_1}^2\,{q_2}^2}\right)^2 |A_1|^2 \\
& -2\left(P_{12}\,P_{21}-q_{12}\frac{s}{2}\right)\left(\frac{q_{12}}{{q_1}^2\,{q_2}^2}+\frac{s}{2\,P_{11}\,P_{22}}-\frac{P_{21}}{P_{22}\,{q_1}^2}-\frac{P_{12}}{P_{11}\,{q_2}^2}\right)\mathrm{Re}\left(A_1A_2^*\right) \\
& +2\left(\frac{q_{12}}{{q_1}^2\,{q_2}^2}+\frac{s}{2\,P_{11}\,P_{22}}-\frac{P_{21}}{P_{22}\,{q_1}^2}-\frac{P_{12}}{P_{11}\,{q_2}^2}\right)\varepsilon^{P_1\,P_2\,q_1\,q_2}\,\mathrm{Re}\left(A_1A_3^*\right) \\
& +\frac{(q_{12}\,s-2\,P_{12}\,P_{21})^2}{4\,P_{11}\,P_{22}}\,|A_2|^2-\frac{P_{12}\,P_{21}-q_{12}\,s}{P_{11}\,P_{22}}\,\varepsilon^{P_1\,P_2\,q_1\,q_2}\,\mathrm{Re}\left(A_2A_3^*\right) \\
& +\left\{s\left(q_{12}-\frac{P_{21}\,{q_2}^2}{P_{22}}-\frac{P_{12}\,{q_1}^2}{P_{11}}+\frac{P_{12}\,P_{21}\,q_{12}}{P_{11}\,P_{22}}\right)\right. \\
& \left.+\frac{1}{P_{11}\,P_{22}}\left[\frac{s^2}{4}\left({q_1}^2\,{q_2}^2-{q_{12}}^2\right)-{P_{12}}^2\,{P_{21}}^2\right]-P_{11}\,P_{22}+2\,P_{12}\,P_{21}\right\}|A_3|^2,
\end{aligned} \tag{B.9}$$

$$\begin{aligned}
C_{33} \;=\; & \frac{q_{12}\,s-2\,P_{12}\,P_{21}}{2\,P_{11}\,P_{22}}\,|A_1|^2 \\
& +\frac{1}{2}\left[\frac{s}{2\,P_{11}\,P_{22}}\left({q_1}^2\,{q_2}^2+{q_{12}}^2\right)+q_{12}-\frac{P_{12}\,{q_1}^2}{P_{11}}-\frac{P_{21}\,{q_2}^2}{P_{22}}\right. \\
& \left.-\frac{P_{12}\,P_{21}\,q_{12}}{P_{11}\,P_{22}}\right]\mathrm{Re}\left(A_1A_2^*\right)+\frac{q_{12}}{2\,P_{11}\,P_{22}}\,\varepsilon^{P_1\,P_2\,q_1\,q_2}\,\mathrm{Re}\left(A_1A_3^*\right) \\
& +\frac{q_{12}}{2}\left(q_{12}-\frac{P_{12}\,{q_1}^2}{P_{11}}-\frac{P_{21}\,{q_2}^2}{P_{22}}+\frac{s\,{q_1}^2\,{q_2}^2}{2\,P_{11}\,P_{22}}\right)|A_2|^2 \\
& +\frac{{q_1}^2\,{q_2}^2}{2\,P_{11}\,P_{22}}\,\varepsilon^{P_1\,P_2\,q_1\,q_2}\,\mathrm{Re}\left(A_2A_3^*\right) \\
& +\frac{q_{12}}{2}\left(q_{12}-\frac{P_{12}\,{q_1}^2}{P_{11}}-\frac{P_{21}\,{q_2}^2}{P_{22}}+\frac{P_{12}\,P_{21}\,{q_1}^2\,{q_2}^2}{P_{11}\,P_{22}\,q_{12}}\right)|A_3|^2.
\end{aligned} \tag{B.10}$$

B.2 The VBF cross-section for a vector resonance

Finally, I provide the formula for the total cross-section for the production of a vector resonance in the structure function approach.
We assume the usual gauge and Lorentz invariant tri-linear vertex (in principle more general cases can be considered [177]):

$$\Gamma^{\mu_1\mu_2\mu_3}(p_1,p_2,p_3)=g_{123}\left[g^{\mu_1\mu_2}\left(p_1^{\mu_3}-p_2^{\mu_3}\right)+g^{\mu_2\mu_3}\left(p_2^{\mu_1}-p_3^{\mu_1}\right)+g^{\mu_3\mu_1}\left(p_3^{\mu_2}-p_1^{\mu_2}\right)\right], \tag{B.11}$$

where all the momenta are taken to flow outside the vertex. Since in the processes considered the coupling g_{123} can always be factorized from the total cross-section, it will be set to unity in the following.
As in Sec. B.1, with the extra care to sum over the polarizations of the produced vector, I have

$$W_{\mu\nu}\left(x_1, Q_1^2\right) \sum_{\lambda} \left(\mathcal{M}_{\lambda}^{\mu\rho} \mathcal{M}^{*\nu\sigma}_{\lambda}\right) W_{\rho\sigma}\left(x_2, Q_2^2\right) = \sum_{i,j=1}^{3} C_{ij} F_i\left(x_1, Q_1^2\right) F_j\left(x_2, Q_2^2\right), \tag{B.12}$$

where I have set

$$\mathcal{M}_{\lambda}^{\mu\nu} = \Gamma_{\rho}^{\mu\nu}\,(q_1, q_2, -q_1 - q_2)\; \epsilon_{\lambda}^{\rho}\,(-q_1 - q_2)\,, \tag{B.13}$$

and the non-vanishing coefficients C_{ij} are

$$\begin{aligned} C_{11} &= \frac{1}{{q_1}^2 {q_2}^2} \Bigg[4\,{q_1}^2 {q_2}^2 q_{12} - 14\,{q_1}^4 {q_2}^2 - 14\,{q_1}^2 {q_2}^4 + 11\,{q_1}^2 {q_{12}}^2 \\ &\quad + 11 q_2^2 {q_{12}}^2 + 2\,{q_{12}}^3 + \frac{1}{m_{V'}^2} \left({q_1}^2 - {q_2}^2\right)^2 \left(2\,{q_1}^2 {q_2}^2 + {q_{12}}^2\right)\Bigg], \end{aligned} \tag{B.14}$$

$$\begin{aligned} C_{12} &= \frac{-1}{P_{22}\,{q_1}^2 {q_2}^4} \\ &\quad \Bigg[-11\,{P_{21}}^2 {q_1}^2 {q_2}^4 - 2\,{P_{21}}^2 q_{12} {q_2}^4 + {P_{21}}^2 {q_2}^6 + 22\,P_{21} P_{22} {q_1}^2 q_{12} {q_2}^2 \\ &\quad + 4\,P_{21} P_{22} {q_{12}}^2 {q_2}^2 - 2\,P_{21} P_{22} q_{12} {q_2}^4 + {P_{22}}^2 {q_1}^4 {q_2}^2 - 11 {P_{22}}^2 {q_1}^2 {q_{12}}^2 \\ &\quad - 2\,{P_{22}}^2 {q_1}^2 q_{12} {q_2}^2 + 5 {P_{22}}^2 {q_1}^2 {q_2}^4 - 2 {P_{22}}^2 {q_{12}}^3 - 3\,{P_{22}}^2 {q_{12}}^2 {q_2}^2 \\ &\quad - \frac{1}{m_{V'}^2} \left({q_1}^2 - {q_2}^2\right)^2 \left({P_{21}}^2 {q_2}^4 - 2\,P_{21} P_{22} q_{12} {q_2}^2 + {P_{22}}^2 {q_1}^2 {q_2}^2 + {P_{22}}^2 {q_{12}}^2\right)\Bigg], \end{aligned} \tag{B.15}$$

$$C_{21} = C_{12}\,(1 \leftrightarrow 2)\,, \tag{B.16}$$

$$C_{22} = \frac{1}{P_{11} P_{22}\,{q_1}^4 {q_2}^4} \Big\{ 3 {P_{11}}^2 {P_{21}}^2 {q_1}^2 {q_2}^4 + 2 {P_{11}}^2 {P_{21}}^2 q_{12} {q_2}^4 - {P_{11}}^2 {P_{21}}^2 {q_2}^6$$

$$
\begin{aligned}
&-6\,P_{11}{}^2\,P_{21}\,P_{22}\,q_1{}^2\,q_{12}\,q_2{}^2-4\,P_{11}{}^2\,P_{21}\,P_{22}\,q_{12}{}^2\,q_2{}^2+2\,P_{11}{}^2\,P_{21}\,P_{22}\,q_{12}\,q_2{}^4\\
&+3\,P_{11}{}^2\,P_{22}{}^2\,q_1{}^2\,q_{12}{}^2+2\,P_{11}{}^2\,P_{22}{}^2\,q_{12}{}^3+3P_{11}{}^2\,P_{22}{}^2\,q_{12}{}^2\,q_2{}^2\\
&-2\,P_{11}\,P_{12}\,P_{21}\,P_{22}\,q_1{}^4\,q_2{}^2+4\,P_{11}\,P_{12}\,P_{21}\,P_{22}\,q_1{}^2\,q_{12}\,q_2{}^2\\
&-2\,P_{11}\,P_{12}\,P_{21}\,P_{22}\,q_1{}^2\,q_2{}^4+2\,P_{11}\,P_{12}\,P_{22}{}^2\,q_1{}^4\,q_{12}\\
&-4\,P_{11}\,P_{12}\,P_{22}{}^2\,q_1{}^2\,q_{12}{}^2-6\,P_{11}\,P_{12}\,P_{22}{}^2\,q_1{}^2\,q_{12}\,q_2{}^2\\
&-P_{12}{}^2\,P_{22}{}^2\,q_1{}^6+2\,P_{12}{}^2\,P_{22}{}^2\,q_1{}^4\,q_{12}+3\,P_{12}{}^2\,P_{22}{}^2\,q_1{}^4\,q_2{}^2\\
&+s\,q_1{}^2\,q_2{}^2\,(q_1-q_2)^2\left(P_{11}\,P_{21}\,q_2{}^2-P_{11}\,P_{22}\,q_{12}+P_{12}\,P_{22}\,q_1{}^2\right)\\
&-\frac{s^2}{4}q_1{}^4\,q_2{}^4\,(q_1-q_2)^2\\
&\left.+\frac{\left(q_1{}^2-q_2{}^2\right)^2}{4m_{V'}^2}\left(2\,P_{11}\,P_{21}\,q_2{}^2-2\,P_{11}\,P_{22}\,q_{12}+2\,P_{12}\,P_{22}\,q_1{}^2-s\,q_1{}^2\,q_2{}^2\right)^2\right\},
\end{aligned}
\tag{B.17}
$$

$$
\begin{aligned}
C_{33}\;=\;\frac{1}{2\,P_{11}\,P_{22}}&\left[-8\,P_{11}\,P_{21}\,q_2{}^2+8\,P_{11}\,P_{22}\,q_{12}+P_{12}\,P_{21}\,q_1{}^2+6\,P_{12}\,P_{21}\,q_{12}+\right.\\
&P_{12}\,P_{21}\,q_2{}^2-8\,P_{12}\,P_{22}\,q_1{}^2-\frac{s}{2}\left(q_1{}^2\,q_{12}-8\,q_1{}^2\,q_2{}^2+6\,q_{12}{}^2+q_{12}\,q_2{}^2\right)\\
&\left.+\frac{1}{m_{V'}^2}\left(q_1{}^2-q_2{}^2\right)^2\left(-P_{12}\,P_{21}+\frac{s}{2}\,q_{12}\right)\right].
\end{aligned}
\tag{B.18}
$$

Appendix C

Scale choice effects on differential observables

The results shown in Sec. 5.5 have been computed with renormalization and factorization scales fixed to the W mass. Although this choice has been justified in Sec. 4.3 with arguments based on the convergence of the total cross-section, it may look as inappropriate for describing differential observables.
In this appendix I will compare the distributions shown in Sec. 5.5 with new ones obtained setting

$$\mu_{R,F} = \frac{1}{2} \sum_{i=parton} p_{T\,i}\,. \tag{C.1}$$

This choice can be justified that, at the LO, it is the average transverse momentum of the two final state partons.

I will not discuss all the observables which have been presented in Sec. 5.5, but only those where effects due to the dynamic scale choice are visible. For all observables, the choice of such a dynamic scale do not visibly change the predictions for the central values but, in some cases, it results in a more narrow scale uncertainty band. The observables for which this happens are the transverse momentum spectra of the two hardest jets, and their rapidity separation. For what concerns the other observables, no visible difference between the two scale choices is visible, neither in the central value prediction nor in the scale uncertainty band.

Fig. C.0.1 shows the transverse momentum of the hardest (top) and second hardest (bottom) jet. The main effect of the scale choice Eq. (C.1) is the reduction of the scale uncertainty band at large transverse momenta, where the W mass is too low. For what concerns the rapidity separation of the two hardest jets, shown in Fig. C.0.2, also in this case the dynamic scale choices has the advantage of showing narrower uncertainty band at large rapidity separations, where, as pointed in Sec. 5.5, a fixed scale choice is inadequate.
All effects are, however, minimal.

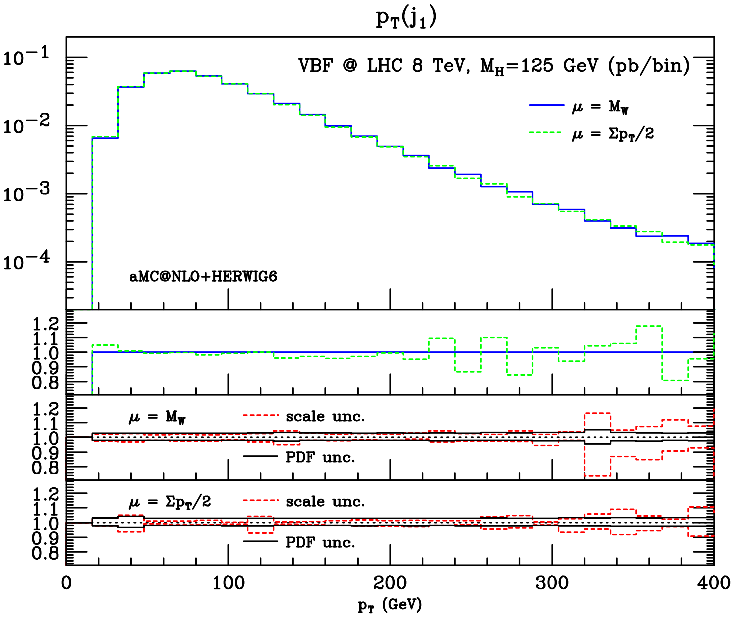

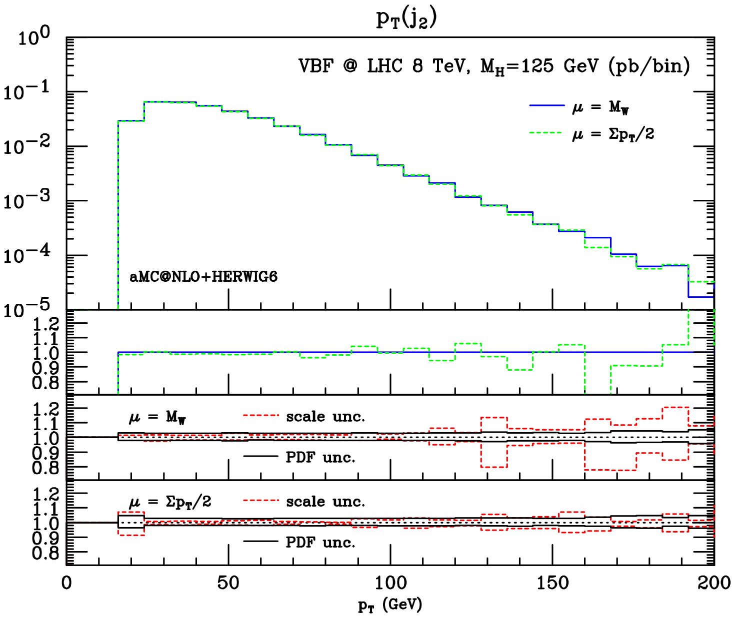

Figure C.0.1: Hardest (top) and second hardest jet transverse momentum. The main frame shows the aMC@NLO samples (matched with HERWIG6), computed setting $\mu_{F,R} = M_W$ (blue solid) and $\mu_{R,F} = \frac{1}{2}\sum_{i=parton} p_{T\,i}$ (green dashed). The first inlay shows the ratio of the two curves over the blue one. The second and third inlay show scale (red dashed) and PDF uncertainties (black solid) respectively for the blue and green curve of the first inlays. Scale uncertainties are obtained by varying independently the renormalization and factorization scales by a factor $1/2 < x_{R,F} < 2$ around the central value. The MSTW 2008 NLO PDF set has been used, with error bands corresponding to 68% confidence level.

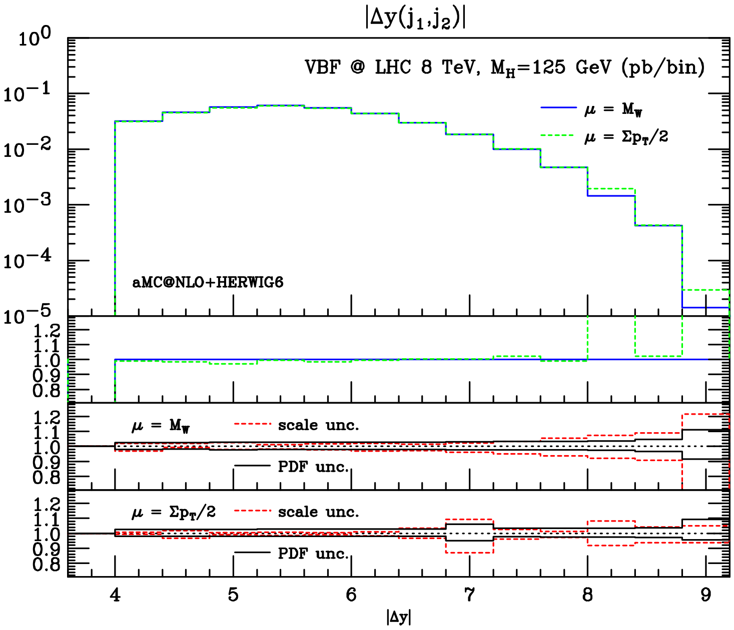

Figure C.0.2: Rapidity separation between the two hardest jets. The main frame shows the aMC@NLO samples (matched with HERWIG6), computed setting $\mu_{F,R} = M_W$ (blue solid) and $\mu_{R,F} = \frac{1}{2}\sum_{i=parton} p_{T\,i}$ (green dashed). The first inlay shows the ratio of the two curves over the blue one. The second and third inlay show scale (red dashed) and PDF uncertainties (black solid) respectively for the blue and green curve of the first inlays. Scale uncertainties are obtained by varying independently the renormalization and factorization scales by a factor $1/2 < x_{R,F} < 2$ around the central value. The MSTW 2008 NLO PDF set has been used, with error bands corresponding to 68% confidence level.

Appendix D

Jet definition and shower effects on the VBF cross-section after cuts

In Sec. 5.5.2 I have shown that the VBF cross-section after cuts has a non-negligible dependence on the PSMC. This dependence was traced back to the way each PSMC generates extra radiation, and to the possibility that the extra radiation may be lost if it falls outside the jet cone.

It is therefore important to study how such differences depend on the given jet definition, and whether they entirely come from the shower phase or also hadronization has a role.

To this aim, I will compute the exclusive jet multiplicities using different values for the jet minimum p_T and radius, with and hadronization enabled or disabled. Apart for these parameters, the same cuts of Sec. 5.5 are used. Since both POWHEG and aMC@NLO show almost the same effects when different showers are used, I will limit myself to results obtained with aMC@NLO.

Fig. D.0.1 shows the results for the two and three jet multiplicities obtained using the anti-k_T algorithm with different values of the radius parameters ranging from 0.1 to 1.1. The histograms use the same color and line pattern used in Sec. 5.5.2: black solid for HERWIG6, red dashed for Pythia6 and blue dot-dashed for HERWIG++. For each value of ΔR, two sets of ratio plots are shown. In the first three plots, jets are required to have a minimum transverse momentum of at least 20 GeV (as in the results shown in Sec. 5.5.2), while the other plots show results for a higher jet p_T threshold (40 GeV). In each set the first and second plots show respectively the ratios over the HERWIG6 prediction of results with and without hadronization effects. The last plot show, for each PSMC, the ratio of the results with hadronization over those without hadronization. As in Sec. 5.5.2, the simulation of the underlying event is disabled.

As it could have been expected, larger values of the radius parameter reduce the differences among the rates predicted by the different PSMCs, for both considered p_T cuts. Indeed, a larger value of the radius correspond in being more inclusive on the extra radiation, therefore being less sensitive on the different ways this extra radiation is generated. This can be specially seen in the two jet bin, which gives the bulk of the total cross-section. For the three jet bin, the pattern is more complicated: the best agreement among the three PSMC is found for a rather low value of ΔR (0.3) while for higher values larger discrepancies are found. No easy explanation of this can be given.
For what concerns hadronization it is very interesting to see that, while for Pythia6 and HERWIG6 effects are moderate (with the exception of the smallest values of ΔR), for HERWIG++ they are larger, and negative. In particular one can see that these effects account almost for the whole difference between HERWIG++ and HERWIG6. These differences deserve further investigations in conjunction with the PSMCs authors. Also hadronization effects tend to diminish for larger radii.

Effects due to the choice of a different jet clustering algorithm are found to be minor.

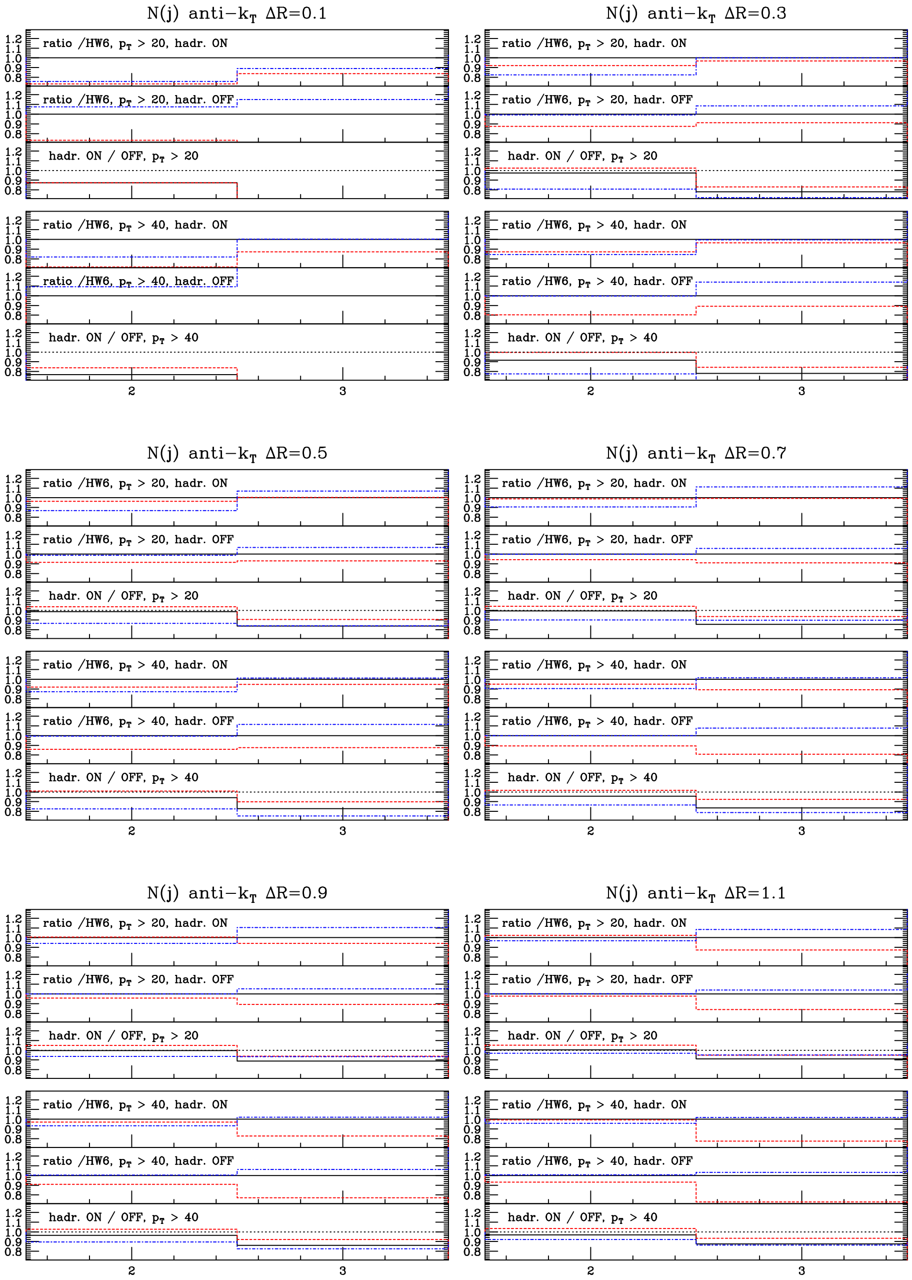

N(j) anti−k$_T$ ΔR=0.1

N(j) anti−k$_T$ ΔR=0.3

N(j) anti−k$_T$ ΔR=0.5

N(j) anti−k$_T$ ΔR=0.7

N(j) anti−k$_T$ ΔR=0.9

N(j) anti−k$_T$ ΔR=1.1

Figure D.0.1: Jet multiplicity ratios for different values of the jet radius parameter ΔR and of the jet minimum p_T. Results obtained without hadronization are also shown. See the text for details.

Bibliography

[1] S. Glashow, Partial Symmetries of Weak Interactions, Nucl.Phys. **22**, 579 (1961).

[2] S. Weinberg, A Model of Leptons, Phys.Rev.Lett. **19**, 1264 (1967).

[3] A. Salam, Weak and Electromagnetic Interactions, Conf.Proc. **C680519**, 367 (1968).

[4] P. W. Higgs, Broken symmetries, massless particles and gauge fields, Phys.Lett. **12**, 132 (1964).

[5] P. W. Higgs, Broken Symmetries and the Masses of Gauge Bosons, Phys.Rev.Lett. **13**, 508 (1964).

[6] F. Englert and R. Brout, Broken Symmetry and the Mass of Gauge Vector Mesons, Phys.Rev.Lett. **13**, 321 (1964).

[7] G. Guralnik, C. Hagen, and T. Kibble, Global Conservation Laws and Massless Particles, Phys.Rev.Lett. **13**, 585 (1964).

[8] P. W. Higgs, Spontaneous Symmetry Breakdown without Massless Bosons, Phys.Rev. **145**, 1156 (1966).

[9] T. Kibble, Symmetry breaking in nonAbelian gauge theories, Phys.Rev. **155**, 1554 (1967).

[10] M. Gell-Mann, A Schematic Model of Baryons and Mesons, Phys.Lett. **8**, 214 (1964).

[11] H. Fritzsch, M. Gell-Mann, and H. Leutwyler, Advantages of the Color Octet Gluon Picture, Phys.Lett. **B47**, 365 (1973).

[12] D. Gross and F. Wilczek, Ultraviolet Behavior of Nonabelian Gauge Theories, Phys.Rev.Lett. **30**, 1343 (1973).

[13] H. D. Politzer, Reliable Perturbative Results for Strong Interactions?, Phys.Rev.Lett. **30**, 1346 (1973).

[14] ATLAS Collaboration, G. Aad *et al.*, Observation of a new particle in the search for the Standard Model Higgs boson with the ATLAS detector at the LHC, Phys.Lett. **B716**, 1 (2012), arXiv:1207.7214.

[15] CMS Collaboration, S. Chatrchyan *et al.*, Observation of a new boson at a mass of 125 GeV with the CMS experiment at the LHC, Phys.Lett. **B716**, 30 (2012), arXiv:1207.7235.

[16] ATLAS Collaboration, Study of the spin of the new boson with up to 25 fb^{-1} of ATLAS data, (2013).

[17] ATLAS Collaboration, Combined coupling measurements of the Higgs-like boson with the ATLAS detector using up to 25 fb^{-1} of proton-proton collision data, (2013).

[18] CMS Collaboration, Combination of standard model Higgs boson searches and measurements of the properties of the new boson with a mass near 125 GeV.

[19] MSTW Collaboration,
`http://mstwpdf.hepforge.org/plots/plots.html` .

[20] P. Bolzoni, F. Maltoni, S. Moch, and M. Zaro, Higgs production via vector-boson fusion at NNLO in QCD, Phys.Rev.Lett. **105**, 011801 (2010), arXiv:1003.4451.

[21] P. Bolzoni, F. Maltoni, S.-O. Moch, and M. Zaro, Vector boson fusion at NNLO in QCD: SM Higgs and beyond, Phys.Rev. **D85**, 035002 (2012), arXiv:1109.3717.

[22] S. Frixione, P. Torrielli, and M. Zaro, Higgs production through vector-boson fusion at the NLO matched with parton showers, Submitted to Phys. Lett. **B** (2013), arXiv:1304.7927.

[23] LHC Higgs Cross Section Working Group, S. Dittmaier *et al.*, Handbook of LHC Higgs Cross Sections: 1. Inclusive Observables, (2011), arXiv:1101.0593.

[24] LHC Higgs Cross Section Working Group, S. Dittmaier *et al.*, Handbook of LHC Higgs Cross Sections: 3. Higgs Properties, (in preparation) (2013).

[25] P. Bolzoni, M. Zaro, F. Maltoni, and S. Moch, Higgs production at NNLO in QCD: The VBF channel, Nucl.Phys.Proc.Suppl. **205-206**, 314 (2010), arXiv:1006.2323.

[26] M. Zaro, P. Bolzoni, F. Maltoni, and S. Moch, Charged Higgs production via vector-boson fusion at NNLO in QCD, (2010), arXiv:1012.1806.

[27] M. Zaro, P. Bolzoni, F. Maltoni, and S. Moch, Higgs production via vector-boson fusion at NNLO in QCD, PoS **DIS2010**, 211 (2010).

[28] Y. Nambu, Axial vector current conservation in weak interactions, Phys.Rev.Lett. **4**, 380 (1960).

[29] Y. Nambu and G. Jona-Lasinio, Dynamical Model of Elementary Particles Based on an Analogy with Superconductivity. 1., Phys.Rev. **122**, 345 (1961).

[30] Y. Nambu and G. Jona-Lasinio, DYNAMICAL MODEL OF ELEMENTARY PARTICLES BASED ON AN ANALOGY WITH SUPERCONDUCTIVITY. II, Phys.Rev. **124**, 246 (1961).

[31] J. Goldstone, Field Theories with Superconductor Solutions, Nuovo Cim. **19**, 154 (1961).

[32] J. Goldstone, A. Salam, and S. Weinberg, Broken Symmetries, Phys.Rev. **127**, 965 (1962).

[33] Particle Data Group, K. Nakamura *et al.*, Review of Particle Physics, J.Phys.G **G37**, 075021 (2010).

[34] A. Djouadi, The Anatomy of electro-weak symmetry breaking. I: The Higgs boson in the standard model, Phys.Rept. **457**, 1 (2008), arXiv:hep-ph/0503172.

[35] The Higgs Cross-Section Working Group,
`https://twiki.cern.ch/twiki/bin/view/LHCPhysics/CrossSections.`

[36] H. Georgi, S. Glashow, M. Machacek, and D. V. Nanopoulos, Higgs Bosons from Two Gluon Annihilation in Proton Proton Collisions, Phys.Rev.Lett. **40**, 692 (1978).

[37] A. Djouadi, M. Spira, and P. Zerwas, Production of Higgs bosons in proton colliders: QCD corrections, Phys.Lett. **B264**, 440 (1991).

[38] S. Dawson, Radiative corrections to Higgs boson production, Nucl.Phys. **B359**, 283 (1991).

[39] M. Spira, A. Djouadi, D. Graudenz, and P. Zerwas, Higgs boson production at the LHC, Nucl.Phys. **B453**, 17 (1995), arXiv:hep-ph/9504378.

[40] R. V. Harlander and W. B. Kilgore, Next-to-next-to-leading order Higgs production at hadron colliders, Phys.Rev.Lett. **88**, 201801 (2002), arXiv:hep-ph/0201206.

[41] C. Anastasiou and K. Melnikov, Higgs boson production at hadron colliders in NNLO QCD, Nucl.Phys. **B646**, 220 (2002), arXiv:hep-ph/0207004.

[42] V. Ravindran, J. Smith, and W. L. van Neerven, NNLO corrections to the total cross-section for Higgs boson production in hadron hadron collisions, Nucl.Phys. **B665**, 325 (2003), arXiv:hep-ph/0302135.

[43] S. Catani, D. de Florian, M. Grazzini, and P. Nason, Soft gluon resummation for Higgs boson production at hadron colliders, JHEP **0307**, 028 (2003), arXiv:hep-ph/0306211.

[44] C. Anastasiou, C. Duhr, F. Dulat, and B. Mistlberger, Soft triple-real radiation for Higgs production at N3LO, (2013), arXiv:1302.4379.

[45] C. Anastasiou, S. Buehler, C. Duhr, and F. Herzog, NNLO phase space master integrals for two-to-one inclusive cross sections in dimensional regularization, JHEP **1211**, 062 (2012), arXiv:1208.3130.

[46] U. Aglietti, R. Bonciani, G. Degrassi, and A. Vicini, Two loop light fermion contribution to Higgs production and decays, Phys.Lett. **B595**, 432 (2004), arXiv:hep-ph/0404071.

[47] S. Actis, G. Passarino, C. Sturm, and S. Uccirati, NLO Electroweak Corrections to Higgs Boson Production at Hadron Colliders, Phys.Lett. **B670**, 12 (2008), arXiv:0809.1301.

[48] C. Anastasiou, R. Boughezal, and F. Petriello, Mixed QCD-electroweak corrections to Higgs boson production in gluon fusion, JHEP **0904**, 003 (2009), arXiv:0811.3458.

[49] J. Baglio and A. Djouadi, Higgs production at the lHC, JHEP **1103**, 055 (2011), arXiv:1012.0530.

[50] D. de Florian and M. Grazzini, Higgs production at the LHC: updated cross sections at $\sqrt{s} = 8$ TeV, Phys.Lett. **B718**, 117 (2012), arXiv:1206.4133.

[51] C. Anastasiou, S. Buehler, F. Herzog, and A. Lazopoulos, Inclusive Higgs boson cross-section for the LHC at 8 TeV, JHEP **1204**, 004 (2012), arXiv:1202.3638.

[52] R. N. Cahn and S. Dawson, Production of Very Massive Higgs Bosons, Phys. Lett. **B136**, 196 (1984).

[53] T. Han, G. Valencia, and S. Willenbrock, Structure function approach to vector boson scattering in p p collisions, Phys.Rev.Lett. **69**, 3274 (1992), arXiv:hep-ph/9206246.

[54] K. Arnold *et al.*, VBFNLO: A Parton level Monte Carlo for processes with electroweak bosons, Comput.Phys.Commun. **180**, 1661 (2009), arXiv:0811.4559.

[55] M. Ciccolini, A. Denner, and S. Dittmaier, Strong and electroweak corrections to the production of Higgs + 2jets via weak interactions at the LHC, Phys.Rev.Lett. **99**, 161803 (2007), arXiv:0707.0381.

[56] M. Ciccolini, A. Denner, and S. Dittmaier, Electroweak and QCD corrections to Higgs production via vector-boson fusion at the LHC, Phys.Rev. **D77**, 013002 (2008), arXiv:0710.4749.

[57] S. Glashow, D. V. Nanopoulos, and A. Yildiz, Associated Production of Higgs Bosons and Z Particles, Phys.Rev. **D18**, 1724 (1978).

[58] T. Han and S. Willenbrock, QCD correction to the p p —gt; W H and Z H total cross-sections, Phys.Lett. **B273**, 167 (1991).

[59] O. Brein, A. Djouadi, and R. Harlander, NNLO QCD corrections to the Higgs-strahlung processes at hadron colliders, Phys.Lett. **B579**, 149 (2004), arXiv:hep-ph/0307206.

[60] G. Ferrera, M. Grazzini, and F. Tramontano, Associated WH production at hadron colliders: a fully exclusive QCD calculation at NNLO, Phys.Rev.Lett. **107**, 152003 (2011), arXiv:1107.1164.

[61] M. Ciccolini, S. Dittmaier, and M. Kramer, Electroweak radiative corrections to associated WH and ZH production at hadron colliders, Phys.Rev. **D68**, 073003 (2003), arXiv:hep-ph/0306234.

[62] Z. Kunszt, Associated Production of Heavy Higgs Boson with Top Quarks, Nucl.Phys. **B247**, 339 (1984).

[63] W. Beenakker *et al.*, Higgs radiation off top quarks at the Tevatron and the LHC, Phys.Rev.Lett. **87**, 201805 (2001), arXiv:hep-ph/0107081.

[64] W. Beenakker *et al.*, NLO QCD corrections to t anti-t H production in hadron collisions, Nucl.Phys. **B653**, 151 (2003), arXiv:hep-ph/0211352.

[65] S. Dawson, L. Orr, L. Reina, and D. Wackeroth, Associated top quark Higgs boson production at the LHC, Phys.Rev. **D67**, 071503 (2003), arXiv:hep-ph/0211438.

[66] S. Dawson *et al.*, Associated Higgs production with top quarks at the large hadron collider: NLO QCD corrections, Phys.Rev. **D68**, 034022 (2003), arXiv:hep-ph/0305087.

[67] R. Frederix *et al.*, Scalar and pseudoscalar Higgs production in association with a top-antitop pair, Phys.Lett. **B701**, 427 (2011), arXiv:1104.5613.

[68] The aMC@NLO team,
`http://amcatnlo.web.cern.ch/amcatnlo/` .

[69] G. Corcella *et al.*, HERWIG 6: An Event generator for hadron emission reactions with interfering gluons (including supersymmetric processes), JHEP **0101**, 010 (2001), arXiv:hep-ph/0011363.

[70] G. Corcella *et al.*, HERWIG 6.5 release note, (2002), arXiv:hep-ph/0210213.

[71] A. Martin, W. Stirling, R. Thorne, and G. Watt, Parton distributions for the LHC, Eur.Phys.J. **C63**, 189 (2009), arXiv:0901.0002.

[72] E. N. Argyres *et al.*, Stable calculations for unstable particles: Restoring gauge invariance, Phys. Lett. **B358**, 339 (1995), arXiv:hep-ph/9507216.

[73] A. Bassetto, M. Ciafaloni, and G. Marchesini, Jet Structure and Infrared Sensitive Quantities in Perturbative QCD, Phys.Rept. **100**, 201 (1983).

[74] J. Alwall *et al.*, MadGraph 5 : Going Beyond, JHEP **1106**, 128 (2011), arXiv:1106.0522.

[75] M. Cacciari, G. P. Salam, and G. Soyez, The Anti-k(t) jet clustering algorithm, JHEP **0804**, 063 (2008), arXiv:0802.1189.

[76] M. Cacciari, G. P. Salam, and G. Soyez, FastJet User Manual, Eur.Phys.J. **C72**, 1896 (2012), arXiv:1111.6097.

[77] R. Harlander, J. Vollinga, and M. M. Weber, Gluon-Induced Weak Boson Fusion, Phys.Rev. **D77**, 053010 (2008), arXiv:0801.3355.

[78] J. R. Andersen and J. M. Smillie, QCD and electroweak interference in Higgs production by gauge boson fusion, Phys. Rev. **D75**, 037301 (2007), arXiv:hep-ph/0611281.

[79] J. R. Andersen, T. Binoth, G. Heinrich, and J. M. Smillie, Loop induced interference effects in Higgs Boson plus two jet production at the LHC, JHEP **02**, 057 (2008), arXiv:0709.3513.

[80] W. A. Bardeen, A. J. Buras, D. W. Duke, and T. Muta, Deep Inelastic Scattering Beyond the Leading Order in Asymptotically Free Gauge Theories, Phys. Rev. **D18**, 3998 (1978).

[81] S. Moch, J. Vermaseren, and A. Vogt, The Three loop splitting functions in QCD: The Nonsinglet case, Nucl.Phys. **B688**, 101 (2004), arXiv:hep-ph/0403192.

[82] A. Vogt, Efficient evolution of unpolarized and polarized parton distributions with QCD-PEGASUS, Comput.Phys.Commun. **170**, 65 (2005), arXiv:hep-ph/0408244.

[83] W. L. van Neerven and A. Vogt, NNLO evolution of deep-inelastic structure functions: The singlet case, Nucl. Phys. **B588**, 345 (2000), arXiv:hep-ph/0006154.

[84] W. van Neerven and E. Zijlstra, Order alpha-s**2 contributions to the deep inelastic Wilson coefficient, Phys.Lett. **B272**, 127 (1991).

[85] E. B. Zijlstra and W. L. van Neerven, Order alpha-s**2 QCD corrections to the deep inelastic proton structure functions F2 and F(L), Nucl. Phys. **B383**, 525 (1992).

[86] E. B. Zijlstra and W. L. van Neerven, Order alpha-s**2 correction to the structure function F3 (x, Q**2) in deep inelastic neutrino - hadron scattering, Phys. Lett. **B297**, 377 (1992).

[87] S. Moch and J. Vermaseren, Deep inelastic structure functions at two loops, Nucl.Phys. **B573**, 853 (2000), arXiv:hep-ph/9912355.

[88] A. Vogt, S. Moch, and J. Vermaseren, The Three-loop splitting functions in QCD: The Singlet case, Nucl.Phys. **B691**, 129 (2004), arXiv:hep-ph/0404111.

[89] J. Vermaseren, A. Vogt, and S. Moch, The Third-order QCD corrections to deep-inelastic scattering by photon exchange, Nucl.Phys. **B724**, 3 (2005), arXiv:hep-ph/0504242.

[90] S. Moch, J. A. M. Vermaseren, and A. Vogt, Third-order QCD corrections to the charged-current structure function F_3, $Nucl.Phys.\mathbf{B813}, 220(2009), arXiv:$ 0812.4168.

[91] E. Remiddi and J. Vermaseren, Harmonic polylogarithms, Int.J.Mod.Phys. **A15**, 725 (2000), arXiv:hep-ph/9905237.

[92] T. Gehrmann and E. Remiddi, Numerical evaluation of harmonic polylogarithms, Comput.Phys.Commun. **141**, 296 (2001), arXiv:hep-ph/0107173.

[93] T. Figy, V. Hankele, and D. Zeppenfeld, Next-to-leading order QCD corrections to Higgs plus three jet production in vector-boson fusion, JHEP **02**, 076 (2008), arXiv:0710.5621.

[94] W. L. van Neerven and J. A. M. Vermaseren, LARGE LOOP INTEGRALS, Phys. Lett. **B137**, 241 (1984).

[95] J. Fleischer and T. Riemann, A complete algebraic reduction of one-loop tensor Feynman integrals, Phys. Rev. **D83**, 073004 (2011), arXiv:1009.4436.

[96] A. Denner and S. Dittmaier, Reduction of one-loop tensor 5-point integrals, Nucl. Phys. **B658**, 175 (2003), arXiv:hep-ph/0212259.

[97] R. K. Ellis and G. Zanderighi, Scalar one-loop integrals for QCD, JHEP **02**, 002 (2008), arXiv:0712.1851.

[98] V. Hirschi *et al.*, Automation of one-loop QCD corrections, JHEP **05**, 044 (2011), arXiv:1103.0621.

[99] R. Frederix, S. Frixione, F. Maltoni, and T. Stelzer, Automation of next-to-leading order computations in QCD: the FKS subtraction, JHEP **10**, 003 (2009), arXiv:0908.4272.

[100] A. Martin, R. Roberts, W. Stirling, and R. Thorne, Uncertainties of predictions from parton distributions. 1: Experimental errors, Eur. Phys. J. **C28**, 455 (2003), arXiv:hep-ph/0211080.

[101] A. Bredenstein, A. Denner, S. Dittmaier, and M. Weber, Precise predictions for the Higgs-boson decay H —amp;gt; WW/ZZ —amp;gt; 4 leptons, Phys.Rev. **D74**, 013004 (2006), arXiv:hep-ph/0604011.

[102] A. Bredenstein, A. Denner, S. Dittmaier, and M. M. Weber, Radiative corrections to the semileptonic and hadronic Higgs-boson decays H –> W W / Z Z –> 4 fermions, JHEP **02**, 080 (2007), arXiv:hep-ph/0611234.

[103] B. A. Kniehl, ON THE DECAY MODE $Z \to H$ g g, Phys. Rev. **D42**, 3100 (1990).

[104] B. A. Kniehl, ASSOCIATED PRODUCTION OF HIGGS AND Z BOSONS FROM GLUON FUSION IN HADRON COLLISIONS, Phys. Rev. **D42**, 2253 (1990).

[105] B. A. Kniehl and J. H. Kühn, QCD Corrections to the Z Decay Rate, Nucl.Phys. **B329**, 547 (1990).

[106] R. J. Gonsalves, C.-M. Hung, and J. Pawlowski, Heavy quark triangle diagram contributions to Z boson production in hadron collisions, Phys.Rev. **D46**, 4930 (1992).

[107] R. Mertig, M. Bohm, and A. Denner, FEYN CALC: Computer algebraic calculation of Feynman amplitudes, Comput.Phys.Commun. **64**, 345 (1991).

[108] F. Maltoni and T. Stelzer, MadEvent: Automatic event generation with MadGraph, JHEP **0302**, 027 (2003), arXiv:hep-ph/0208156.

[109] J. Alwall *et al.*, MadGraph/MadEvent v4: The New Web Generation, JHEP **09**, 028 (2007), arXiv:0706.2334.

[110] W. Bernreuther *et al.*, Two-loop QCD corrections to the heavy quark form-factors: Anomaly contributions, Nucl.Phys. **B723**, 91 (2005), arXiv:hep-ph/0504190.

[111] S. Alekhin, J. Blümlein, S. Klein, and S. Moch, The 3, 4, and 5-flavor NNLO Parton from Deep-Inelastic-Scattering Data and at Hadron Colliders, Phys.Rev. **D81**, 014032 (2010), arXiv:0908.2766.

[112] HAWK, A. Denner, S. Dittmaier, and A. Mück, `http://omnibus.uni-freiburg.de/~sd565/programs/hawk/hawk.html`.

[113] A. Denner, S. Dittmaier, M. Roth, and D. Wackeroth, Predictions for all processes e+ e- —gt; 4 fermions + gamma, Nucl.Phys. **B560**, 33 (1999), arXiv:hep-ph/9904472.

[114] A. Denner and S. Dittmaier, The Complex-mass scheme for perturbative calculations with unstable particles, Nucl.Phys.Proc.Suppl. **160**, 22 (2006), arXiv:hep-ph/0605312.

[115] S. Goria, G. Passarino, and D. Rosco, The Higgs Boson Lineshape, Nucl.Phys. **B864**, 530 (2012), arXiv:1112.5517.

[116] G. Passarino, http://personalpages.to.infn.it/ giampier/cphto.html, `http://personalpages.to.infn.it/~giampier/CPHTO.html`.

[117] N. Kauer and G. Passarino, Inadequacy of zero-width approximation for a light Higgs boson signal, JHEP **1208**, 116 (2012), arXiv:1206.4803.

[118] H1 and ZEUS Collaboration, F. Aaron *et al.*, Combined Measurement and QCD Analysis of the Inclusive e+- p Scattering Cross Sections at HERA, JHEP **1001**, 109 (2010), arXiv:0911.0884.

[119] H1 and ZEUS Collaboration, H1prelim-10-142, ZEUS-prel-10-018 (2010).

[120] S. Alekhin, J. Blumlein, and S. Moch, Parton Distribution Functions and Benchmark Cross Sections at NNLO, Phys.Rev. **D86**, 054009 (2012), arXiv:1202.2281.

[121] P. Jimenez-Delgado and E. Reya, Dynamical NNLO parton distributions, Phys.Rev. **D79**, 074023 (2009), arXiv:0810.4274.

[122] P. Jimenez-Delgado and E. Reya, Variable Flavor Number Parton Distributions and Weak Gauge and Higgs Boson Production at Hadron Colliders at NNLO of QCD, Phys.Rev. **D80**, 114011 (2009), arXiv:0909.1711.

[123] NNPDF Collaboration, R. D. Ball *et al.*, Unbiased global determination of parton distributions and their uncertainties at NNLO and at LO, Nucl.Phys. **B855**, 153 (2012), arXiv:1107.2652.

[124] J. Gao *et al.*, The CT10 NNLO Global Analysis of QCD, (2013), arXiv:1302.6246.

[125] A. Daleo, A. Gehrmann-De Ridder, T. Gehrmann, and G. Luisoni, Antenna subtraction at NNLO with hadronic initial states: initial-final configurations, JHEP **1001**, 118 (2010), arXiv:0912.0374.

[126] VBF@NNLO, P. Bolzoni, F. Maltoni, S. Moch, and M. Zaro, `http://vbf-nnlo.phys.ucl.ac.be/vbf.html`.

[127] S. Catani and M. Seymour, The Dipole formalism for the calculation of QCD jet cross-sections at next-to-leading order, Phys.Lett. **B378**, 287 (1996), arXiv:hep-ph/9602277.

[128] S. Catani and M. Seymour, A General algorithm for calculating jet cross-sections in NLO QCD, Nucl.Phys. **B485**, 291 (1997), arXiv:hep-ph/9605323.

[129] S. Frixione, Z. Kunszt, and A. Signer, Three jet cross-sections to next-to-leading order, Nucl.Phys. **B467**, 399 (1996), arXiv:hep-ph/9512328.

[130] S. Frixione, A General approach to jet cross-sections in QCD, Nucl.Phys. **B507**, 295 (1997), arXiv:hep-ph/9706545.

[131] J. M. Campbell, M. Cullen, and E. N. Glover, Four jet event shapes in electron - positron annihilation, Eur.Phys.J. **C9**, 245 (1999), arXiv:hep-ph/9809429.

[132] D. A. Kosower, Antenna factorization of gauge theory amplitudes, Phys.Rev. **D57**, 5410 (1998), arXiv:hep-ph/9710213.

[133] P. Nason, A New method for combining NLO QCD with shower Monte Carlo algorithms, JHEP **0411**, 040 (2004), arXiv:hep-ph/0409146.

[134] S. Frixione, P. Nason, and C. Oleari, Matching NLO QCD computations with Parton Shower simulations: the POWHEG method, JHEP **0711**, 070 (2007), arXiv:0709.2092.

[135] S. Frixione and B. R. Webber, Matching NLO QCD computations and parton shower simulations, JHEP **0206**, 029 (2002), arXiv:hep-ph/0204244.

[136] T. Kinoshita, Mass singularities of Feynman amplitudes, J.Math.Phys. **3**, 650 (1962).

[137] T. Lee and M. Nauenberg, Degenerate Systems and Mass Singularities, Phys.Rev. **133**, B1549 (1964).

[138] G. Altarelli and G. Parisi, Asymptotic Freedom in Parton Language, Nucl.Phys. **B126**, 298 (1977).

[139] G. Passarino and M. Veltman, One Loop Corrections for e+ e- Annihilation Into mu+ mu- in the Weinberg Model, Nucl.Phys. **B160**, 151 (1979).

[140] G. Ossola, C. G. Papadopoulos, and R. Pittau, Reducing full one-loop amplitudes to scalar integrals at the integrand level, Nucl.Phys. **B763**, 147 (2007), arXiv:hep-ph/0609007.

[141] C. Berger *et al.*, An Automated Implementation of On-Shell Methods for One-Loop Amplitudes, Phys.Rev. **D78**, 036003 (2008), arXiv:0803.4180.

[142] W. T. Giele, Z. Kunszt, and K. Melnikov, Full one-loop amplitudes from tree amplitudes, JHEP **0804**, 049 (2008), arXiv:0801.2237.

[143] A. van Hameren, C. Papadopoulos, and R. Pittau, Automated one-loop calculations: A Proof of concept, JHEP **0909**, 106 (2009), arXiv:0903.4665.

[144] G. Cullen *et al.*, Automated One-Loop Calculations with GoSam, Eur.Phys.J. **C72**, 1889 (2012), arXiv:1111.2034.

[145] F. Cascioli, P. Maierhofer, and S. Pozzorini, Scattering Amplitudes with Open Loops, Phys.Rev.Lett. **108**, 111601 (2012), arXiv:1111.5206.

[146] S. Badger, B. Biedermann, P. Uwer, and V. Yundin, NLO QCD corrections to multi-jet production at the LHC with a centre-of-mass energy of $\sqrt{s} = 8$ TeV, Phys.Lett. **B718**, 965 (2013), arXiv:1209.0098.

[147] V. Gribov and L. Lipatov, Deep inelastic e p scattering in perturbation theory, Sov.J.Nucl.Phys. **15**, 438 (1972).

[148] L. Lipatov, The parton model and perturbation theory, Sov.J.Nucl.Phys. **20**, 94 (1975).

[149] Y. L. Dokshitzer, Calculation of the Structure Functions for Deep Inelastic Scattering and e+ e- Annihilation by Perturbation Theory in Quantum Chromodynamics., Sov.Phys.JETP **46**, 641 (1977).

[150] T. Sjostrand, S. Mrenna, and P. Z. Skands, PYTHIA 6.4 Physics and Manual, JHEP **0605**, 026 (2006), arXiv:hep-ph/0603175.

[151] B. Webber, Monte Carlo Simulation of Hard Hadronic Processes, Ann.Rev.Nucl.Part.Sci. **36**, 253 (1986).

[152] G. Marchesini *et al.*, HERWIG: A Monte Carlo event generator for simulating hadron emission reactions with interfering gluons. Version 5.1 - April 1991, Comput.Phys.Commun. **67**, 465 (1992).

[153] M. Bahr *et al.*, Herwig++ Physics and Manual, Eur.Phys.J. **C58**, 639 (2008), arXiv:0803.0883.

[154] T. Sjostrand, S. Mrenna, and P. Z. Skands, A Brief Introduction to PYTHIA 8.1, Comput.Phys.Commun. **178**, 852 (2008), arXiv:0710.3820.

[155] T. Gleisberg *et al.*, Event generation with SHERPA 1.1, JHEP **0902**, 007 (2009), arXiv:0811.4622.

[156] S. Catani, F. Krauss, R. Kuhn, and B. Webber, QCD matrix elements + parton showers, JHEP **0111**, 063 (2001), arXiv:hep-ph/0109231.

[157] J. Alwall *et al.*, Comparative study of various algorithms for the merging of parton showers and matrix elements in hadronic collisions, Eur.Phys.J. **C53**, 473 (2008), arXiv:0706.2569.

[158] P. Nason and B. Webber, Next-to-Leading-Order Event Generators, Ann.Rev.Nucl.Part.Sci. **62**, 187 (2012), arXiv:1202.1251.

[159] S. Frixione *et al.*, The MCaNLO 4.0 Event Generator, (2010), arXiv:1010.0819.

[160] P. Torrielli and S. Frixione, Matching NLO QCD computations with PYTHIA using MC@NLO, JHEP **1004**, 110 (2010), arXiv:1002.4293.

[161] J. Alwall *et al.*, New Developments in MadGraph/MadEvent, AIP Conf.Proc. **1078**, 84 (2009), arXiv:0809.2410.

[162] G. Ossola, C. G. Papadopoulos, and R. Pittau, CutTools: A Program implementing the OPP reduction method to compute one-loop amplitudes, JHEP **0803**, 042 (2008), arXiv:0711.3596.

[163] S. Alioli, P. Nason, C. Oleari, and E. Re, NLO Higgs boson production via gluon fusion matched with shower in POWHEG, JHEP **0904**, 002 (2009), arXiv:0812.0578.

[164] S. Alioli, P. Nason, C. Oleari, and E. Re, A general framework for implementing NLO calculations in shower Monte Carlo programs: the POWHEG BOX, JHEP **1006**, 043 (2010), arXiv:1002.2581.

[165] G. Bevilacqua *et al.*, HELAC-NLO, Comput.Phys.Commun. **184**, 986 (2013), arXiv:1110.1499.

[166] J. M. Campbell *et al.*, NLO Higgs Boson Production Plus One and Two Jets Using the POWHEG BOX, MadGraph4 and MCFM, JHEP **1207**, 092 (2012), arXiv:1202.5475.

[167] R. Frederix *et al.*, Four-lepton production at hadron colliders: aMC@NLO predictions with theoretical uncertainties, JHEP **1202**, 099 (2012), arXiv:1110.4738.

[168] P. Nason and C. Oleari, NLO Higgs boson production via vector-boson fusion matched with shower in POWHEG, JHEP **1002**, 037 (2010), arXiv:0911.5299.

[169] T. Plehn, D. L. Rainwater, and D. Zeppenfeld, Determining the structure of Higgs couplings at the LHC, Phys.Rev.Lett. **88**, 051801 (2002), arXiv:hep-ph/0105325.

[170] K. Hagiwara, Q. Li, and K. Mawatari, Jet angular correlation in vector-boson fusion processes at hadron colliders, JHEP **0907**, 101 (2009), arXiv:0905.4314.

[171] C. Englert, D. Goncalves-Netto, K. Mawatari, and T. Plehn, Higgs Quantum Numbers in Weak Boson Fusion, JHEP **1301**, 148 (2013), arXiv:1212.0843.

[172] A. Djouadi, R. Godbole, B. Mellado, and K. Mohan, Probing the spin-parity of the Higgs boson via jet kinematics in vector boson fusion, (2013), arXiv:1301.4965.

[173] R. Frederix and S. Frixione, Merging meets matching in MC@NLO, JHEP **1212**, 061 (2012), arXiv:1209.6215.

[174] P. Artoisenet *et al.*, Higgs characterization reloaded, in preparation (2013).

[175] G. Lepage, A New Algorithm for Adaptive Multidimensional Integration, J.Comput.Phys. **27**, 192 (1978).

[176] Y. Takubo *et al.*, Measurement of Higgs Anomalous Coupling with H -amp;gt; WW* at International Linear Collider, (2010), arXiv:1006.3427.

[177] K. Hagiwara, R. Peccei, D. Zeppenfeld, and K. Hikasa, Probing the Weak Boson Sector in e+ e- —gt; W+ W-, Nucl.Phys. **B282**, 253 (1987).